High Power Converters for Current Source Converter-Type Series DC-Based Wind Energy Conversion System

by

Ling Xing

A thesis submitted in partial fulfillment of the requirements for the degree of

Doctor of Philosophy

in

Energy Systems

Department of Electrical and Computer Engineering
University of Alberta

Abstract

The high-voltage direct current (HVDC)-based wind energy conversion system (WECS) currently used in the industry requires a large and expensive substation. An emerging technology called current source converter (CSC)-type series DC-based WECS, can eliminate the need for the bulky and costly substation, resulting in substantial cost and size reductions for WECS. However, the power converters used in the CSC-type series DC-based WECS present several technical challenges. For example, the grid-side power converters require the use of bulky and costly multi-winding transformers, while the generator-side power converters face issues such as highly distorted generator stator currents, low scalability, and/or high complexity. Therefore, in this thesis, new power converters are proposed for generator-side and grid-side converters to address their respective technical challenges.

On the generator side of the CSC-type WECS, a passive rectifier-based converter utilizing a phase-shifting transformer is proposed. It effectively addresses the disadvantage of highly distorted generator stator currents commonly associated with passive rectifiers, while retaining all their advantages including low cost, high reliability, simplicity, and scalability. However, the phase-shifting transformer is bulky and heavy, which poses a disadvantage in WECS where space in the nacelle is limited. To address the challenges associated with a phase-shifting transformer-based converter, while retaining all its benefits, a passive rectifier-based converter using modular medium-frequency transformers (MFTs) is proposed for the generator-side converter. Compared to the phase-shifting transformer-based converter, the MFT-based converter offers reduced size and weight, while retaining all the advantages of the former. Additionally, an active rectifier-based converter using modular MFTs is also proposed for the generator-side converter. The use of an

active rectifier ensures superior harmonic performance in the generator stator currents, while the use of modular MFTs contributes to size and weight reductions in the generator-side conversion system. This converter offers benefits of both active rectifiers and MFTs simultaneously.

On the grid side of the CSC-type WECS, transformerless series-connected CSCs are proposed. The proposed transformerless CSCs are the first to eliminate the need for transformers in series-connected CSCs. This elimination results in substantial reductions in both cost and size. A modified version of the transformerless CSCs is also proposed. Compared to the original converter, this modification removes the need for series-connected switches by using cascaded half-bridge converters. This change eliminates the requirement for expensive and complex voltage balancing schemes while retaining all the advantages of the original converter. Modulations and controls are developed for proposed converters on both generator side and grid side of the CSC-type CSC. The performance of the proposed converters and the effectiveness of the proposed modulations and controls have been validated through simulations and lab-scale experiments.

Preface

This thesis comprises seven chapters. Chapter 1 reviews the state-of-the-art current source converter (CSC)-type wind energy conversion systems (WECS), identifies challenges of existing CSC-type WECS, and defines research objectives. In Chapter 2, a passive rectifier-based converter utilizing a phase-shifting transformer is proposed for the generator-side converter of the CSC-type WECS, effectively addressing the disadvantages of existing passive rectifier-based converters while retaining their advantages. Chapter 3 introduces a passive rectifier-based converter using modular medium-frequency transformers (MFTs) for the generator-side converter of the CSC-type WECS, offering reduced size and weight while maintaining the advantages of the phase-shifting transformer-based converter from Chapter 2. Chapter 4 proposes an active rectifier-based converter using modular MFTs for the generator-side converter of the CSC-type WECS, providing superior harmonic performance and reduced size and weight. Chapter 5 presents transformerless series-connected CSCs for the grid-side converter of the CSC-type WECS, eliminating transformers for substantial reductions in cost and size. Chapter 6 introduces a modified version of the transformerless CSCs, eliminating series-connected switches and the need for expensive and complex voltage balancing schemes while retaining all the advantages of the original converter presented in Chapter 5. Finally, Chapter 7 summarizes the contributions, conclusions, and outlines future research work.

The material presented in this thesis is based on the original work by Ling Xing. Related publications to this thesis under the supervision of Dr. Yunwei (Ryan) Li are listed below.

Chapter 2:

L. Xing, Q. Wei and Y. Li, "A New Power Converter for Current Source Converter-Based Wind Energy System," in IEEE Transactions on Industrial Electronics, vol. 69, no. 12, pp. 12851-12858, Dec. 2022, doi: 10.1109/TIE.2022.3140530.

Chapter 3:

L. Xing, Q. Wei and Y. Li, "An Improved Current-Source-Converter-Based Series-Connected Wind Energy Conversion System," in IEEE Transactions on Industrial Electronics, vol. 71, no. 5, pp. 4818-4829, May 2024, doi: 10.1109/TIE.2023.3283700.

Chapter 4:

L. Xing, Q. Wei and Y. Li, "A PWM Current-Source Converter-Based Wind Energy Conversion System," in IEEE Transactions on Power Electronics, vol. 39, no. 2, pp. 2787-2797, Feb. 2024, doi: 10.1109/TPEL.2023.3333315.

Chapter 5:

L. Xing, Q. Wei and Y. Li, "Transformerless Series-Connected Current Source Converter," in IEEE Transactions on Power Electronics, vol. 37, no. 8, pp. 8811-8815, Aug. 2022, doi: 10.1109/TPEL.2022.3159598.

Chapter 6:

L. Xing, Q. Wei and Y. Li, "Modified Transformerless Series-Connected Current Source Converter Without Series-Connected Switches," in IEEE Transactions on Industrial Electronics, vol. 70, no. 12, pp. 12331-12339, Dec. 2023, doi: 10.1109/TIE.2023.3236119.

Acknowledgements

First and foremost, I extend my sincere gratitude to my Ph.D. supervisor, Dr. Yunwei (Ryan) Li, for his unwavering support, guidance, and invaluable feedback throughout the past several years. His profound knowledge and experience in power electronics and energy systems, coupled with his great encouragement, have been instrumental in completing this work. This research and dissertation would not have been possible without his supervision.

Secondly, I would like to express my sincere appreciation to my supervisory committee members, Dr. Gregory Kish, Dr. Yasser Mohamed, and Dr. Xiaodong Liang from the University of Saskatchewan, for their constructive comments. I am also grateful to all the lab members, particularly Dr. Li Ding, Dr. Yuzhuo Li, Dr. Cheng Xue, Dr. Nie Hou, and Mr. Han Zhang, for their professional support and insightful suggestions. It has been an honor to study and work alongside them.

Thirdly, I acknowledge the financial support provided by Dr. Yunwei (Ryan) Li, the University of Alberta, the Alberta Innovates Graduate Student Scholarship program, and the Canada Graduate Scholarship-doctoral program.

Finally, my deepest appreciation goes to my family for their unconditional love, encouragement, and support. This is always my motivation.

Contents

List of Tables

List of Figures

List of Abbreviations

AC	Alternating Current
CHB	Cascaded H-bridge
CSC	Current source converter
DAB	Dual active bridge
DC	Direct current
FRT	Fault ride through
HVAC	High voltage alternating current
HVDC	High voltage direct current
KCL	Kirchoff's Current Law
LCC	Line commutated converter
LFT	Low frequency transformer
LV	Low voltage
MFT	Medium frequency transformer
MMC	Modular multilevel converter
NPC	Neutral point clamped
OTC	Optimal torque control
PI	Proportional integral
PMSG	Permanent magnet synchronous generator
PWM	Pulse-width modulation
RMC	Reduced matrix converter
SG	Synchronous generator
SGCT	Symmetrical gate-commutated thyristor
SPWM	Sinusoidal pulse-width modulation
SVM	Space vector modulation
THD	Total harmonic distortion
VSC	Voltage source converter
VSR	Voltage source rectifier

WECS	Wind energy conversion system
ZDC	Zero d-axis current
MPPT	Maximum power point tracking

List of Symbols

I_{dc}	DC current
$v_{s1} \ldots v_{sm}$	AC voltage of each module
$V_{C1} \ldots V_{Cm}$	DC voltage of each module
d	Duty cycle of the DC-DC converter
L_{dc}	DC-link inductance
v_{wind}	Wind speed
$\omega_{m\text{-}ref}$	Generator speed reference
ω_m	Generator speed
m	Number of modules
L_t	Leakage inductance of the secondary winding of the transformer
ω_s	Electrical speed of generator
P_g	Power captured by the wind turbine-generator unit
P_{dc}	Power received at the DC link
$I_{dc\text{-}gen\text{-}\mathrm{min}}$	Minimum DC-link current required by the generator side
$I_{dc\text{-}grid\text{-}\mathrm{min}}$	Minimum DC-link current required by the grid side
Q_s, P_s	Reactive power and real power
v_{dg}	*d*-axis component of the grid voltage
i_{dg}, i_{qg}	*d*- and *q*-axis components of grid current
$i_{dwi\text{-}ref}$, $i_{qwi\text{-}ref}$	Reference PWM currents in *dq* frame
$i_{dg\text{-}ref}$, $i_{qg\text{-}ref}$	References of the *d*- and *q*-axis components of the grid current
i_{cd}, i_{cq}	*d*- and *q*-axis components of the capacitor current
v_{cd}, v_{cq}	*d*- and *q*-axis components of the capacitor voltage
C_f, L_f	Filter capacitor and inductor of the grid-side CSC
ω_g	Angular speed of the grid
m_i	Modulation index
α_i	Delay angle
$I_{dc\text{-}ref}$	DC current reference

θ_g	Grid voltage angle
θ_{wi}	Angle of the PWM current
v_p	generator voltage
$i_s, i_{s1}, i_{s2}\ldots, i_{sn}$	Generator-side AC currents
i_p	primary current of the phase-shifting transformer
$V_{C1}\ldots, V_{Cn}$	DC capacitor voltages
i_g	Load current
L_g	Generator synchronous inductance
$v_{C1}\ldots, v_{Cn}$	AC capacitor voltages
$I_1\ldots, I_n$	DC current of each module
i_g, v_g	Grid-side current and voltage
R_l	Load resistance
$V_{c\text{-}ref}, V_{c\text{-}ref1}, V_{c\text{-}ref2}$	Capacitor voltage references
$i_{ds}, i_{qs}, v_{ds}, v_{qs}$	Generator-side *d*-axis currents and voltages
λ_r	Rotor flux linkage
$T_e, T_{e\text{-}ref}$	Torque and torque reference
θ_r	Rotor position angle
I_{in}	Input DC current
Δd_m	Duty cycle error
d_c	Shared duty cycle
R_p	Extra resistor
$I_{L1}, I_{L2}\ldots I_{Ln}$	Inductor currents
$i_{w1}, i_{w1}\ldots i_{wn}$	PWM output current of each CSC module
i_{out}	Output current
$i_{C1}, i_{C2}\ldots i_{Cn}$	Capacitor currents
V_{in}	Input DC voltage
ω	Angular speed
T_s	Switching period
T_{01}, T_{02}	Zero-stage dwell time

T_1	Active-state dwell time
θ	Phase displacement between capacitor voltage and output current
k	Voltage gain
$\Delta I_{L\mathrm{n}}$	Inductor current ripple
f_{sw}	Switching frequency
R	Load resistor
$v_{C\text{-}peak}$	Positive peak value of v_C
v_s	Voltage stress of switch S_1
V_d	DC voltage of the half bridge converter
h	Number of ON-state half-bridge converters

Chapter 1

Introduction

The pursuit of carbon neutrality on a global scale is driving the development and utilization of renewable energy resources, such as wind energy [1][2]. According to the transmission technologies, existing wind energy conversion systems (WECS) can be classified into high voltage alternating current (HVAC)-based system and high voltage direct current (HVDC)-based system [3-7]. The HVAC technology is suitable for short-distance transmission, featuring a simple structure and low cost. However, as the transmission distance increases, challenges arise in terms of efficiency and reactive power compensation. For long-distance transmission, the HVDC technology is the preferred choice due to its lower cost and higher efficiency compared to the HVAC technology. The existing HVDC-based WECS requires the use of a substation, which is very large and expensive. A new technology, named series-connected HVDC-based WECS, was proposed to address this challenge. It can eliminate the need for the bulky and costly substation, resulting in substantial cost and size reductions. Both voltage source converters (VSCs) and current source converters (CSCs) have been studied for this series-connected HVDC-based WECS. While the CSC features variable DC voltage operation and inherent short-circuit protection [8], making it a promising candidate for the series-connected HVDC-based WECS. However, the use of CSC-based power converters in the series-connected HVDC-based WECS presents several technical challenges. For example, the grid-side power converters require bulky and costly multi-winding transformers, while the generator-side power converters face issues such as highly distorted generator stator currents, low scalability, and/or high complexity. In this thesis, new CSC-based power converters are proposed to address the aforementioned challenges for the series-connected HVDC-based WECS. This chapter begins with a review of the state-of-the-art power converters in the series-connected HVDC-based WECS. On this basis, challenges and objectives of this thesis are presented.

1.1 Configurations of WECS

The configuration of an offshore WECS, as illustrated in Figure 1.1, generally consists of a wind farm, transmission system, grid-side substation, and the grid [9]. The wind farm comprises several turbine-generator-converter units. These units have power converters on the generator side that can produce either AC or DC at their outputs [10-16], and they can be connected either in parallel or in series at the collection point. The transmission system is categorized into HVAC-based and HVDC-based systems, with the former suitable for short-distance transmission and the latter for long-distance transmission. As a result, the WECS can be configured in various ways, including HVAC-based, parallel AC and HVDC-based, parallel DC and HVDC-based, and series DC and HVDC-based configurations [17-39].

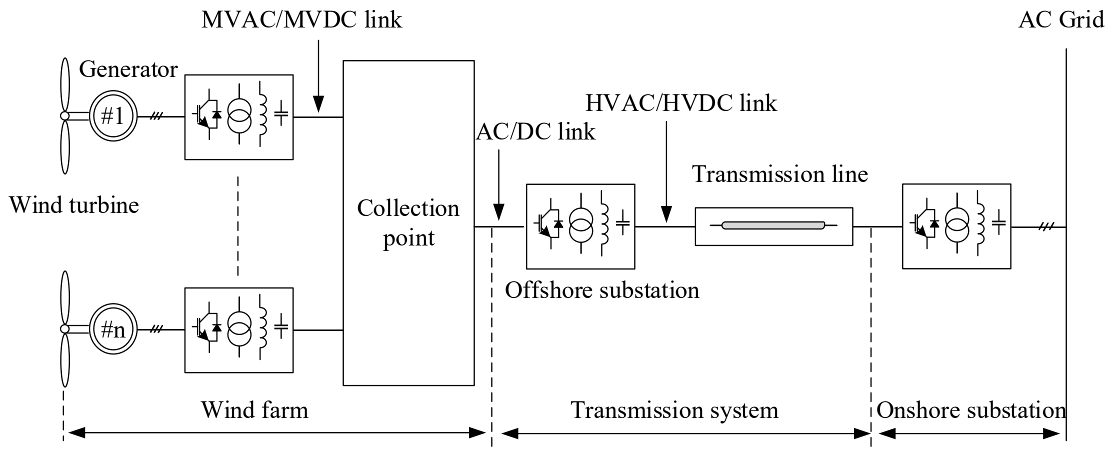

Figure 1.1: Configuration of a wind energy conversion system.

1.1.1 HVAC-based configuration

Figure 1.2 illustrates the HVAC-based configuration [17]. The generator-side power converter is utilized to achieve maximum power point tracking for each turbine-generator unit. The output voltage of each generator-side power converter is elevated to medium-voltage (MV) levels through the step-up transformer and then connected in parallel at the collection point. The MVAC voltage is subsequently stepped up to the HVAC voltage through the second step-up transformer. The generator-side power converter and the first step-up transformer are housed in the nacelle of the wind turbine, while the second step-up transformer, a central transformer, is located at the offshore substation.

The HVAC-based configuration offers several advantages such as well-proven technology and low initial and maintenance costs, making it well-suited for WECS with short-distance power transmission. Some onshore wind farms and offshore wind farms, situated near the shore, adopt this configuration. For instance, the Horns Rev offshore wind farm[18], with a total power rating of approximately 800 MW across its three projects [19], is located approximately 20 km off the coast and utilizes HVAC technology.

However, when applied to long-distance transmission, the HVAC-based WECS faces several technical challenges, including high power losses, significant voltage drops, the requirement of reactive power compensation, limited power transmission capacity, and grid synchronization issues. These challenges make the HVAC-based WECS less competitive in long-distance transmission. Typically, an HVAC-based system is employed in wind farms with a shorter transmission distance, and the power rating of the wind farm also plays an important role when choosing the transmission system.

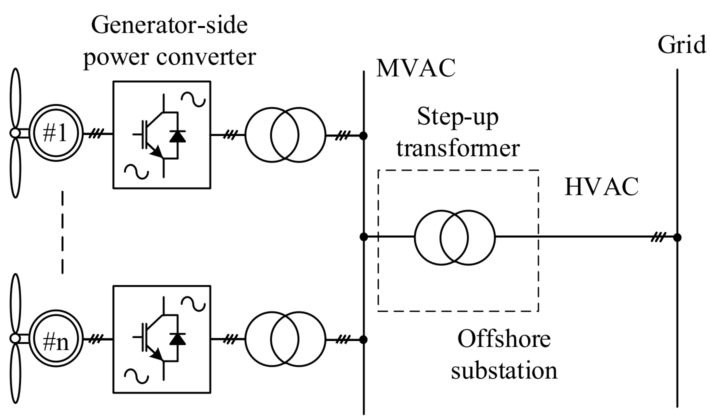

Figure 1.2: HVAC-based configuration.

1.1.2 Parallel AC and HVDC-based configuration

For long-distance transmission, the HVDC technology offers several advantages over the HVAC system, including lower power loss, reduced cost, higher transmission capacity, and decoupling between the two sides of the transmission line. Figure 1.3 shows the parallel AC and HVDC-based configuration [20-24]. The same as the HVAC technology, a step-up transformer is employed for each turbine-generator unit to boost its LV output to an MVAC level. The MVAC is further stepped up to HVAC by another step-up transformer and then converted to HVDC through the

HVDC converter. The HVDC is converted back to HVAC at the receiving end of the transmission line by the grid-side HVDC converter and is then stepped down to match the grid voltage. The generator and generator-side power converter as well as the first transformer are installed in the nacelle, while the second transformer and the HVDC converter [78] are housed in the offshore substation.

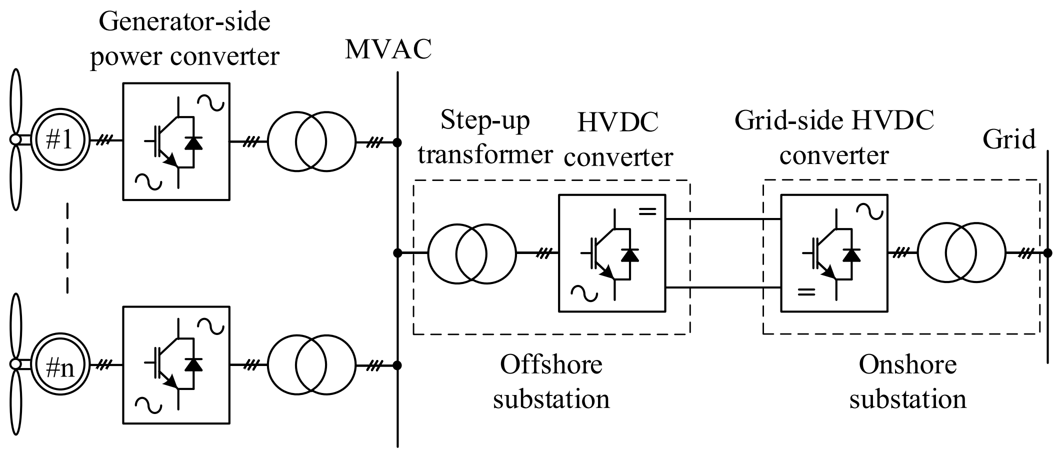

Figure 1.3: Parallel AC and HVDC-based configuration.

In the wind market, the HVDC converter can be either the line commutated converter (LCC) or voltage source converters (VSC). The LCC-based HVDC [73] system needs reactive power compensation, and its active and reactive power cannot be controlled separately. The VSC including 2-level VSC [74-77] and modular multilevel converters (MMC) [70][71] are widely used in wind energy projects. Compared with the 2-level VSC which requires the use of series-connected switches and complicated and expensive voltage balancing schemes, the MMC represents a significant advancement in VSC technology, known for its modular structure eliminating the series-connected switches, high reliability, high scalability, high efficiency, and generation of close-to-sinusoidal waveforms. However, a large number of redundancy designs are needed, and the initial and maintenance costs are substantial. To address the challenges of LCC and VSC, while retaining their advantages, hybrid converters consisting of both of LCC and VSC were reported [72]. Also, CSC has been studied for the use in this configuration [61].

The parallel AC and HVDC-based technology is dominant in the market of the WECS. However, its biggest challenge is the need for the very bulky and costly offshore substation.

Furthermore, the involvement of multiple power conversion stages leads to reduced efficiency and increased complexity.

1.1.3 Parallel DC and HVDC-based configuration

The parallel DC and HVDC-based configuration [25-30] as shown in Figure 1.4, was developed to reduce the size and cost of the offshore substation used in the parallel AC and HVDC-based WECS. As depicted in Figure 1.4, each turbine-generator unit utilizes an isolated DC-DC converter instead of employing a low-frequency step-up transformer to boost LVDC to MVDC levels at the MVDC collection point. The DC collection offers increased efficiency of the system and the flexibility of interconnecting different networks. The MVDC is boosted to the HVDC level by a central isolated DC-DC converter and then transmitted to onshore substation. The isolated DC-DC converters including the generator-side DC-DC converter and the central DC-DC converter, are multiple-stage power converters, consisting of a DC/AC converter, a high/medium-frequency transformer, and an AC/DC converter. The high/medium-frequency transformers feature a smaller size than the low-frequency transformers used in parallel AC and HVDC-based configuration, resulting in a reduced footprint of the magnetic components. The resultant size and cost of the offshore substation are therefore reduced. However, the multiple power conversions of the isolated DC-DC converters suffer from increased power losses. In addition, manufacturing of high-frequency transformers with high-power and high-voltage insulation levels is not yet mature.

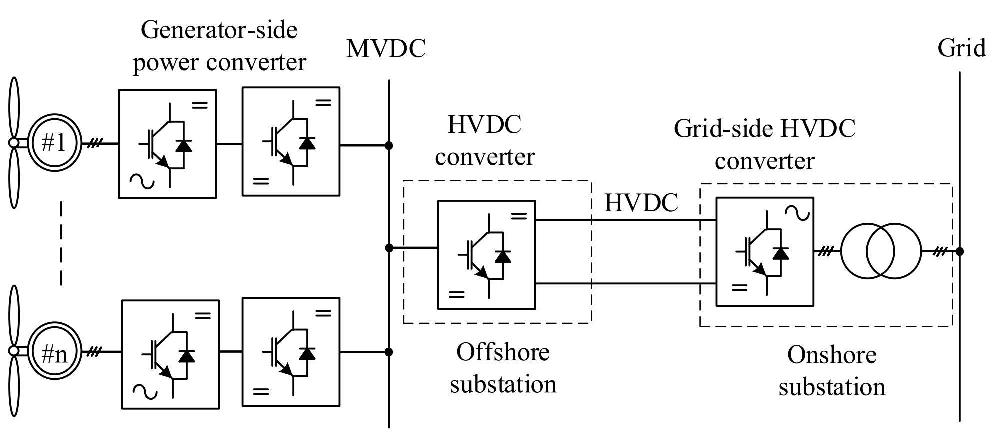

Figure 1.4: Parallel DC and HVDC-based configuration.

1.1.4 Series DC and HVDC-based configuration

A series DC and HVDC-based configuration [31-55] was proposed to eliminate the offshore substation. As shown in Figure 1.5, the outputs of the generator-side converters are connected in series to achieve an HVDC level. As a result, the need for the bulky and costly offshore substation is eliminated, resulting in a substantial reduction in cost and footprint. Moreover, this configuration involves fewer power conversion stages, leading to a reduction in complexity and an improvement in efficiency.

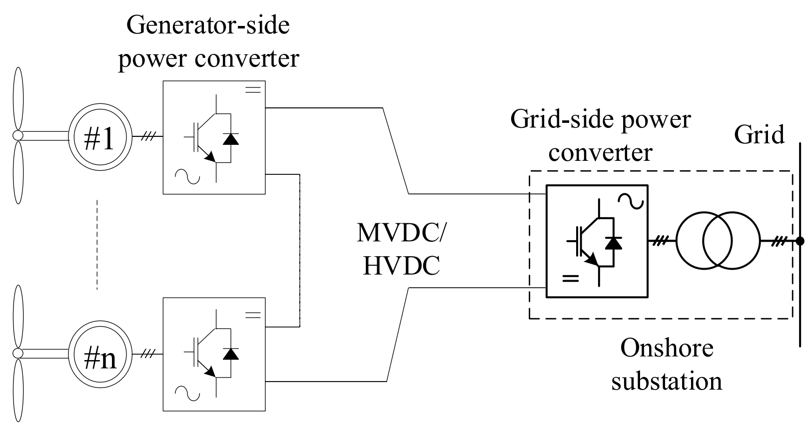

Figure 1.5: Series DC and HVDC-based configuration.

In summary, among these configurations, the series DC and HVDC-based configuration offers the elimination of the bulky and costly offshore substation, along with a reduction in power losses, making it a highly promising candidate for the next generation of WECS.

The series-parallel connected configuration [56-57] also been studied to increase the power rating of the whole wind farm.

1.2 Power converters in series DC and HVDC-based WECS

The power converters used in the series DC and HVDC-based WECS include the generator-side converter and the grid-side converter. The generator-side converter is to control the generator speed to achieve the maximum power point tracking (MPPT), while the grid-side converter is responsible for controls of the DC-link voltage (or current) and the reactive power. According to the types of the grid-side converter, the series DC and HVDC-based WECS can be classified into

VSC-type and CSC-type series DC-based WECS. This section reviews state-of-the-art power converters that have been proposed for both types of series DC-based WECS.

1.2.1 Power converters in VSC-type series DC-based WECS

For the VSC-type series DC-based WECS, the reported grid-side power converters mainly include the conventional 2-level VSC [32-34] and the MMC [36-38], while the generator-side power converters range from passive converters [88][89] to active converters [42][86].

Figure 1.6 shows the 2-level VSC [85] used as the grid-side converter. The converter has a simple structure but requires the use of series-connected switches to withstand the high DC-link voltage. The use of the series-connected switches suffers from voltage imbalance issues, resulting in the need for complicated and expensive voltage balancing schemes. Meanwhile, the output voltage of a 2-level VSC contains substantial low-order harmonics, leading to the need for a large AC filter. Despite these challenges, 2-level VSC technology has demonstrated maturity and successful application in HVDC systems, making it a viable option for extension into the series DC-based WECS.

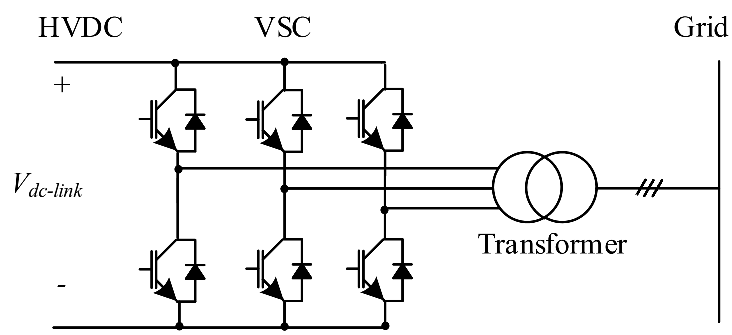

Figure 1.6: Grid-side converter: 2-level VSC.

The modular multilevel converter (MMC) as shown in Figure 1.7 represents a significant milestone in VSC development. The submodule of the MMC can be a half-bridge, a full-bridge, or a neutral point clamping converter. Unlike the 2-level VSC, the MMC doesn't require series-connected switches, eliminating the need for voltage balancing schemes. Additionally, in comparison to the 2-level VSC, it generates a multi-level output exhibiting superior harmonic performance at a reduced switching frequency, leading to reduced switching loss and smaller filter size. Overall, the MMC features a modular structure, high reliability, high scalability, and high efficiency [70][71]. It is a well-proven converter in the HVDC systems in industry, and a better candidate for the use in the series DC-based WECS compared with the 2-level VSC.

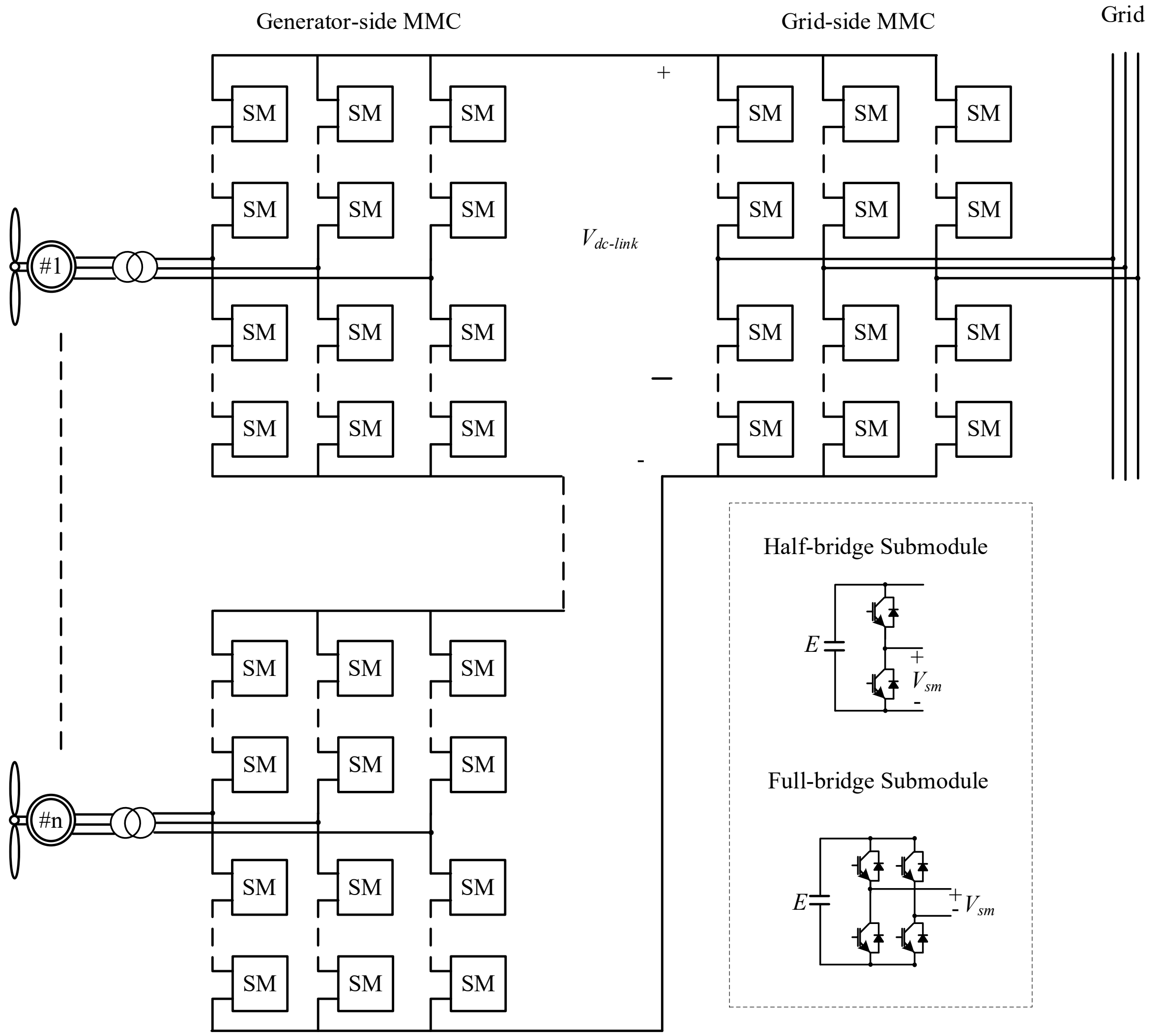

Figure 1.7: MMC-based series-connected WECS.

In the series DC-based WECS, the generator that is the farthest to the ground must withstand a voltage of an HVDC level, which is impractical for the generator. To solve this issue, a practical solution is to use a transformer. The transformer is employed to isolate the generator from the HVDC level, and as a result, the generator with regular insulation levels can be employed in the series DC-based WECS. According to the types of transformers, the generator-side converters are classified into low-frequency transformer (LFT)-based and medium-frequency transformer (MFT)-based converters.

Figure 1.8 illustrates an LFT-based converter. The LFT is connected between the generator and the generator-side converter to provide the isolation. The generator-side converter is a passive rectifier, featuring simple structure, high reliability, scalability, and low cost. However, it generates highly distorted generator stator currents, leading to increased thermal and mechanical stress as well as shortened lifespan of the generator. Another disadvantage of the use of a passive power converter is that it is only suitable for the synchronous generator (SG)-based WECS. In addition, the lack of generator-side control results in the fact that the generator-side MPPT and the grid-side real and reactive power controls cannot be guaranteed simultaneously under low wind speeds.

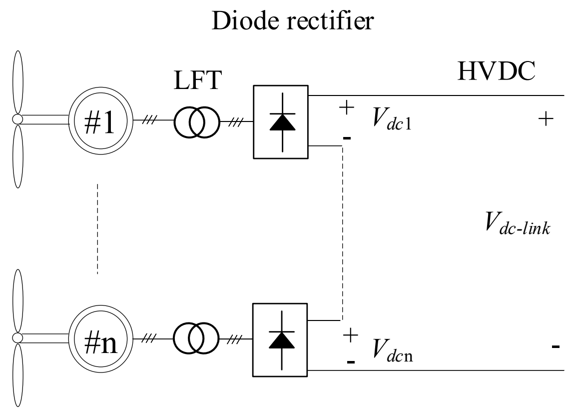

Figure 1.8: LFT-based generator-side converter: Passive rectifier.

Figure 1.9 shows an improved version of the previously discussed LFT-based converter, where a boost DC-DC converter is added on the generator side [88][89]. The boost DC-DC converter is used to control the generator speed to achieve the MPPT, while the grid-side real and reactive power controls are achieved by the grid-side converter. As a result, the generator-side and the grid-side controls can be achieved simultaneously in the full operation range [106]. The advantages associated with the use of a passive rectifier are retained, while the disadvantages, such as highly distorted generator stator currents and limited application to SG-based WECS, still exist.

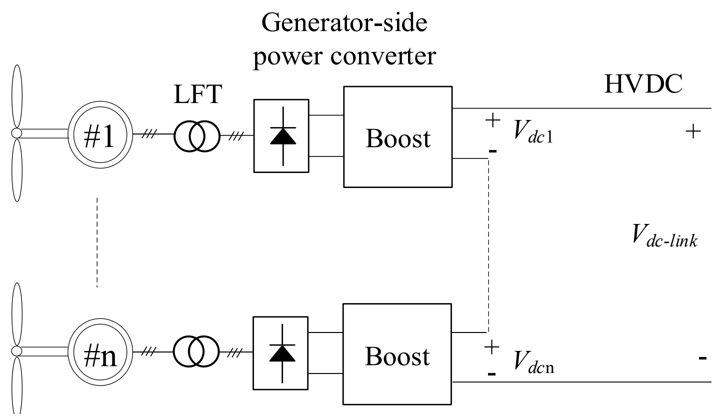

Figure 1.9: LFT-based generator-side converter: Passive rectifier + boost DC-DC converter.

Figure 1.10 shows the active rectifier version of the LFT-based generator-side converter, where both 2-level and multi-level converters can be employed. The 2-level converter is a well-suited converter for LV turbine-generator systems, while the three-level NPC is suitable for MV turbine-generator systems. The use of a MMC was also discussed in the literature [36-38]. Compared with the passive rectifier, these active rectifiers can ensure generator-side and grid-side controls simultaneously without the need for extra DC-DC converters. Another benefit of using active rectifiers is that they can be utilized for both SG-based, and induction generator (IG)-based WECS. In addition, active rectifiers offer superior harmonic performance. Penalties associated with the use of active rectifiers include higher costs, lower efficiency, and more complex control requirements.

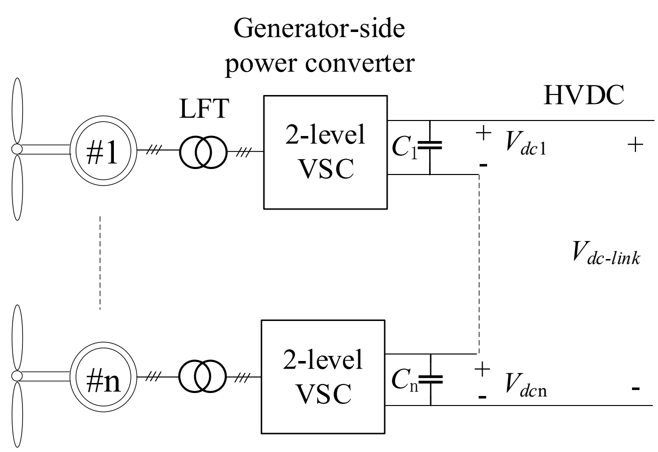

Figure 1.10: LFT-based generator-side converter: Active rectifier.

The LFT-based converters are mature technology and widely used in existing WECS, but with a large size and weight of LFT. On the other hand, the MFT-based converters see potential in reducing size and weight, making them an attractive solution for WECS where the space of the wind turbine nacelle is limited. However, the high-power, high-voltage insulated MFT is not mature technology yet.

Figure 1.11 shows an MFT-based generator-side converter [42].It consists of a reduced matrix converter (RMC), a single-phase MFT, and a diode bridge. The single-phase MFT is used to isolate the generator from the HVDC level, while the RMC is for generator speed control. The RMC has a small size due to the elimination of DC-link capacitors and offers high efficiency because of its direct power conversion. However, it requires a high number of switches, complex control schemes, and the need for overvoltage protection. Similar MFT-based converters were developed for the series DC-based WECS. For example, Figure 1.12 shows such an MFT-based converter, where a 2-level VSC followed by an isolated H-bridge converter is employed [86]. Compared with the RMC, it offers better harmonic performance and easier control, but features a lower efficiency due to the employment of more power conversion stages. Additionally, VSC and HB converters are widely used in the industry, while commercially ready solutions for matrix converters are limited.

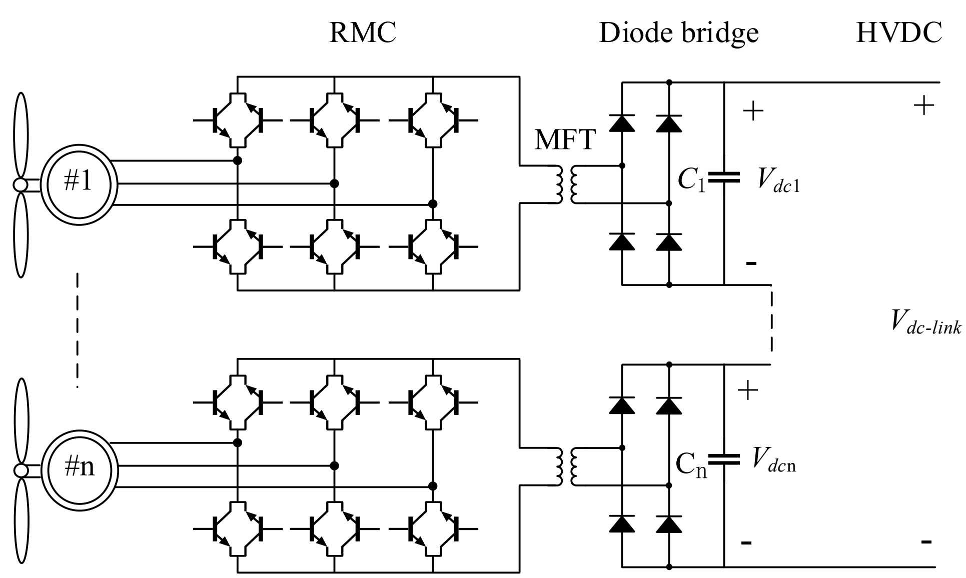

Figure 1.11: MFT-based generator-side converter: Reduced matrix converter.

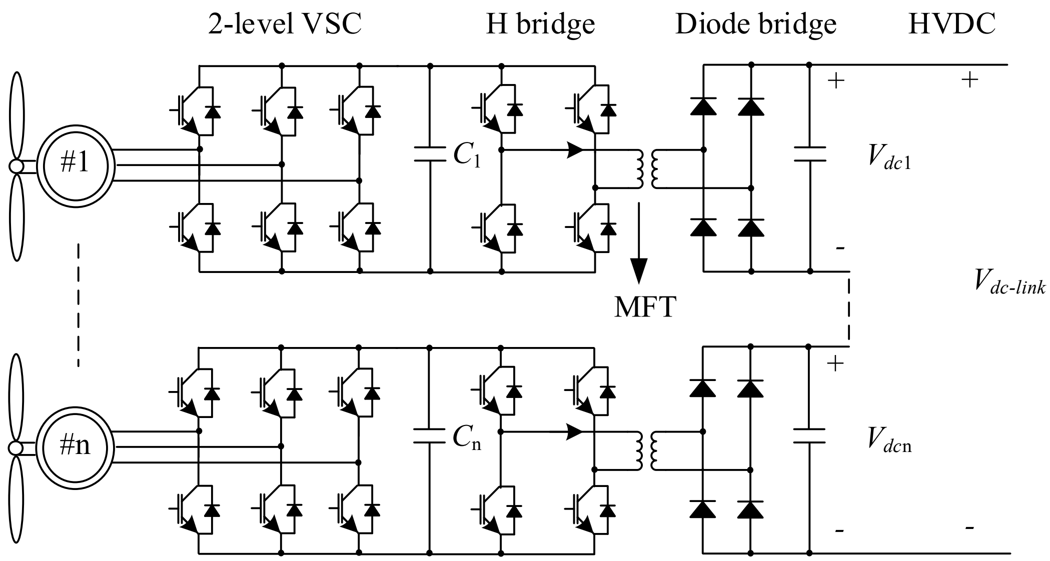

Figure 1.12: MFT-based generator-side converter: 2-level VSC.

The above MFT-based converters all utilize a single-phase MFT, which can be extended to its three-phase version, as shown in Figure 1.13 [41][86]. By doing so, the power density of the generator-side converter is increased. What is more, the use of a dual active bridge (DAB) allows bidirectional power flow for the system, contributing to the startup and fault ride through (FRT) of the WECS. On the other hand, the use of the DAB converter results in a higher cost and a lower efficiency as well as the requirement for more complex control schemes than the 2-level VSC-based version shown in Figure 1.12 and the RMC-based one shown in Figure 1.11.

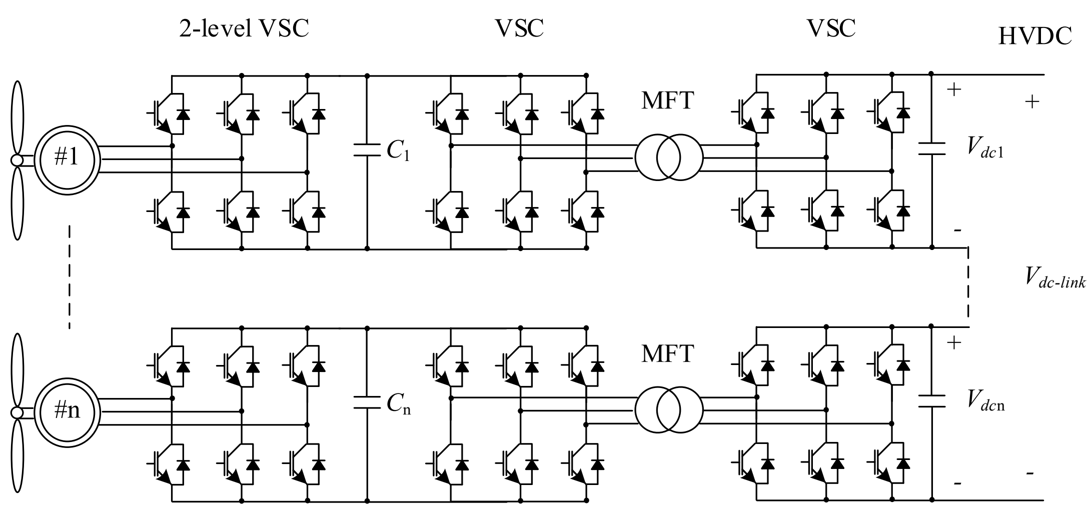

Figure 1.13: MFT-based generator-side converter: Three-phase MFT.

1.2.2 Power converters in CSC-type series DC-based WECS

CSCs are mature technology [64-65], and widely used in MV drive [8]. Figure 1.14 shows a CSC-type series DC-based WECS, where line-commutated CSCs (LCC) are employed on both generator and grid sides [46][47]. On the generator side, a number of generator-side LCCs are connected in series to form an HVDC level, while only one LCC is employed on the grid side. The LFT is used on the generator side to allow the use of generators with regular insulation levels. On the grid side, the synchronous compensator is employed to provide the reactive power compensation for the LCC. LCC technology is well-proven in HVDC transmission systems. Its advantages including simple structure, reliable short-circuit protection, and large power capacity are well retained when using for the series DC-based WECS, and the same for its disadvantages such as the need for a relatively strong synchronous voltage source in order to commutate, the requirement for reactive power compensation as well as bulky and costly filters, and the lack of independent real and reactive power control.

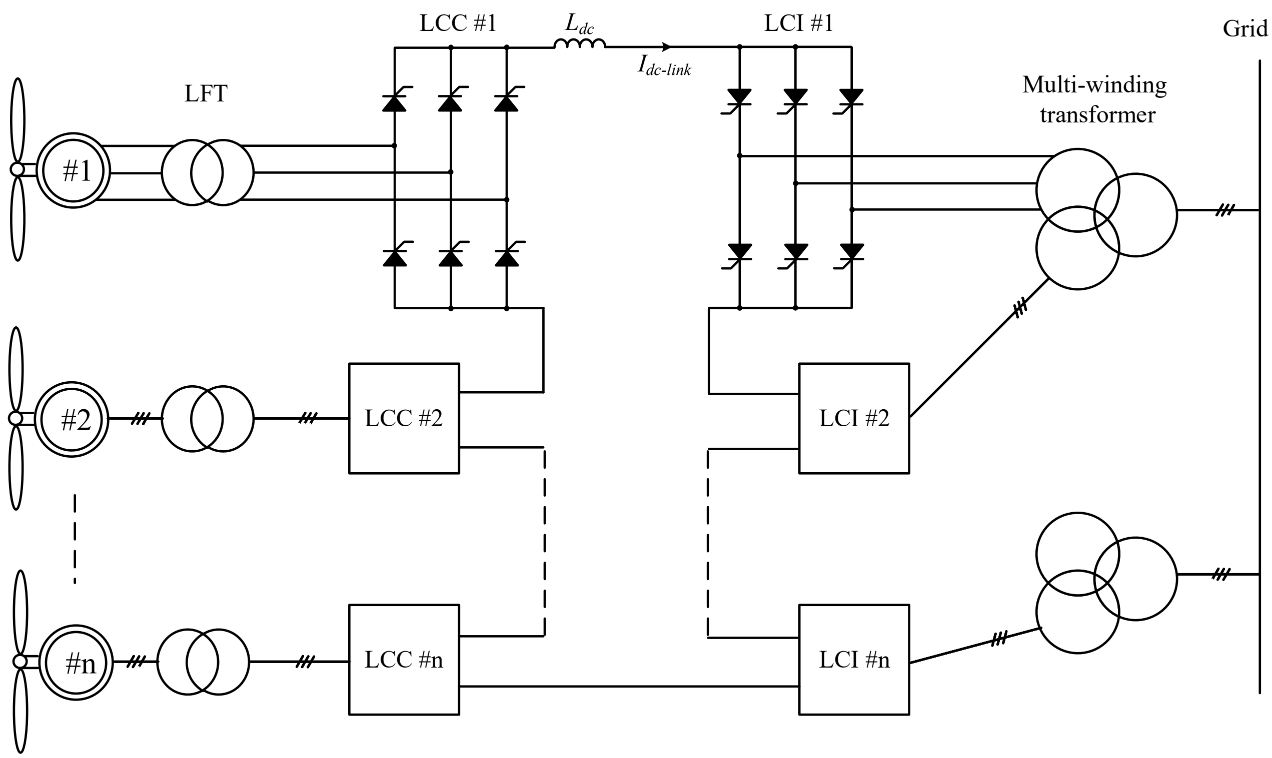

Figure 1.14: CSC-type WECS: LCC.

Figure 1.15 shows the PWM CSC-based version of the CSC-type WECS [50-51]. On the grid side, a number of PWM CSCs are connected in series at inputs to withstand the HVDC level and in parallel at outputs through multi-winding transformers. On the generator side, the PWM CSC is employed at each turbine-generator unit, The outputs of these generator-side PWM CSCs are connected in series to realize an HVDC level. The generator-side converter is for the generator speed control, and the grid-side series-connected PWM CSCs are for the real and reactive power controls. Each PWM CSC is composed of six symmetrical gate commutated thyristors (SGCT). Each SGCT can be replaced with two or three SGCTs connected in series to achieve higher voltage operation. The switching frequency of the PWM CSC is around several hundred hertz to reduce power losses. The PWM CSC-based WECS addresses the challenges of the LCC-based WECS while retaining its advantages. For example, it achieves independent real and reactive power controls, eliminating the need for reactive power compensation. Second, it offers better harmonics performance, leading to the use of smaller AC filters. Moreover, its switches are self-extinguishing, eliminating the need for a strong grid voltage for commutation. Advantages of CSCs such as inherent short-circuit protection and grid-friendly waveform are retained. On the other hand, one of the disadvantages of the PWM CSC-based WECS is the use of bulky and costly multi-winding transformers on the grid side.

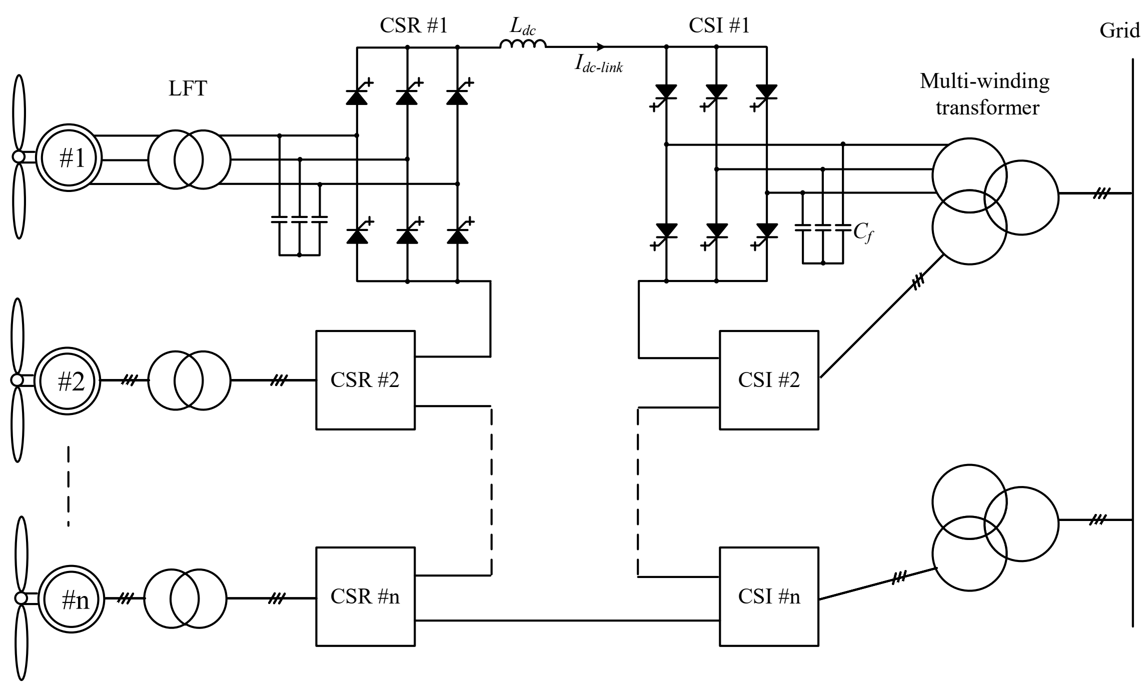

Figure 1.15: CSC-type WECS: PWM CSC.

A simplified version of the PWM CSC-based WECS was developed, as shown in Figure 1.16. On the grid side, the system employs the same series-connected PWM CSCs, while on the generator side, a diode rectifier is used instead of the PWM CSC. The substitution of the PWM CSC with a diode rectifier provides several advantages, including lower cost, a smaller converter size, enhanced reliability and scalability, and reduced complexity. However, it comes with the drawbacks of highly distorted generator stator currents and a lack of guaranteed MPPT under low speeds. Like the VSC-type WECS, a DC-DC converter can be added on the generator side to achieve the MPPT under low speeds, while retaining all the advantages of the diode rectifier. Unlike the VSC-type WECS where a boost DC-DC is used, a buck DC-DC converter is needed for the CSC-type WECS. The power converter with such a buck DC-DC converter [89] is shown in Figure 1.17.

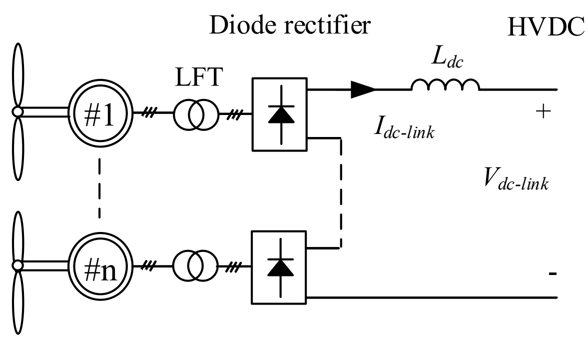

Figure 1.16: CSC-type WECS: Simplified version using a diode rectifier.

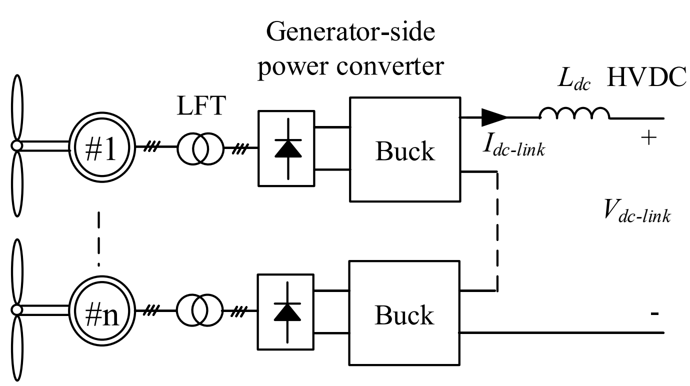

Figure 1.17: CSC-type WECS: Simplified version using a diode rectifier and a buck DC-DC converter.

The same as the VSC-type WECS, the CSC-type WECS also utilizes transformers to isolate the generators from the HVDC level to allow the use of generators with regular insulation levels. For example, the LCC-based WECS shown in Figure 1.14, the PWM CSC-based WECS shown in Figure 1.15, and the simplified versions shown in Figure 1.16 and Figure 1.17 all utilize an LFT. On the other hand, Figure 1.18 shows an MFT-based PWM CSC proposed for the CSC-type WECS [41-43]. It utilizes an RMC on the generator side and the same PWM CSCs on the grid side. The use of an RMC ensures MPPT in the full operation range, but the utilization of a single MFT leads to a significant burden for the MFT manufacturing. The KVA of the single MFT is the same as that of each turbine-generator unit, that is a megawatts level. The manufacturing of such a high-power MFT with an HVDC-level insulation requirement is not mature.

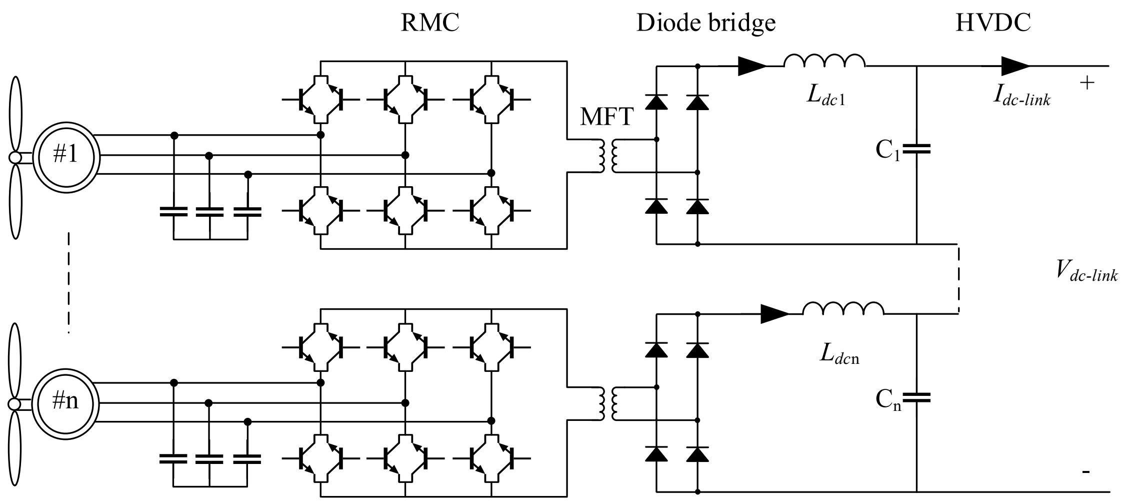

Figure 1.18: CSC-type WECS: Single-phase MFT.

Like the VSC-type WECS, a three-phase MFT version of the PWM CSC-type WECS was proposed as shown in Figure 1.19. The use of a three-phase MFT is expected to achieve higher power density in comparison with a single-phase MFT[41].

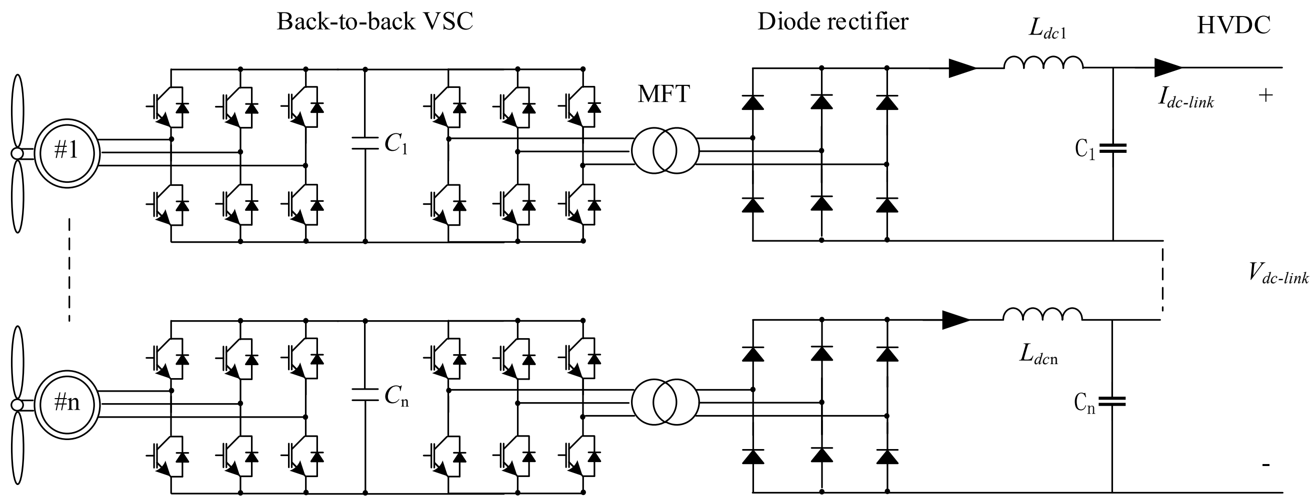

Figure 1.19: CSC-type WECS: Three-phase MFT.

To reduce the manufacturing burden of the high-power high-voltage insulated MFT, a modular MFT-based converter was developed for the PWM CSC-based WECS as shown in Figure 1.20 [52][53]. This converter utilizes a modular isolated DC-DC converter where multiple MFTs are employed. The use of multiple MFTs reduces the KVA of each MFT, thereby decreasing its manufacturing burden. Furthermore, the modular structure enables the use of low-cost low-voltage switches and enhances the reliability of the conversion system. Compared with the active rectifier-based converters as shown in Figure 1.18 and Figure 1.19, the use of the diode rectifier, however, leads to highly distorted generator stator currents.

There are also some CSC-type converters [60] [63] [80-83] [97-102], including multi-level CSCs which are developed for the MV and HV applications. Some of these converters can be potentially used in the WECS.

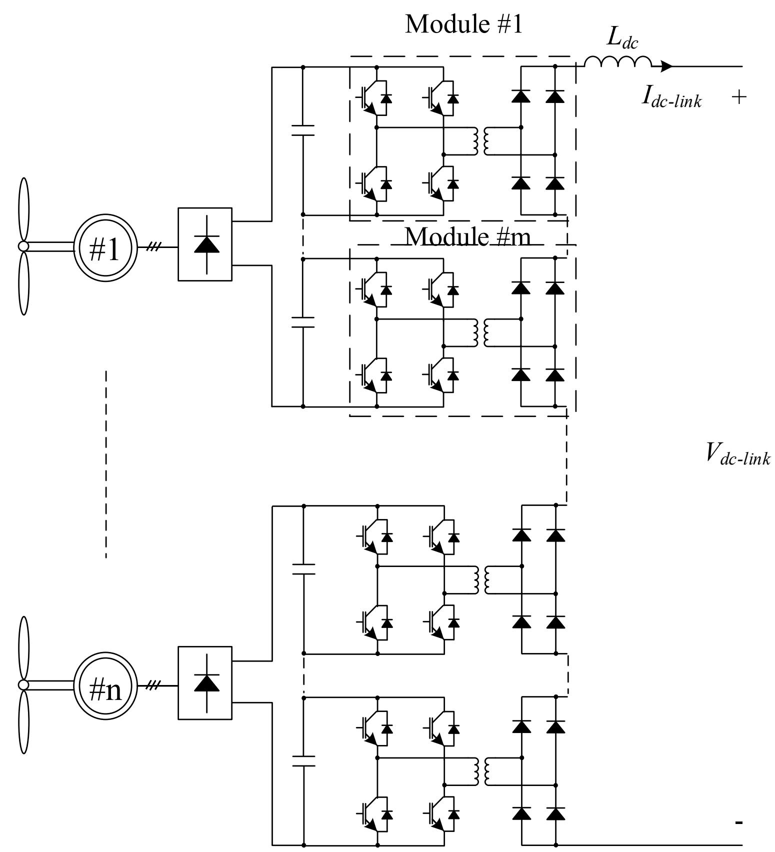

Figure 1.20: CSC-type WECS: Modular isolated DC-DC converter.

1.2.3 Comparisons between VSC-type and CSC-type series DC-based WECS

VSCs are dominant and well-proven converters in existing WECS, while their application in series DC and HVDC-based WECS presents two technical challenges: ensuring a constant DC-link voltage and achieving MPPT for all turbine-generator units. The DC-link voltage must be controlled as a constant to ensure grid connection. And this constant DC-link voltage should be evenly distributed among generator-side power converters. It requires that each generator-side power converter needs to ensure a constant DC voltage at its output under all conditions. Meanwhile, the unique series connection of generator-side power converters results in the fact that they share the same DC-link current at their outputs. However, such identical DC voltages and identical DC currents at the outputs of all generator-side power converters cannot be achieved simultaneously under different wind speeds. In practice, wind speeds at different wind turbines could be different. The achievement of MPPT for all turbine-generator systems under different wind speeds results in different output DC voltages at different generator-side power converters.

This in turn results in that the constant DC-link voltage cannot be ensured under different wind speeds. The same conclusion will be received under faults, in which one or more generator-side power converters are bypassed due to failure and the remaining healthy power converters cannot realize the same constant DC-link voltage. In turn, to ensure a constant DC-link voltage, MPPT cannot be obtained for all turbine-generator units under different wind speeds.

On the other hand, CSCs can effectively address the aforementioned challenges associated with the application of VSCs in series DC and HVDC-based WECS. A unique feature of CSCs is variable DC-link operation, allowing the achievement of MPPT control for all turbine-generator units under various conditions. Additionally, faulty generator-side power converters can be bypassed without causing overvoltage issues for the remaining healthy units. Such inherent advantages of the CSC-type WECS make it a highly promising candidate for the next generation of series DC and HVDC-based WECS.

1.3 Thesis objectives

1.3.1 Technical challenges and thesis objectives

The grid-side series-connected PWM CSCs require the use of multi-winding transformers to provide an independent current path for each PWM CSC, enabling series connection at their inputs and parallel connection at their outputs. However, these multi-winding transformers are bulky and costly. Eliminating multi-winding transformers would lead to significant reductions in both cost and footprint. Therefore, one objective of this thesis research is to develop transformerless series-connected PWM CSCs.

Various generator-side power converters have been proposed for PWM CSC-type WECS, including LFT-based converters and MFT-based converters. Each type of converter can be further divided into passive rectifier-based and active rectifier-based converters. While LFT is a mature technology, it suffers from a large footprint. On the other hand, MFT offers a smaller size and weight but is not yet a mature technology. Active rectifiers exhibit superior performance in terms of generator stator harmonics compared to passive rectifiers. However, they cannot surpass passive rectifiers in terms of cost, reliability, scalability, and efficiency. Hence, the second objective of this thesis research is to develop innovative generator-side power converters that effectively address the challenges of LFT/MFT and passive/active rectifier-based converters while retaining their respective advantages.

In summary, the objectives of this thesis research are to develop new generator-side power converters and grid-side power converters for the PWM CSC-type series DC and HVDC-based WECS, as shown in Figure 1.21.

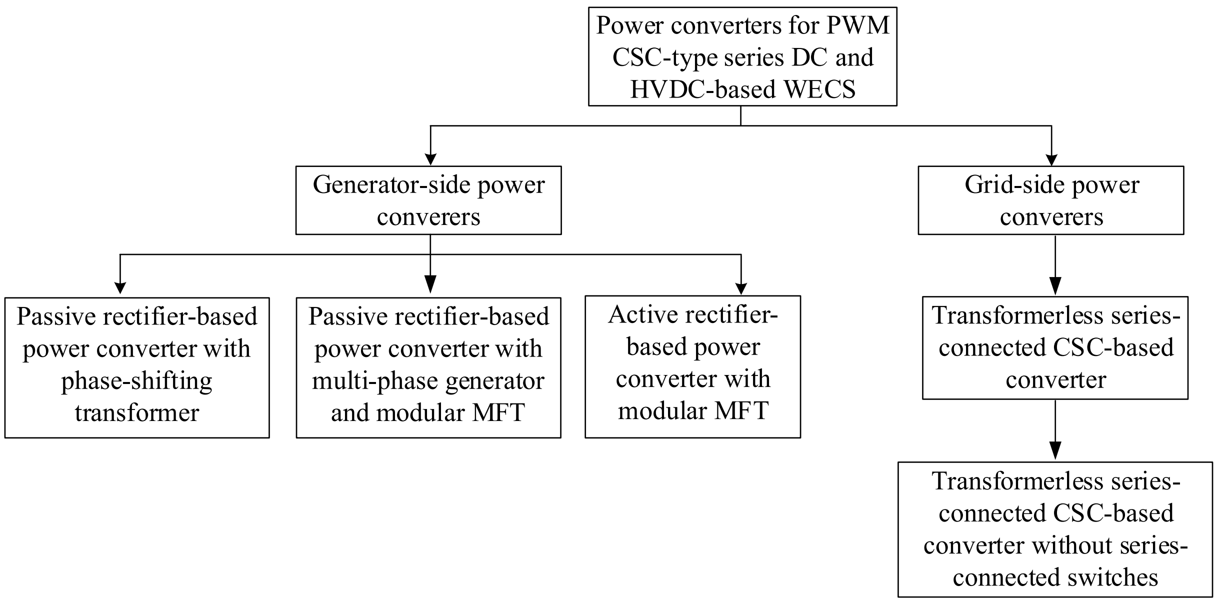

Figure 1.21: Thesis objectives.

1.3.2 Thesis layout

This thesis consists of seven chapters as follows.

Chapter 1: The state-of-the-art power converters in series DC and HVDC-based WECS are reviewed.

Chapter 2: A passive rectifier-based converter with the use of a phase-shifting transformer is proposed for the generator side converter of the CSC-type series DC-based WECS. It effectively addresses the disadvantage of highly distorted generator stator currents associated with passive rectifiers, while retaining all their advantages including low cost, high reliability, simplicity, and scalability.

Chapter 3: A passive rectifier-based converter using a multi-phase generator and modular medium-frequency transformers (MFTs) is proposed for the generator-side converter. Compared with the proposed phase-shifting transformer-based converter, it offers reduced size and weight, contributing to reduced construction burden of WECS. All the advantages of the phase-shifting transformer-based converter are retained.

Chapter 4: An active rectifier-based converter using modular MFTs is also proposed for the generator-side converter of the CSC-type WECS. The use of an active rectifier ensures superior harmonic performance in the generator stator currents, while the use of modular MFTs contributes to size and weight reductions in the generator-side conversion system. This converter offers benefits of both active rectifiers and MFTs simultaneously.

Chapter 5: Transformerless series-connected CSCs are proposed for the grid-side converter of the CSC-type WECS. The proposed transformerless CSCs are the first to eliminate the need for transformers in series-connected CSCs. This elimination yields substantial cost and size reductions.

Chapter 6: A modified version of the transformerless CSCs is proposed. Compared with the original converter, this modification eliminates the need for series-connected switches by using cascaded half-bridge converter, thereby eliminating the requirement for expensive and complex voltage balancing schemes, while retaining all the advantages of the original converter.

Chapter 7: Contributions and conclusions are drawn from the thesis research.

Chapter 2

Generator-Side Passive Rectifier-Based Converter with Phase-Shifting Transformer

In the CSC-type series DC-based WECS, the LFT and passive rectifier-based converters are well-discussed converters used on the generator side. They provide several advantages. The use of an LFT on the generator side offers a practical solution for addressing the generator insulation issue. Meanwhile, the passive rectifier is characterized by its low cost, simplicity, high reliability, and scalability. However, employing the passive rectifier results in highly distorted generator stator currents, leading to significant torque ripples and a reduced lifespan of the generator. To overcome this issue, a new generator-side power converter is proposed. It delivers superior harmonic performance of the generator stator current while retaining all the benefits of the passive rectifier. This chapter begins with an introduction to the proposed power converter, including its operation principles, features, and device selection criteria. Subsequently, the control scheme is presented, wherein a DC-link current minimization strategy is applied. Finally, the performance of the proposed converter is validated through both simulations and laboratory-scale experiments.

2.1 Existing LFT and passive rectifier-based converters

Figure 2.1 shows the configuration of an existing CSC-type series DC-based WECS. The outputs of the generator-side converters are connected in series to reach the HVDC level. The grid-side CSCs are connected in series at their inputs and in parallel at their outputs through the multi-winding transformer. The generator-side converters at different turbine-generator units are identical, with each comprising an LFT and a passive rectifier plus a Buck converter (optional). The CSC modules employed on the grid side are also identical, each carrying the same power. The number of CSC modules on the grid side is equal to that of the generator-side converters. Note that #n represents the n^{th} turbine-generator unit.

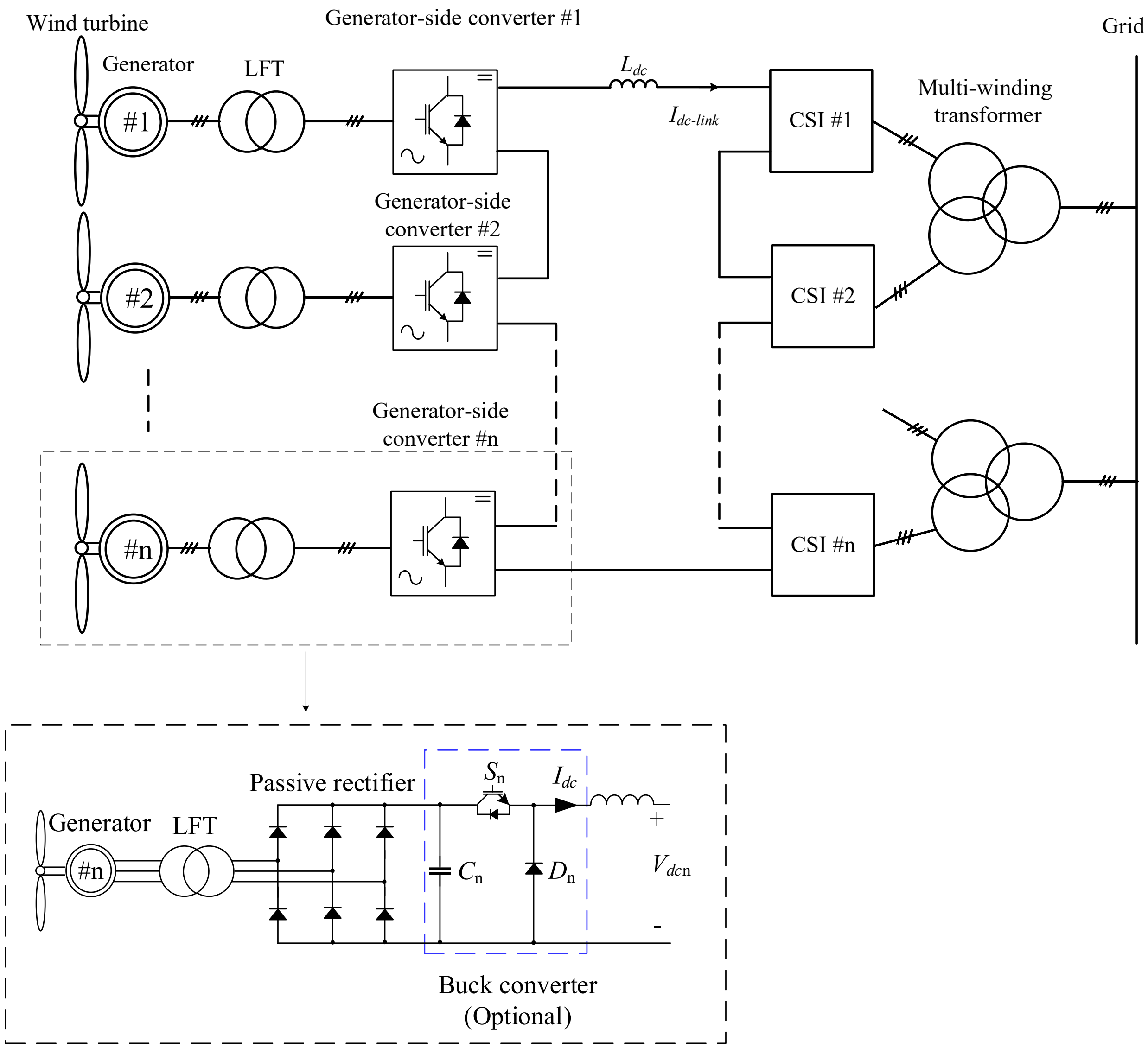

Figure 2.1: CSC-type series DC-based WECS: System configuration; Simplified generator-side conversion for turbine-generator unit #n, with existing LFT and passive rectifier-based converters.

As shown in Figure 2.1, on the grid side, the conventional CSC is employed. On the generator side, the LFT, a mature technology, is used to isolate the generator #n from HVDC to allow the use of generators with regular insulation levels. While the use of a passive rectifier offers low cost, high simplicity, reliability, and scalability, it results in highly distorted generator stator currents, leading to significant torque ripples and a reduced lifespan of the generator.

2.2 Phase-shifting transformer-based converter

To address the aforementioned challenges associated with LFT and passive rectifier-based converters, while retaining their advantages, a phase-shifting transformer-based converter is proposed, as depicted in Figure 2.2, where the turbine-generator unit #n is provided as an example. In this new converter, the grid-side converter remains the CSC, consistent with the existing configuration shown in Figure 2.1, while a new generator-side converter is introduced. This new generator-side converter comprises a phase-shifting transformer, a multi-pulse diode rectifier, and a cascaded DC-DC converter.

The use of diode rectifiers in this new converter allows it to maintain advantages associated with diode rectifiers, including low cost, high reliability, and scalability. Additionally, employing a DC-DC converter ensures the achievement of MPPT, same as existing converters. Similar to the LFT, the phase-shifting transformer in this new converter also serves functions of isolation and voltage regulation. Firstly, by utilizing the transformer, the generator is effectively isolated from the HVDC, allowing for the use of generators with regular insulation levels in the series-connected wind system. Secondly, in medium-voltage (MV) turbine-generator systems, the transformer steps down the input MV to low-voltage (LV) values, enabling the use of LV class components.

A unique role that the phase-shifting transformer plays is current harmonics elimination. The phase-shifting transformer can eliminate specific current harmonics generated by the passive rectifiers. For example, the 5^{th} and 7^{th} harmonics are eliminated by a 12-pulse diode rectifier (a phase-shifting transformer with 2 sets of secondary windings), and the 5^{th}, 7^{th}, 11^{th}, and 13^{th} harmonics are eliminated by an 18-pulse diode rectifier (a phase-shifting transformer with 3 sets of secondary windings). The elimination of these current harmonics improves generator stator current harmonic performance and ultimately enhances the lifespan of the generator. Like the LFT, the phase-shifting transformer is also a mature and well-proven technology in industry. Given the same power rating and insulation level, the cost and size of the two types of transformers are with no significant differences. Therefore, the utilization of a phase-shifting transformer effectively addresses the challenge of highly distorted currents associated with the LFT and diode rectifier-based converters.

Depending on the used DC-DC converter, the proposed generator-side converter is extended to three versions.

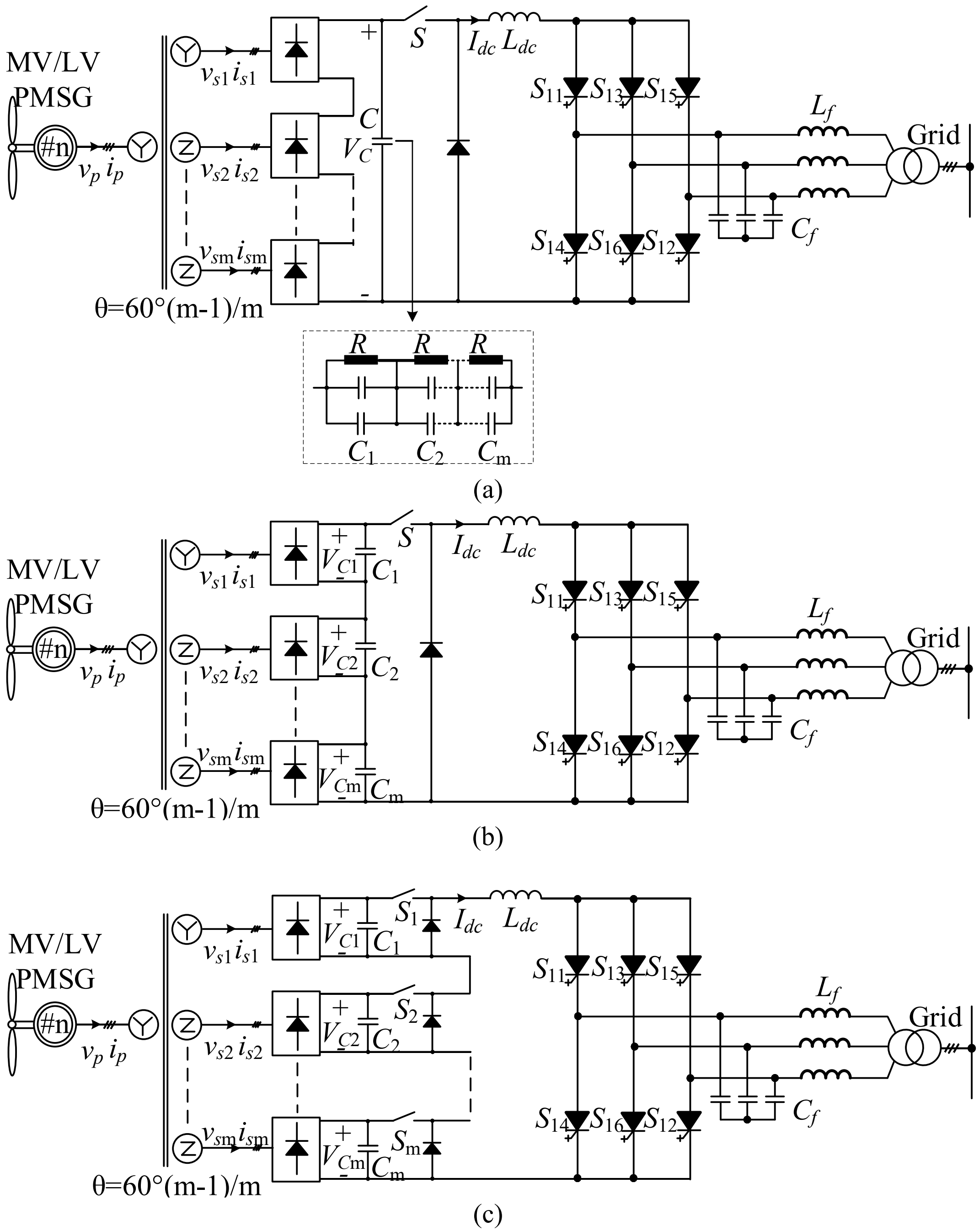

Figure 2.2: Proposed generator-side power converter: (a) Version 1, (b) Version 2, and (c) Version 3.

Version 1: The outputs of the diode rectifiers are connected in series and then connected to a conventional Buck converter. It faces two challenges for medium-voltage high-power applications. Firstly, the capacitor C is realized by series/parallel-connected capacitors, necessitating the use of lossy balancing resistors to ensure voltage balancing as depicted in Figure 2.2 (a). Secondly, for a single turbine-generator unit with medium dc-link voltages, series-connected switches are required. For example, for a 4160 V system, either 2 series-connected 6500 V switches or 4 series-connected 3300 V switches are needed. Balancing the voltages across series-connected switches is a technical challenge, requiring complicated and expensive voltage balancing controls. This version of the proposed converter is a good candidate for converters with low power and low dc-link voltages. It is important to note that the dc-link voltage here refers to the dc voltage of the power converter of a single turbine-generator system, not the whole wind system.

Version 2: Distributed capacitors are utilized in this version of the proposed converter. Each capacitor's voltage is clamped by the output of the diode rectifier, resulting in inherent capacitor voltage balancing and eliminating the need for balancing resistors. Similar to Version 1, series-connected switches are still required. This version is suitable for converters with low or high-power ratings and low dc-link voltages.

Version 3: This version employs a cascaded DC-DC converter. The constituent modules of the cascaded DC-DC converter are controlled synchronously, sharing a single duty cycle, denoted as d. The series connection at the output ensures an identical output current (I_{dc}) for each module. Consequently, the resultant input current for each module is equal to dI_{dc}. On this basis, the equivalent circuit of the proposed converter is derived and shown in Figure 2.3. Assuming ideal conditions with no parameter tolerance, the secondary winding voltages $v_{s1} = v_{s\mathrm{m}}$ is guaranteed. The input of each module $V_{C\mathrm{m}}$ is clamped by the output of the corresponding diode rectifier which is powered by isolated secondary windings of the phase-shifting transformer, ensuring that V_{C1} equals $V_{C\mathrm{m}}$. However, in practice, parameters such as turn ratios, winding leakage inductances, ON-state voltage of rectifiers, etc., exhibit small tolerances, leading to voltage imbalance. Nevertheless, these imbalances are fixed, stable, small, and negligible due to their small tolerance, and each module operates independent of others thanks to the use of isolated transformers. Therefore, inherent current and capacitor voltage balancing are guaranteed. Furthermore, the modular structure offers higher scalability compared to the other two versions. This version is well-suited for converters with high-power ratings and medium dc-link voltages.

In summary, compared with existing LFT and passive rectifier-based converters, the proposed converter offers superior performance in terms of generator stator current harmonics. This improvement is achieved through the utilization of a phase-shifting transformer, which effectively eliminates specific current harmonics. Additionally, the converter retains the advantages associated with passive rectifiers, such as low cost, high reliability, and scalability, thanks to the employment of a multi-pulse diode rectifier. Moreover, the adoption of a cascaded DC-DC converter not only provides the same level of control flexibility as existing converters but also enhances reliability and scalability due to its modular structure.

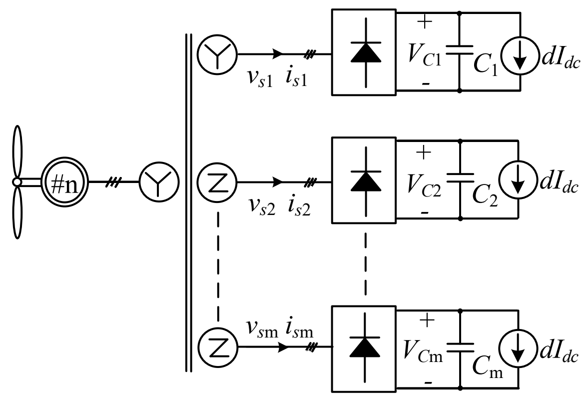

Figure 2.3: Equivalent circuit of the proposed generator-side converter.

2.3 Control scheme

2.3.1 Control of CSC-type series DC-based WECS

The overall control strategy of the CSC-type series DC-based WECS is shown in Figure 2.4. Analogous to VSC-type WECS, where the DC-link voltage is controlled as a constant, the DC-link current of the CSC-type WECS is also controlled as a constant. Following this, the generator-side converters and the grid-side converters are controlled independently. The generator-side converters are controlled to achieve MPPT, while the grid-side converters are responsible for both DC-link current control and reactive power control. Furthermore, on the generator side, power converters at different turbine-generator units are controlled independently. For example, the generator-side converter at turbine-generator #1 is controlled following its own reference, which is independent of that for the converter at turbine-generator #n. On the other hand, the grid-side series-connected CSCs are controlled collectively, where all CSCs are identical and controlled in a synchronous manner, with each CSC carrying one-nth of the total power. Note that a total of n CSC modules are employed on the grid side, matching the number of generator-side converters. Therefore, from the perspective of control system design, the entire system can be simplified to an equivalent power converter, comprising a generator-side converter #n and a grid-side CSC #n. In the following, the simplified converter is employed to illustrate the control system design of the proposed converter.

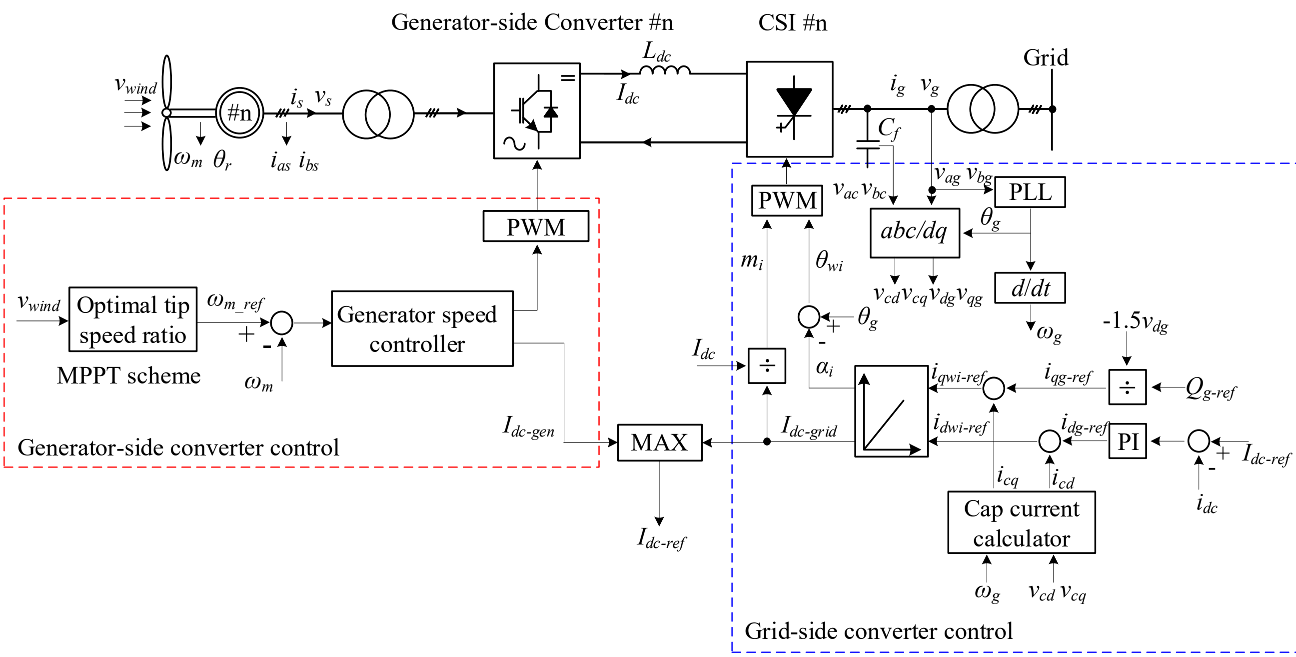

Figure 2.4: Control of CSC-type series DC-based WECS.

2.3.2 Control of proposed generator-side converter

As shown in Figure 2.5, the generator-side converter is controlled to ensure MPPT. On the generator side, the wind speed v_{wind} is measured to determine the generator speed reference $\omega_{m\text{-}ref}$ according to the optimal tip ratio control, one of well-proven MPPT schemes [106]. This reference speed is then sent to the speed controller which generates the required duty cycle d for the modular DC-DC converter. MPPT is then achieved upon applying the duty cycle to the modular dc-dc converter. Since the cascaded DC-DC converter has inherent voltage balancing, no extra balancing control is required.

The grid-side controls include DC-link current control and reactive power control. For CSC-type WECS, either constant DC-link current control or variable DC-link current control can be applied. The former provides higher dynamic performance, while the latter offers higher efficiency. In WECS, while faster dynamic performance is not a top requirement, high efficiency performance is more preferred, thus a variable DC-link current control is employed. To ensure the generator-side MPPT control, a minimum DC-link current is required. To ensure the grid-side reactive power control, a minimum DC-link current is also required. To ensure controls at both sides, the greater one between the two minimum values is selected to be the DC-link current reference used for the DC-link current control. In the following, the respective minimum DC-link currents at both sides and the final DC-link current are selected.

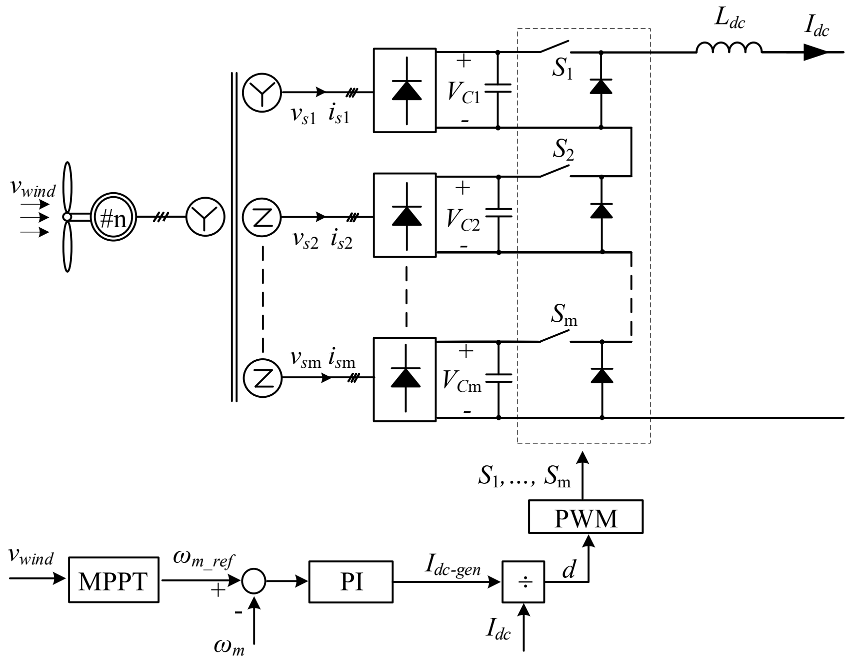

Figure 2.5: Control scheme of the proposed generator-side power converter.

(a) DC-link current required by the generator-side control

To derive the DC-link current required by the generator-side MPPT, the proposed converter is simplified and illustrated in Figure 2.6. The cascaded DC-DC converter is equivalent to a Buck converter, and the multi-pulse diode rectifier is replaced by the conventional 6-pulse diode rectifier, and the voltage source mv_{s1} (m is the number of secondary windings of the phase-shifting transformer) is output of the generator and phase-shifting transformer upon MPPT.

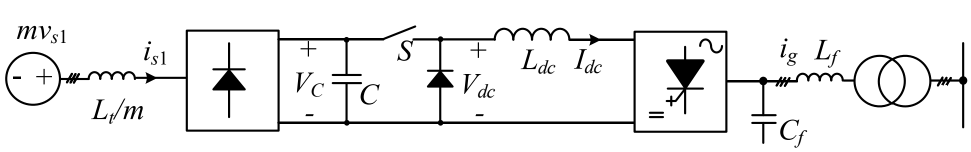

Figure 2.6: Equivalent circuit of the proposed converter.

The output voltage V_C of the diode rectifier is expressed as

$$V_C = \frac{3\sqrt{2}}{\pi} m v_{s1} - \frac{3}{\pi} \frac{\omega_s L_t I_{dc}}{m} \tag{2.1}$$

where m is the number of the secondary windings of the phase-shifting transformer, mv_{s1} is the equivalent input voltage of the diode rectifier, L_t/m is the per-phase inductance of each secondary winding of the phase-shifting transformer, ω_s is the electrical speed of PMSG.

The output voltage V_{dc} of the Buck converter is obtained as

$$V_{dc} = dV_C \tag{2.2}$$

where d is the duty cycle that is received from the MPPT control and applied to the DC-DC converter. Assuming a lossless converter, the following is received.

$$P_g = P_{dc} = V_{dc} I_{dc} \tag{2.3}$$

where P_g is the power captured by the wind turbine-generator unit #n upon MPPT, P_{dc} is the power received at the DC link.

Combining (2.1) – (2.3) and setting $d = 1$, the minimum dc-link current ($I_{dc\text{-}gen\text{-}\min}$) determined by the generator-side converter upon MPPT is expressed as

$$I_{dc-gen-\min} = \frac{3\sqrt{2} m V_{s1} - \sqrt{18 m^2 V_{s1}{}^2 - 12\pi \omega_s L_t P_g}}{6\omega_s L_t} \tag{2.4}$$

(b) DC-link current required by the grid-side control

The grid-side controls consist of DC-link current control and reactive power control. DC-link current control adjusts the captured wind power, while reactive power control regulates reactive power in accordance with grid codes. As depicted in Figure 2.5, two independent control loops are implemented based on voltage-oriented control. These control loops generate the modulation index and phase angle used for modulation implementation. Various modulation schemes can be employed for CSC [58-59] [62] [67-68]. In this study, the conventional space vector modulation (SVM) is utilized.

As shown in Figure 2.5, the reactive power (Q_s) and real power (P_s) are controlled independently in the *dq* frame:

$$\begin{aligned} P_s &= 1.5 v_{dg} i_{dg} \\ Q_s &= -1.5 v_{dg} i_{qg} \end{aligned} \tag{2.5}$$

where v_{dg} is the *d*-axis component of the grid voltage, i_{dg} and i_{qg} are *d*- and *q*-axis components of grid current.

The reference PWM currents in *dq* frame ($i_{dwi-ref}$ and $i_{qwi-ref}$) after compensating the capacitor currents are expressed as follows.

$$\begin{cases} i_{dwi-ref} = i_{dg-ref} + i_{cd} = i_{dg-ref} - \omega_g C_f v_{cq} \\ i_{qwi-ref} = i_{qg-ref} + i_{cq} = i_{qg-ref} + \omega_g C_f v_{cd} \end{cases} \tag{2.6}$$

where i_{dg-ref} and i_{qg-ref} are the references of the *d*- and *q*-axis components of the grid current, and they are the outputs of the reactive power control and dc current control as shown in Figure 2.4. i_{cd}, i_{cq}, v_{cd} and v_{cq} are *d*- and *q*-axis components of the capacitor current and voltage, respectively, C_f is the filter capacitor of the grid-side CSC, and ω_g is the angular speed of the grid.

The capacitor voltage and grid voltage are related as:

$$\begin{cases} v_{cd} = v_{sd} - \omega_g L_f i_{qg} \\ v_{cq} = \omega_g L_f i_{dg} \end{cases} \tag{2.7}$$

where L_f is the filter inductor of the grid-side CSC.

Assuming a lossless system and a unity power factor at the grid side, the minimum DC-link current required by the grid-side control occurs at $m_i = 1$. Combining (2.5) - (2.7) and substituting $m_i = 1$ into the equation yields the minimum DC-link current determined by the grid-side control.

$$i_{dc-grid-\min} = \sqrt{\left\{(1-\omega_g{}^2 L_f C_f)(\frac{2}{3}\frac{P_g}{v_{dg}})\right\}^2 + (\omega_g C_f v_{dg})^2} \qquad (2.8)$$

In summary, equation (2.4) illustrates the minimum DC-link current to ensure the generator-side MPPT, while equation (2.8) represents the minimum DC-link current to ensure the grid-side reactive power control. To simultaneously ensure control at both sides, the greater of the two values is selected as the final DC-link current reference for the control system, expressed as:

$$I_{dc-ref} = \max\{I_{dc-grid-\min}, I_{dc-gen-\min}\} \qquad (2.9)$$

The dc current reference ($I_{dc-grid}$) and delay angle (α_i) of the grid-side CSC can then be calculated based on the following Cartesian-to-polar transformation:

$$\begin{aligned} I_{dc-grid} &= \sqrt{(i_{dwi-ref})^2 + (i_{qwi-ref})^2} \\ \alpha_i &= \tan^{-1}(i_{qwi-ref} / i_{dwi-ref}) \end{aligned} \qquad (2.10)$$

Then the modulation index for the CSC and the angle of the PWM current (θ_{wi}) is calculated based on (2.11).

$$\begin{aligned} m_i &= I_{dc-grid} / I_{dc} \\ \theta_{wi} &= \theta_g - \alpha_i \end{aligned} \qquad (2.11)$$

where θ_g is the grid voltage angle. After applying m_i and θ_{wi} to the grid-side CSC, reactive power and dc current controls are achieved. Note that different modulation schemes can be used here, please refer to [8] for details. As discussed earlier, the reference dc current (I_{dc-ref}) is the bigger one between $I_{dc-grid-\min}$ and $I_{dc-gen-\min}$. Upon applying I_{dc-ref}, the controls at both sides can be ensured. Please refer to [51-53] for details of dc current control.

2.4 Simulation and experimental results

The proposed generator-side converter has been verified through both MATLAB/Simulink simulation and laboratory-scaled experiments. It is noteworthy that all three versions share the same control scheme, as well as the same generator-side and grid-side performance. Therefore, only Version 3 is studied. The parameters utilized are listed in Table 2.1, and Figure 2.7 illustrates the converter circuit used for simulations.

Table 2.1: Simulation and experiment parameters

Parameters	Simulation	Experiment
System Rating		
Nominal Power	1 MW (1.0 pu)	1200 W (1.0 pu)
Grid/Load Voltage	4160 V (1.0 pu)	110 V (1.0 pu)
Frequency	60 Hz (1.0 pu)	60 Hz (1.0 pu)
PMSG		
Nominal Voltage	4000 V	Variac
Synchronous Inductance	0.4 pu	
Stator Resistance	0.01 pu	
Generators-Side Converter		
Phase-Shifting Transformer	$m = 5$	$m = 2$
Leakage Inductance	0.08 pu	NA
Switching Frequency	1000 Hz	1000 Hz
Grid/Load-Side CSC		
DC-link Inductor	45 mH (1.0 pu)	30 mH (1.0 pu)
Grid/Load-Side Inductor	5 mH (0.11 pu)	5 mH (0.18 pu)
Grid/Load-Side Capacitor	77 uF (0.5 pu)	100 uF (0.38pu)
Grid/Load-Side Resistor	NA	10 Ω (1.0 pu)
Switching Frequency	540 Hz	540 Hz

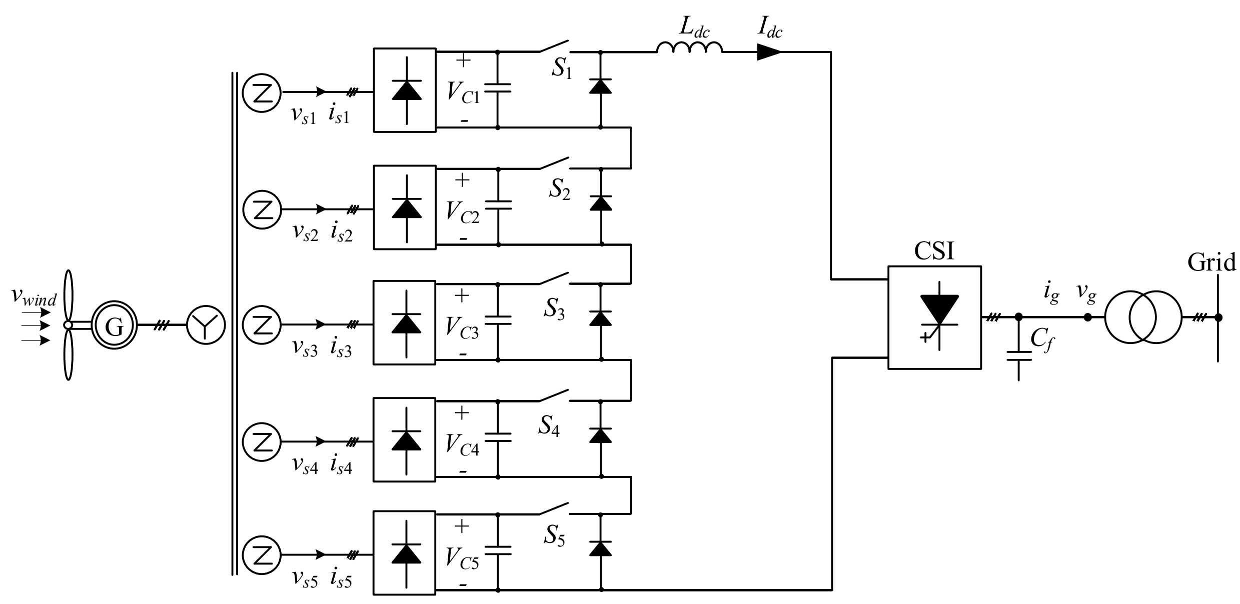

Figure 2.7: Converter circuit used for simulations.

2.4.1 Simulated results

Figure 2.8 shows the simulated waveforms of the proposed power converter under both steady and dynamic states. Before t = 1.5s, the converter is operating under rated conditions. At t = 1.5s, the wind speed is purposely reduced from 1 pu (12 m/s) to 0.8 pu (9.6 m/s); the generator speed reference $\omega_{m\text{-}ref}$ is reduced to 0.8 pu; and the dc-link current reference $I_{dc\text{-}ref}$ is adjusted accordingly to minimize power loss. Both generator speed control and dc-link current control effectively track their respective references well in this transition. Once this transition is complete, the converter operates at a new operational point, characterized by a reduction in generator voltage v_p to 0.8 pu and a decrease in captured real power to approximately 0.51 pu. At t = 2.5s, the wind speed is intentionally increased from 0.8 pu back to 1 pu. The converter then smoothly transitions back to rated operation with both generator-side speed and grid-side dc-link current and unity power factor being well controlled.

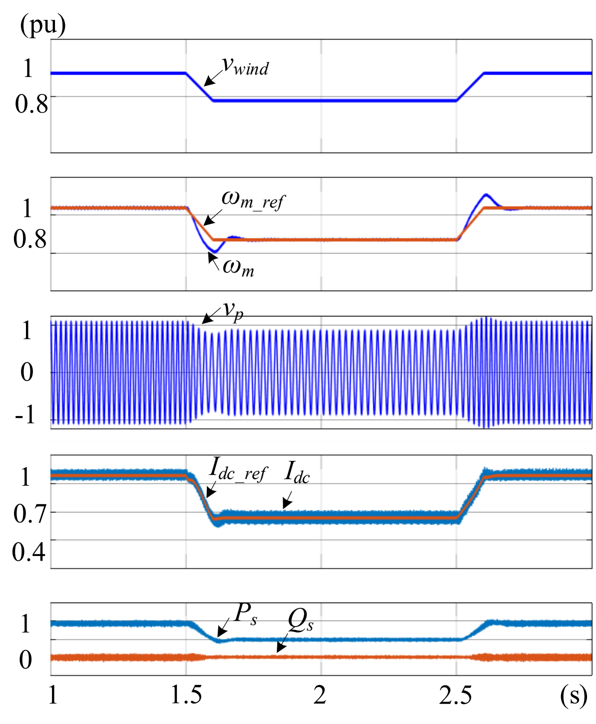

Figure 2.8: Simulated waveforms under steady and dynamic states.

Figure 2.9 shows the simulated current harmonics performance of the proposed converter under rated conditions. The rectifier currents, i_{s1}, i_{s2}…, i_{s5}, exhibit significant distortion primarily due to the presence of 5th and 7th harmonics, accounting for approximately 20% and 12%, respectively.

In contrast, the primary current, i_p, demonstrates superior harmonic performance, attributed to the utilization of a phase-shifting transformer. Notably, the 5th and 7th harmonics are effectively eliminated, reducing the THD of i_p to 1.5% under rated conditions.

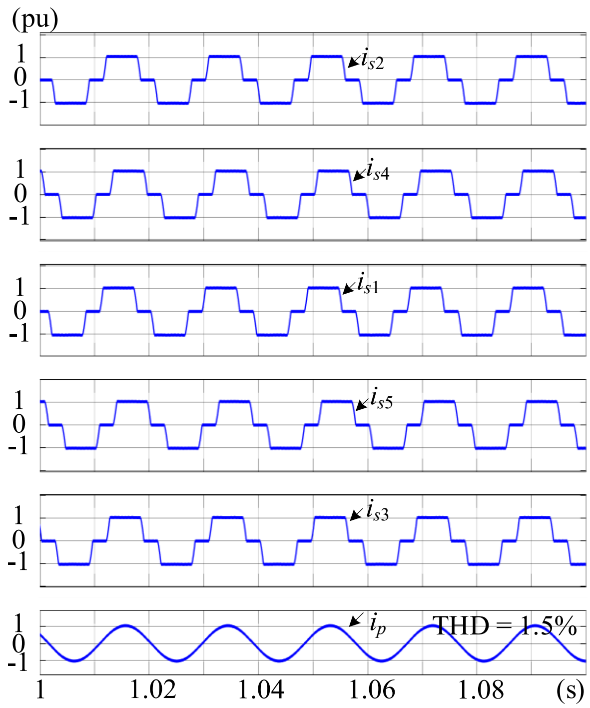

Figure 2.9: Simulated harmonics performance under rated conditions.

Figure 2.10 displays the simulated waveforms of the capacitor voltages of the proposed converter under both steady and dynamic states. The proposed converter features inherent capacitor voltage balancing, eliminating the need for additional balancing control mechanisms. Prior to t = 1.5s, the converter is operating under rated conditions, at t = 1.5s, the wind speed is reduced from 1 pu to 0.8 pu, and at t = 2.5s, the wind speed is increased from 0.8 pu to 1 pu. Consequently, the generator terminal voltage, DC-link current, and captured wind power undergo corresponding changes. Throughout both transitions and steady states, the capacitor voltages (V_{C1}…, V_{C5}) remain well balanced without requiring balancing resistors or additional control mechanisms. This simulated result aligns well with previous analyses.

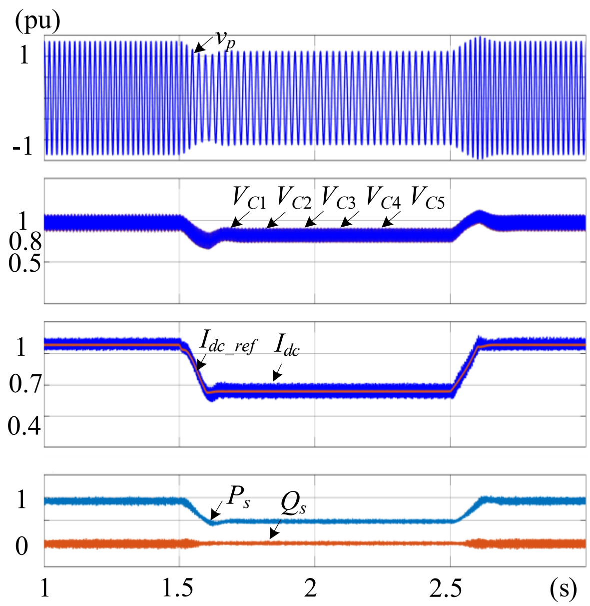

Figure 2.10: Simulated capacitor voltage balancing under steady and dynamic states.

2.4.2 Experimental investigation

Lab-scale experiments have been conducted to verify the performance of the proposed converter. Since grid-side controls, including DC-link current control and reactive power control, have been well studied in previous research [51-53], they are not repeated here. As shown in Figure 2.11, a variac is used to simulate the turbine-generator set, a 12-pulse diode rectifier connected to two Buck converters, and a conventional CSC with an RL load are employed.

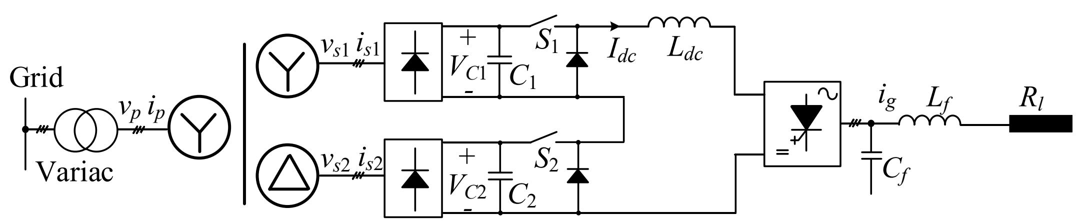

Figure 2.11: Converter circuit used for lab-scale experiments.

Figure 2.12 shows the experimental waveforms of the proposed converter under both steady and dynamic states. Under rated condition, the input line-to-neutral voltage v_p is set to 35 V, the dc-link current I_{dc} is around 9 A, the load current i_g is around 6.3 A, and the rated power is approximately 1200 W. Additionally, as depicted in Figure 2.12, the input voltage v_p is increased from around 20 V to 35 V by manually adjusting the variac transformer to emulate the change in wind speed. Consequently, the dc-link current and the output current are changed accordingly.

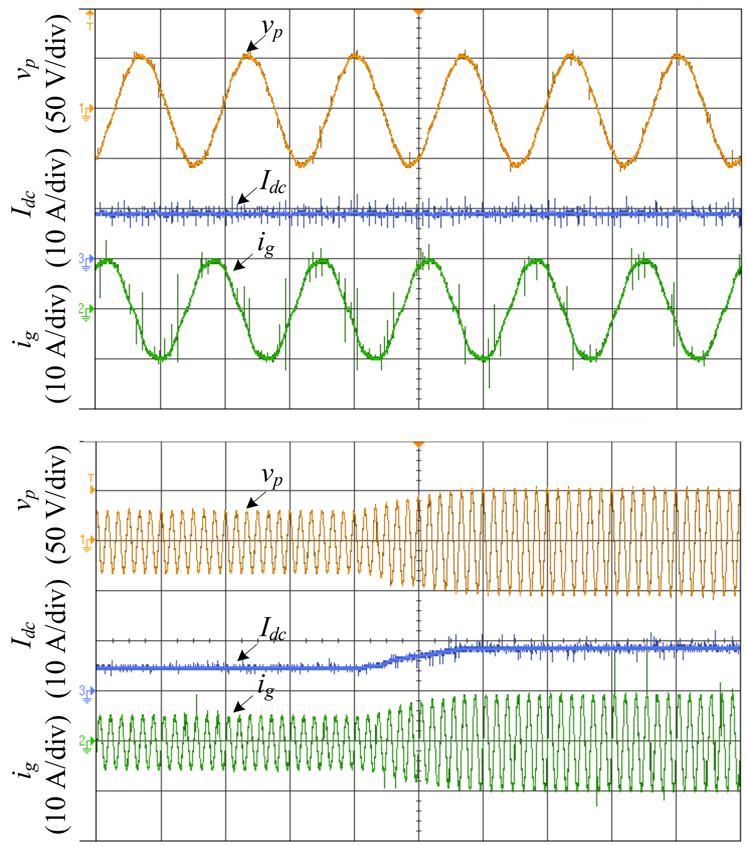

Figure 2.12: Experimental waveforms of the proposed converter under steady and dynamic states.

Figure 2.13 illustrates the experimental harmonic performance of the proposed converter under rated conditions. The measured secondary currents, i_{s1} and i_{s2}, exhibit a quasi-trapezoidal waveform with a phase shift of 30° and contain significant harmonics, with the 5th and 7th harmonics being dominant. Theoretically, the phase-shifting transformer should eliminate the 5th and 7th harmonics, not appearing in the primary current i_p. However, in the experimental setup, the phase-shifting transformer is subject to tolerances in parameters such as leakage inductance, resistance, and turn ratios. Consequently, the 5th and 7th harmonics remain present, as shown in Figure 2.13, with magnitudes of 3% for the 5th harmonic and 4% for the 7th harmonic.

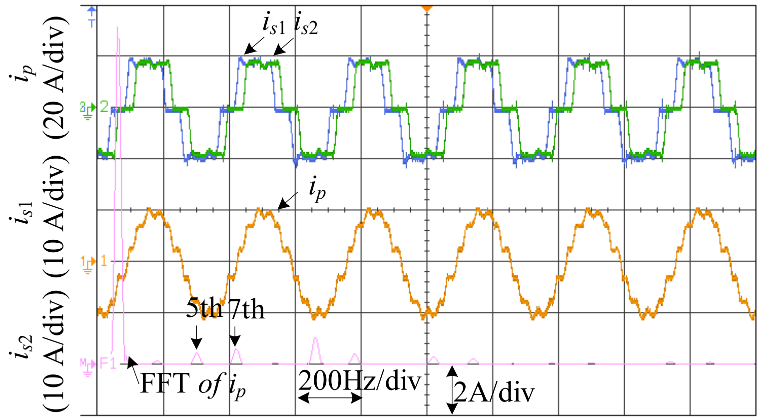

Figure 2.13: Experimental harmonic performance of the proposed converter under rated conditions.

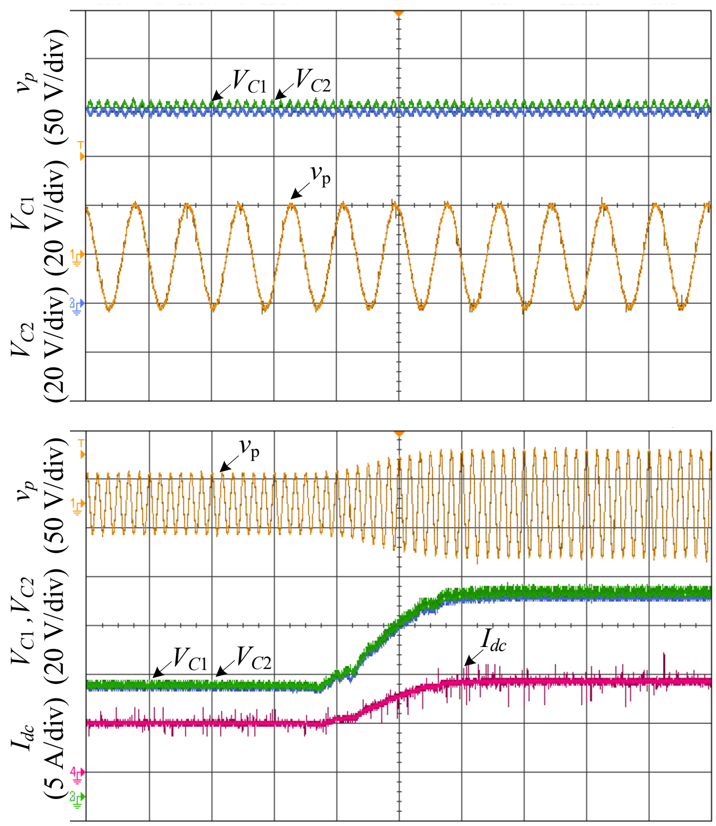

Figure 2.14: Experimental inherent capacitor voltage balancing of the proposed converter under both steady and dynamic states.

Figure 2.14 displays the capacitor voltages of the proposed converter under both steady and dynamic states. Under rated conditions, the capacitor voltages are V_{C1} = 80 V and V_{C2} = 78 V. This slight mismatch is due to the parameter tolerances in the phase-shifting transformer, such as the turn ratio. Nevertheless, as shown in Figure 2.14, this mismatch is fixed, stable, small, and negligible under both steady and dynamic states. Aside from this discrepancy, the capacitor voltages exhibit good balance. For example, when the input voltage v_p is increased from 20 V to 35 V, V_{C1} and V_{C2} are increased from 45 V to 80 V, respectively.

In summary, both simulation and experiments have validated that: 1) the proposed converter demonstrates superior current harmonic performance due to the use of the phase-shifting transformer, and 2) the cascaded DC-DC converter inherently maintains voltage balance under both steady and dynamic states without the need for the balancing control.

2.4 Conclusions

The LFT and passive rectifier-based converters are well-studied power converters utilized on the generator side of WECS. The LFT, a mature technology, serves to isolate the generator from HVDC levels, allowing the use of generators with regular insulation levels. On the other hand, passive rectifier-based converters offer WECS with low cost, high reliability, simplicity, and scalability. However, the utilization of passive rectifiers results in highly distorted generator stator currents, leading to increased power losses and reduced lifespan of generators.

To address this issue while retaining the advantages of both the LFT and passive rectifier-based converters, a phase-shifting transformer-based converter is proposed in this chapter. This converter comprises a phase-shifting transformer, a multi-pulse diode rectifier, and a cascaded DC-DC converter. The phase-shifting transformer has the capability to eliminate specific current harmonics, thereby significantly improving the performance of generator stator current harmonics and reducing power losses, ultimately prolonging the service life of generators. Furthermore, like the LFT, the phase-shifting transformer is also a mature technology.

The inclusion of a multi-pulse diode rectifier in the proposed converter ensures the retention of the advantages associated with passive rectifiers. Additionally, the cascaded DC-DC converter not only facilitates generator-side MPPT control but also features inherent capacitor voltage balancing. In summary, the proposed converter effectively addresses the shortcomings of existing LFT and passive rectifier-based converters while preserving all of their advantages. Three versions of the proposed generator-side converter have been developed to accommodate applications with different power/voltage ratings. The operational principles of the proposed converter are thoroughly discussed, and control schemes are developed. Furthermore, both simulations and experiments have been conducted to validate the performance of the proposed converter.

Chapter 3

Generator-Side Passive Rectifier-Based Converter with Multi-Phase Generator and Modular Medium-Frequency Transformers

In CSC-type series DC-based WECS, the use of LFT and passive rectifier-based converters on the generator side provides several advantages. The LFT offers a practical solution for addressing the generator insulation issue, while the passive rectifier features low cost, high reliability, and scalability. However, the LFT is bulky, posing a challenge to WECS due to limited space in the nacelle of the wind turbine. Furthermore, using passive rectifier-based converters results in highly distorted generator stator currents, leading to significant torque ripples and a reduced lifespan of the generator. To overcome these issues, a new generator-side power converter is proposed. It exhibits superior harmonic performance of the generator stator current while retaining all the benefits of the passive rectifier. Additionally, it offers significant reductions in the size and weight of magnetic components. This chapter begins with an introduction to the proposed power converter, including its operation principles and features. Subsequently, the control scheme is presented. Finally, the performance of the proposed converter is validated through both simulations and laboratory-scale experiments.

3.1 Existing LFT and passive rectifier-based based converters

Figure 3.1 illustrates existing LFT and passive rectifier-based converters used on the generator side of CSC-type series DC-based WECS [88][89]. The use of the LFT [46-48] allows for the utilization of generators with standard insulation levels but presents challenges due to its large size and weight, especially considering the limited space within the turbine nacelle. Passive rectifiers offer benefits such as low cost, high reliability, and scalability to WECS. However, they produce highly distorted generator stator current harmonics, resulting in increased power loss and reduced lifespan of generators.

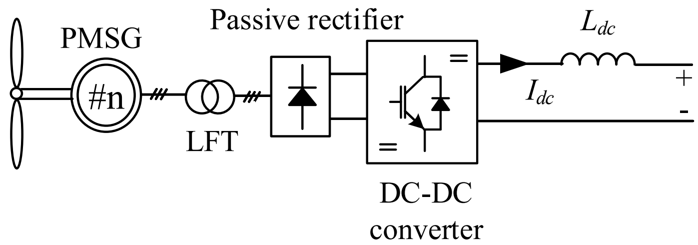

Figure 3.1: Existing LFT and passive rectifier-based converters.

To mitigate the challenges associated with passive rectifiers while preserving their advantages, a phase-shifting transformer-based converter was proposed, as illustrated in Figure 3.2. This solution retains the benefits of passive rectifiers by incorporating a multi-pulse diode rectifier. Furthermore, it utilizes an LFT, albeit not the conventional isolated transformer but a phase-shifting transformer. In addition to ensuring the use of generators with standard insulation levels, it eliminates specific current harmonics generated by passive rectifiers, thereby improving the performance of generator stator current harmonics and ultimately reducing power loss while increasing the service life of generator systems. The same as the conventional LFT depicted in Figure 3.1, the phase-shifting transformer is also an LFT, characterized by its large size and weight.

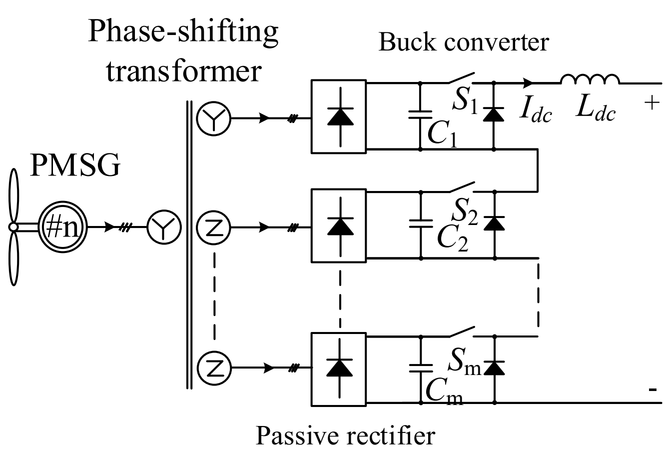

Figure 3.2: Phase-shifting transformer-based converter.

In summary, the use of LFT, including both conventional isolated transformers and phase-shifting transformers, enables the utilization of generators with standard insulation requirements. However, their bulky nature poses challenges for WECS, particularly in nacelles where space is limited. Passive rectifiers offer advantages such as low cost, simplicity, high reliability, and scalability. Nevertheless, they generate highly distorted currents, resulting in reduced efficiency and shortened lifespan of generator systems, unless addressed by solutions such as the utilization of bulky phase-shifting transformers.

3.2 Multi-phase generator-based converter with modular medium-frequency transformers

To address the respective challenges associated with the bulky LFT and passive rectifiers while preserving their respective advantages and functions, a new generator-side converter is proposed. It is a multi-phase generator-based converter comprising a multi-phase generator, diode rectifiers, and a modular medium-frequency transformer (MFT)-based DC-DC converter.

The use of diode rectifiers allows the proposed converter to retain advantages associated with diode rectifiers, such as low cost and high reliability, while the utilization of a multi-phase generator enables the elimination of specific current harmonics generated by diode rectifiers. For example, a 6-phase generator with a phase shift of 30 degrees between its two sets of stator windings is able to eliminate the dominant 5^{th} and 7^{th} harmonics generated by a 6-pulse diode rectifier.

Like the LFT, the MFT isolates generators from HVDC, thus allowing the use of generators with regular insulation requirements [84]. On the other hand, the MFT withstands HVDC-level insulation. However, MFTs with such high-voltage insulation requirements, as well as high-power ratings, are not mature. To address this problem, modular MFTs [41] [43][53][54] are employed, with each MFT carrying one part of the rated power, thus reducing the manufacturing burden. Compared with the LFT, the MFT offers a smaller size and weight.

To enable the utilization of low-cost, low-voltage, low-current switches for generator systems with different voltage ratings, two versions of the proposed converter are developed. Figure 3.3 shows the low-voltage (LV) version of the proposed converter for generators with LV ratings, while Figure 3.4 shows the medium-voltage (MV) version for generators with MV ratings. In the LV converter as shown in Figure 3.3, the modules of the DC-DC converter are connected in parallel at the input and in series at the output. The parallel connection at the input allows the use of low-cost, low-voltage, low-current devices for LV generator systems. Similarly, the modules of the DC-DC converter of the MV version, as shown in Figure 3.4, are connected in series at both input and output, also allowing the use of low-cost, low-voltage, low-current devices for MV generator systems.

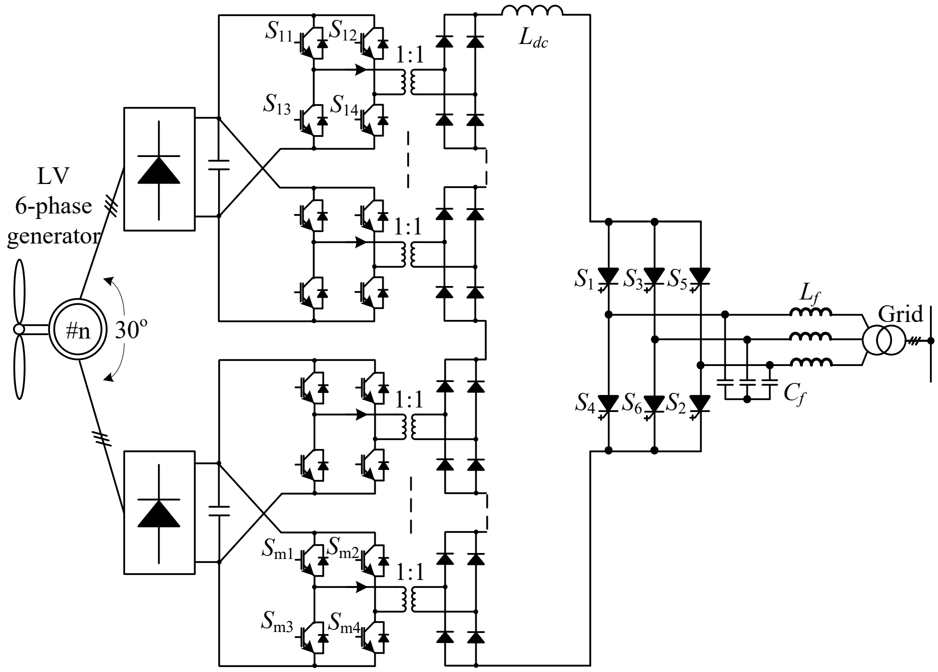

Figure 3.3: Proposed multi-phase generator-based converter: LV version.

The number (m) of modules of the DC-DC converter is selected to reduce the DC-link current of the conversion system, thereby reducing power loss. The DC-link current of the conversion system is the greater one of two reference currents: one is generator-side reference current, and the other the grid-side reference current. In the following, the derivation of reference currents and the selection of m are presented.

Figure 3.5 shows the simplified equivalent circuit of proposed converters including the two versions. The identical H-bridge modules of the DC-DC converter and are simplified to series-connected buck converters.

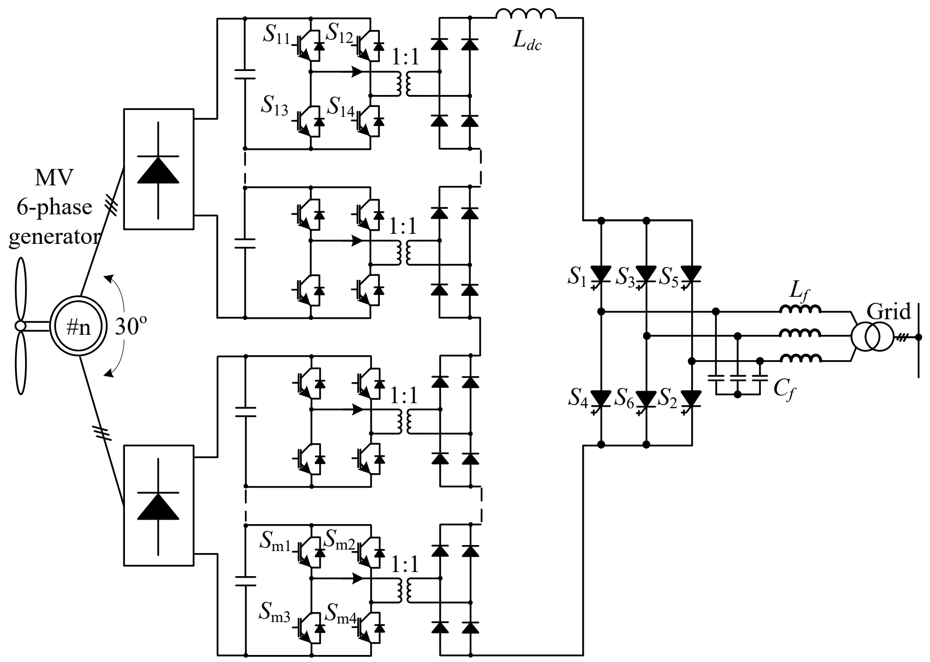

Figure 3.4: Proposed multi-phase generator-based converter: MV version.

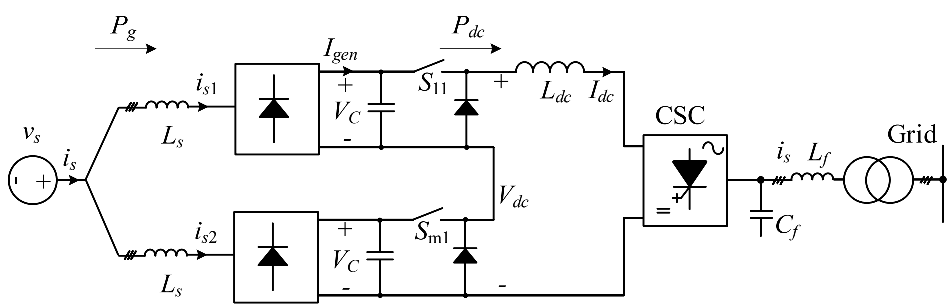

Figure 3.5: Simplified equivalent circuit of proposed converters.

The output voltage V_C of the conventional 6-pulse diode rectifier is expressed as

$$V_C = \frac{3\sqrt{2}}{\pi} v_s - \frac{3}{\pi} \omega_s L_s I_{gen} \tag{3.1}$$

where v_s is the generator terminal voltage, L_s is generator synchronous inductance, and ω_s is the generator angular speed, and I_{gen} is the average output current of the diode rectifier.

The input and output of series-connected buck converters are related as

$$
\begin{aligned}
V_{dc} &= mdV_C \\
I_{dc} &= I_{gen} / d
\end{aligned}
\tag{3.2}
$$

where m is the number of H-bridge converter modules of the DC-DC converter, and d is the duty cycle. Applying the law of conservation of energy results in the following:

$$P_g = P_{dc} = V_{dc} I_{dc} \tag{3.3}$$

where P_g is the captured wind power upon MPPT, and P_{dc} is the power received at the dc side.

I_{gen} is the resultant current achieved upon reaching MPPT. In other words, to achieve MPPT, a minimum current of I_{gen} is required. On this basis, as shown in (3.2), the minimum DC-link current I_{dc} needed to achieve MPPT is $I_{dc} = I_{gen}$, occurring at $d = 1$. Finally, combining (3.1) - (3.3) and setting $d = 1$ results in the generator-side reference dc-link current $I_{dc\text{-}gen}$.

$$I_{dc-gen} = \frac{3\sqrt{2}v_s - \sqrt{18 {v_s}^2 - \dfrac{12\pi\omega_s L_s P_g}{m}}}{6\omega_s L_s} \tag{3.4}$$

The grid-side reference current $I_{dc\text{-}grid}$ has been derived in the previous chapter and will not be repeated in this chapter.

$$I_{dc-grid} = \sqrt{\left\{(1-{\omega_g}^2 L_f C_f)(\frac{2}{3}\frac{P_g}{v_{sd}})\right\}^2 + (\omega_g C_f v_{gd})^2} \tag{3.5}$$

where ω_g is the grid angular frequency, L_f and C_f are filter inductor and capacitor of the grid-side CSC, and v_{gd} is the d-axis component of the grid voltage.

To ensure controls at both generator and grid sides, the greater one of the above two current references is selected as the reference DC-link current ($I_{dc\text{-}ref}$) of the proposed conversion system.

$$I_{dc-ref} = \max\{I_{dc-grid}, I_{dc-gen}\} = \begin{cases} I_{dc-grid} \,@\, I_{dc-grid} \geq I_{dc-gen} \\ I_{dc-gen} \,@\, I_{dc-grid} \leq I_{dc-gen} \end{cases} \tag{3.6}$$

As indicated in equation (3.6), $I_{dc\text{-}grid}$ remains fixed under rated conditions, while from equation (3.4), $I_{dc\text{-}gen}$ shows an inverse proportionality to the number (m) of H-bridge converter modules in the DC-DC converter. Consequently, when $I_{dc\text{-}grid} > I_{dc\text{-}gen}$, it generates results in a smaller final reference DC-link current compared to the scenario where $I_{dc\text{-}grid} < I_{dc\text{-}gen}$. Thus, the number 'm' is selected based on the condition $I_{dc\text{-}grid} > I_{dc\text{-}gen}$.

For instance, in the LV version, considering a rated generator terminal voltage of 690 V, a rated output line-to-line voltage of 4160 V for the CSC, a rated power of 1 MW, and the utilization of 1700 V IGBTs, a value of $m = 6$ is chosen. For the MV version, where the generator rated voltage is 4000 V, the CSC voltage remains at 4160 V, and the power is 1 MW, $m = 10$ is selected when using 1700 V IGBTs, while $m = 6$ is chosen when employing 3300 V IGBTs.

3.3 Control scheme

The overall control strategy of the CSC-type series DC-based WECS has been discussed in the previous chapter and will not be repeated in this chapter. The same as Chapter 2, the back-to-back power converter, comprising a generator-side converter #n and a grid-side CSC #n, is taken as an example to illustrate the control system design of the proposed converter.

3.3.1 Shared control of proposed LV and MV converters

The proposed LV and MV converters share the same generator-side MPPT and grid-side DC-link current and reactive power controls.

As shown in Figure 3.6, on the generator side, the wind speed v_{wind} is measured to determine the generator speed reference ω_{m_ref} according to the optimal tip ratio, one of well-proven MPPT schemes [106]. This reference speed is then sent to the speed controller which generates the required duty cycle d for the modular MFT-based DC-DC converter. MPPT is then achieved upon applying the duty cycle to the modular dc-dc converter.

On the grid side, DC-link current control and reactive power control are implemented. The two controls are done independently in the dq frame. The PI controller of the DC current control outputs the d-axis grid current reference ($i_{dg\text{-}ref}$). The q-axis grid current reference ($i_{qg\text{-}ref}$) is calculated according to the reactive power reference ($Q_{s\text{-}ref}$) and the d-axis grid voltage (v_{dg}) as shown below.

$$P_s = \frac{3}{2} v_{dg} i_{dg}$$
$$Q_s = -\frac{3}{2} v_{dg} i_{qg} \tag{3.7}$$

where i_{dg} and i_{qg} are d-axis and q-axis grid currents respectively.

The calculation of the dq-axis PWM currents ($i_{dwi\text{-}ref}$ and $i_{qwi\text{-}ref}$) requires the compensation of the filter capacitor currents.

$$\begin{aligned} i_{dwi-ref} &= i_{dg-ref} - i_{cd} = i_{dg-ref} + \omega_g C_f v_{cq} \\ i_{qwi-ref} &= i_{qg-ref} - i_{cq} = i_{qg-ref} - \omega_g C_f v_{cd} \end{aligned} \tag{3.8}$$

where i_{cd} and i_{cq} are the dq-axis capacitor currents, and the v_{cd} and v_{cq} are the dq-axis capacitor voltages.

$$\begin{aligned} v_{cd} &= V_{dg} - \omega_s L_f i_{qg} \\ v_{cq} &= \omega_g L_f i_{dg} \end{aligned} \tag{3.9}$$

The dc current reference ($i_{dc\text{-}grid}$) and delay angle (α_i) of the grid-side CSC are calculated based on the following.

$$\begin{aligned} i_{dc-grid} &= \sqrt{(i_{dwi-ref})^2 + (i_{qwi-ref})^2} \\ \alpha_i &= \tan^{-1}(i_{qwi-ref} / i_{dwi-ref}) \end{aligned} \tag{3.10}$$

The modulation index (m_i) for the CSC is then obtained by $i_{dc\text{-}grid}/i_{dc}$. And the angle of the PWM current (θ_{wi}) is calculated based on $\theta_{wi} = \theta_g$ - α_i in which θ_s is the grid voltage angle. After applying m_i and θ_{wi} to the grid-side CSC, reactive power and dc current controls are achieved. Note that different modulation schemes can be used here [29]. As discussed earlier, the reference dc current ($I_{dc\text{-}ref}$) is the bigger one between $I_{dc\text{-}grid}$ and $I_{dc\text{-}gen}$. Upon applying $I_{dc\text{-}ref}$, the controls at both sides can be ensured.

3.3.2 Balancing control of proposed LV and MV converters

Both LV and MV converters utilize the modular MFT-based DC-DC converter, employing multiple H-bridge converters. Figure 3.7 illustrates the equivalent circuits of these two DC-DC converters. Here, V_C represents the input voltage of the MFT-based DC-DC converter, clamped by the output voltage of the diode rectifier. The DC inductor and grid-side CSC are replaced with a current source I_{dc}. In both converters, the modules share the same I_{dc}.

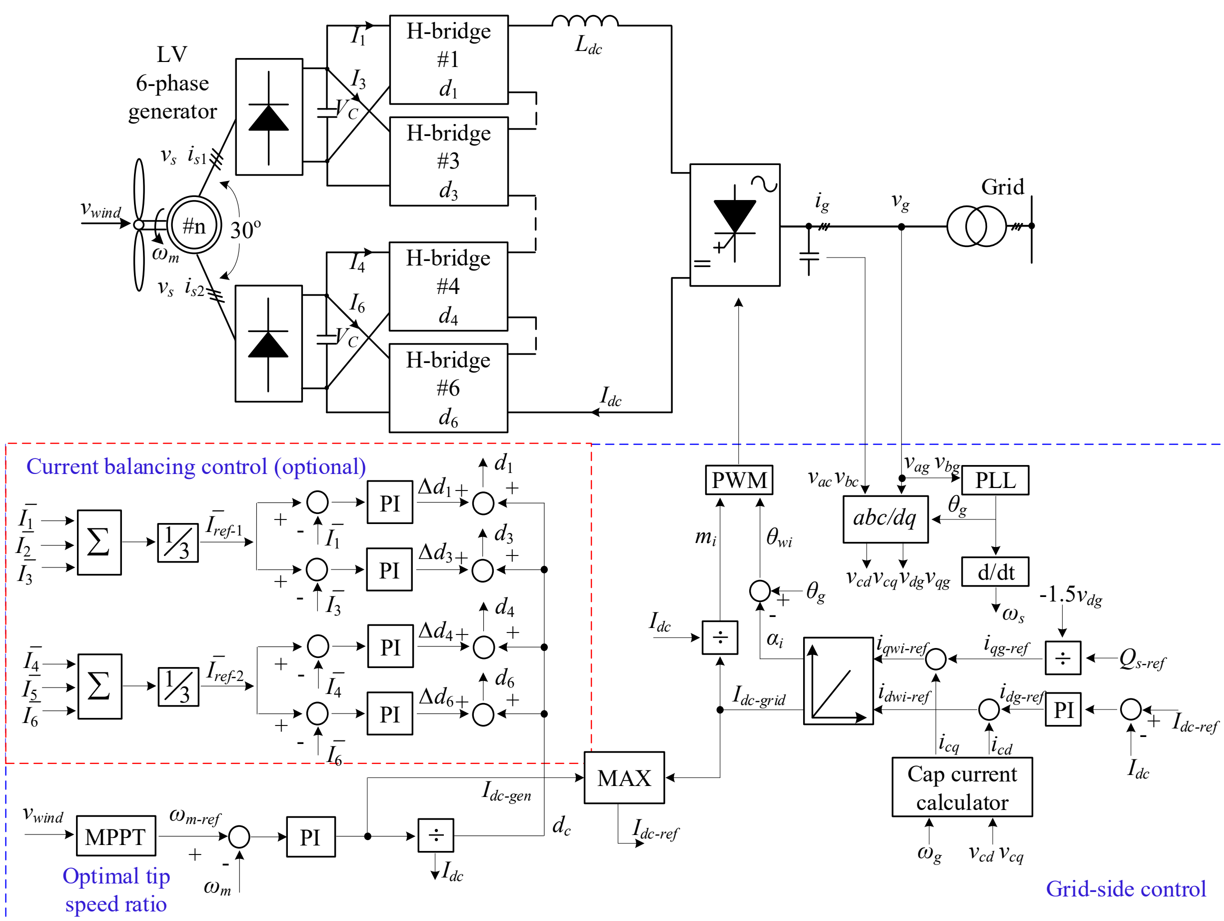

(a) Control for the proposed converter: LV version

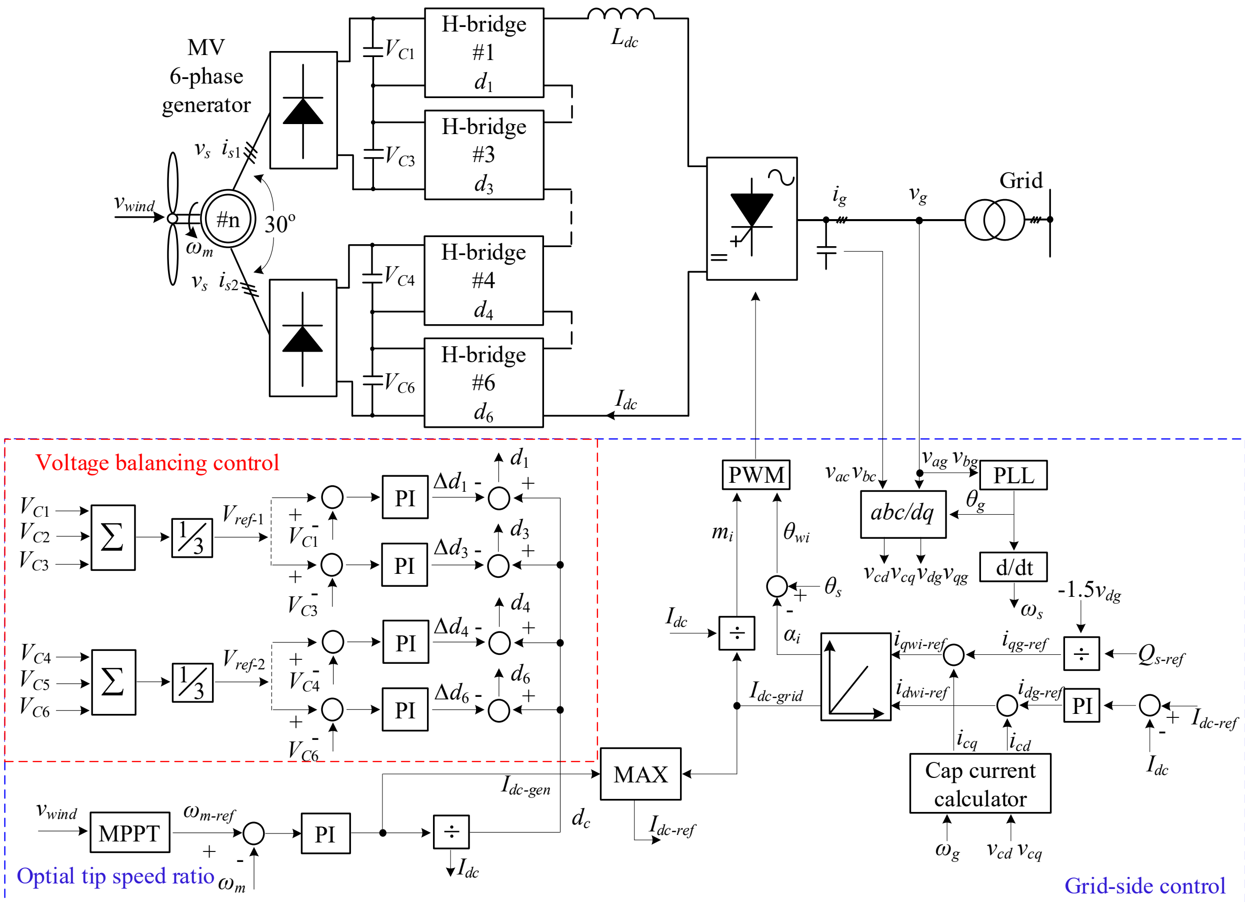

(b) Control for the proposed converter: MV version

Figure 3.6: Control scheme of the proposed converters.

However, in practice, parameter tolerance exists, leading to imbalance issues. This tolerance results in voltage imbalance for the MV version and current imbalance for the LV version. For instance, the turn ratio of different MFTs cannot be guaranteed to be identical due to manufacturing tolerance. Consequently, in the MV converter, the module with a higher turn ratio suffers from a higher capacitor voltage, while in the LV converter, it experiences a lower input current. The MV version's structure, with series connection at both input and output, is unstable, necessitating voltage balancing control. Conversely, the LV version's structure, with parallel connection at the input and series connection at the output, is stable, resulting in a fixed and stable imbalance. With modern manufacturing techniques, mismatches can be limited, and power imbalance becomes insignificant. Consequently, current balancing control becomes optional for the LV version.

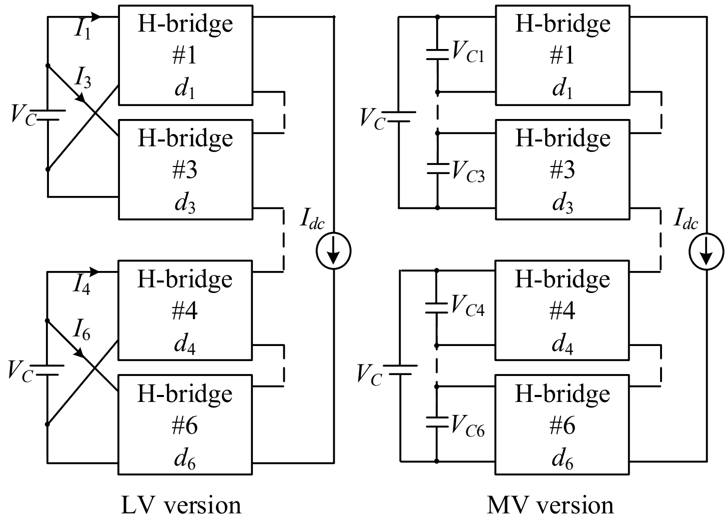

Figure 3.7: Equivalent circuits of proposed converters.

Optional current balancing control of the LV converter: Shown in Figure 3.6, the average current is compared with the reference current to generate an error signal, which then passes through the PI controller, resulting in an additional duty cycle, Δd_1 for #1, and Δd_6 for #6. This additional duty cycle is used to correct the current imbalance. The reference current is obtained by averaging the currents of all modules. Finally, the duty cycles (d_1, d_2 …, and d_6) are resulted by adding the common duty cycle d_c and the additional one Δd_1, Δd_2 …, and Δd_6. The former ensures MPPT, while the latter current balancing.

Mandatory voltage balancing control of the MV version: Shown in Figure 3.6, the measured capacitor voltages V_{C1} and V_{C6} are compared with their reference values. The resulting errors go through the respective PI controllers to generate extra duty cycles for voltage balancing. The duty cycles (d_1, d_2 …, and d_6) ultimately consist of the common duty cycle d_c and the extra ones (Δd_1, Δd_2 …, and Δd_6) outputted by the respective voltage balancing controllers. The former ensures MPPT, while the latter voltage balancing.

3.4 Simulation and experimental results

MATLAB simulations were conducted to investigate the performance of the proposed two converters. First, the wind turbine model is provided by MATLAB, and the optimal tip ratio is utilized for the MPPT control. Second, to effectively study the harmonic performance, a 3-phase generator connected to a phase-shifting transformer is used to simulate the 6-phase generator. Third, six modular H-bridge converters are employed for both simulations, with a maximum tolerance of 10% introduced to six MFTs to verify the performance of the proposed balancing control. The key parameters are listed in Table 3.1. The converter circuits used for simulations are illustrated in Figure 3.8.

Table 3.1: Simulation and experiment parameters

Parameters	Simulation		Experiment	
	MV	LV	MV	LV
System Rating				
Nominal power	1 MW	1 MW	600 W	600 W
Grid voltage	4160 V	4160 V	110 V	110 V
PMSG				
Nominal voltage	4000 V	690 V	Variac + phase-shifting transformer	
Number of poles	16	26		
Rated speed	400 rpm	22.5 rpm		
Generators-side converter				
Number of modules	6		4	
Transformer turn ratio	1:1, 1:1.01 1:1.02, 1:1 1:1.02 1:1.06	1:1 1:1.05 1:1.1, 1:1 1:1.05 1:1.1	1:1, 1:1 1:1, 1:1 (± 2%)	1:1, 1:1 1:1, 1:1 (± 2%)
Grid-side CSC				
DC-link inductor	46 mH	46 mH	40 mH	40 mH
Filter inductor	4.5 mH	4.5 mH	5 mH	5 mH
Filter capacitor	77 µF	77 µF	150 µF	150 µF

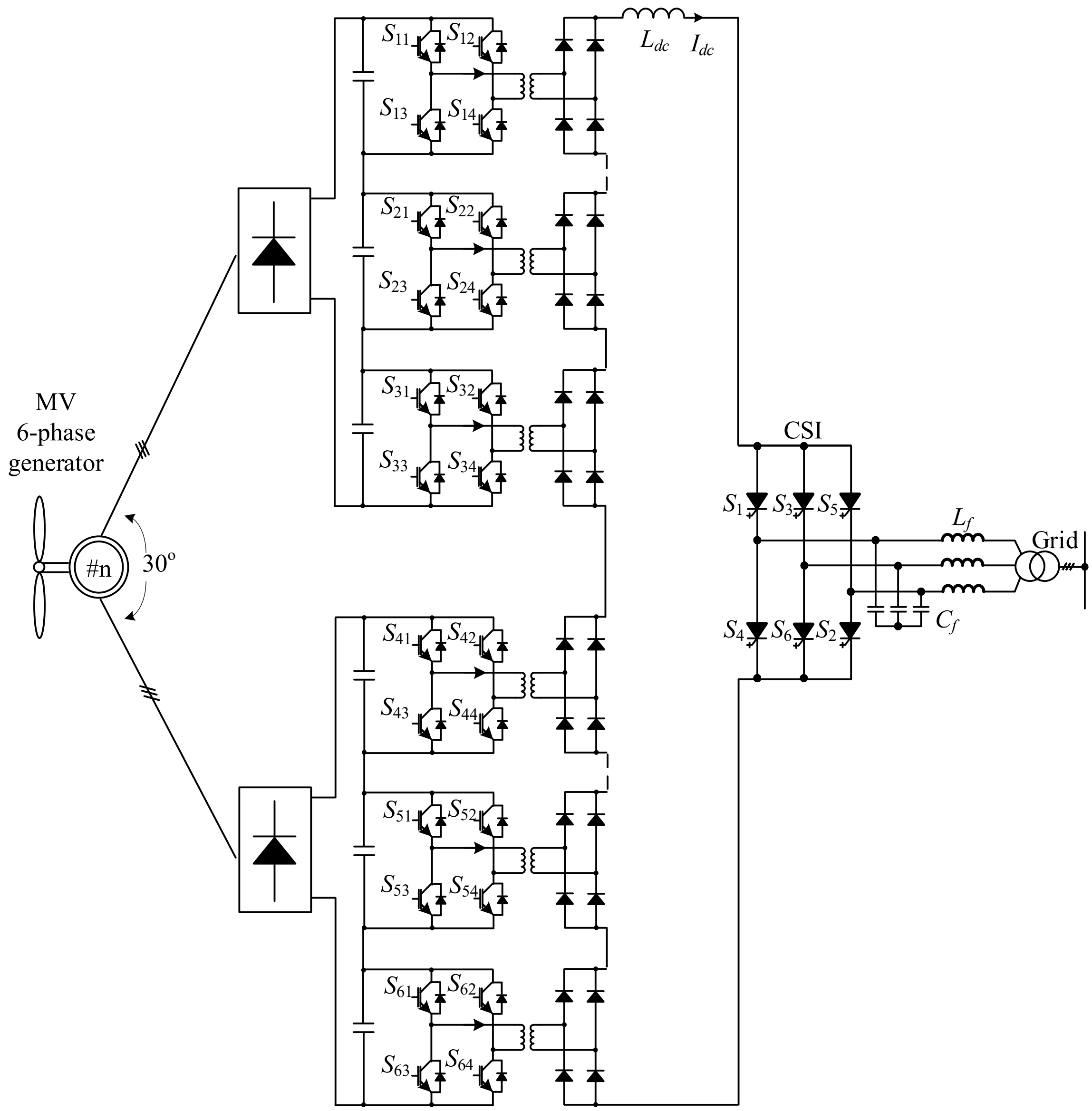
MV
6-phase
generator
#n
30°
S11
S12
S13
S14
S21
S22
S23
S24
S31
S32
S33
S34
S41
S42
S43
S44
S51
S52
S53
S54
S61
S62
S63
S64
Ldc
Idc
CSI
S1
S3
S5
S4
S6
S2
Lf
Grid
Cf

(a)

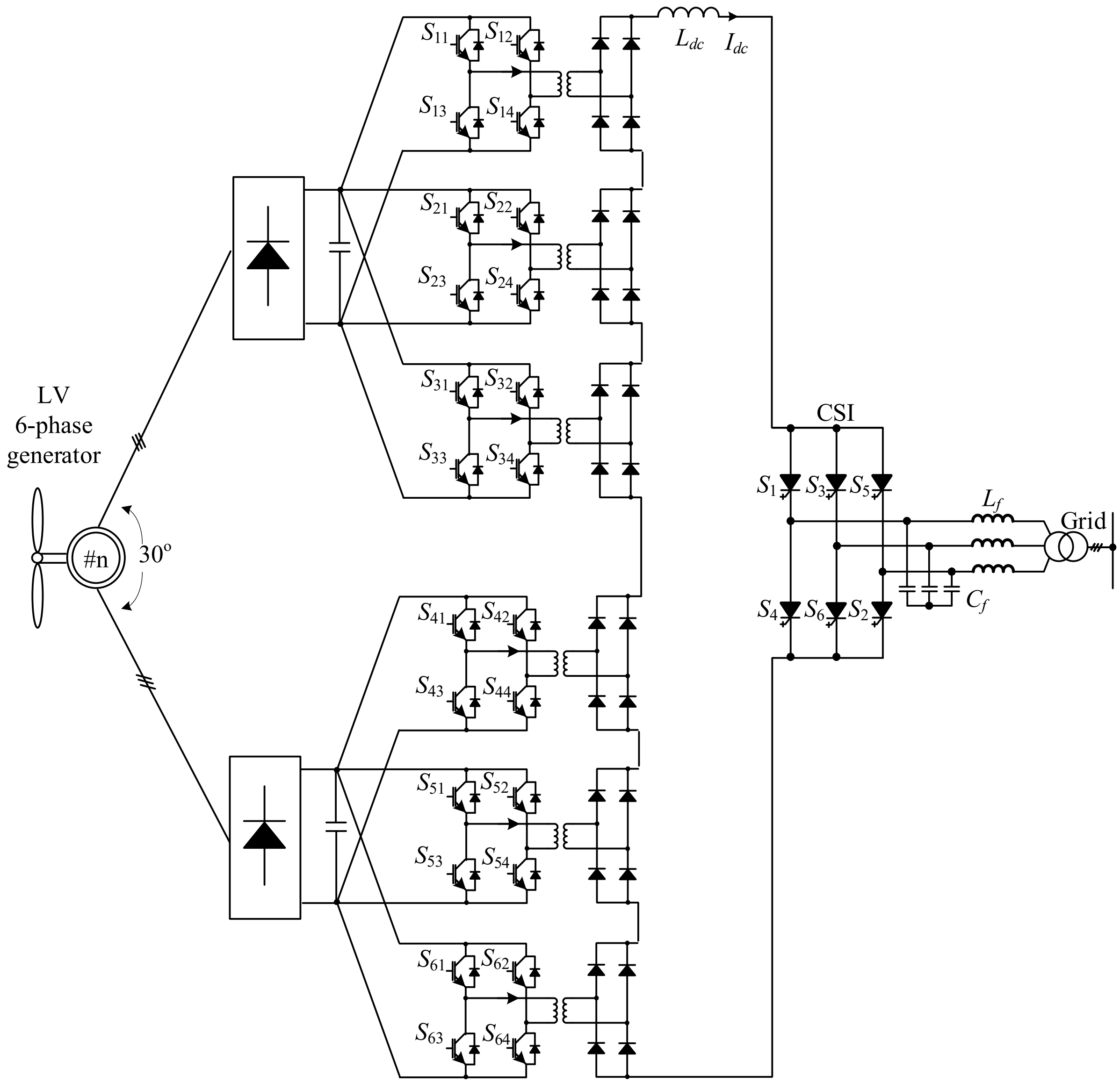

(b)

Figure 3.8: Converter circuit used for simulations: (a) MV version; (b) LV version.

3.4.1 Simulated results of LV converter

Figure 3.9 illustrates the simulated waveforms of the proposed LV version. Before t = 2 s, the converter operates under rated conditions: the wind speed is set to 12 m/s (1 pu), the generator speed tracks its reference at 1 pu, the dc-link current is optimized at 1 pu, and the real and reactive power are fixed at 1 pu and 0 pu, respectively. At t = 2 s, the wind speed decreases to 0.8 pu.

Consequently, the generator speed decreases according to MPPT, the captured wind power reduces to around 0.5 pu, while the dc-link current is decreased to around 0.6 pu to reduce power loss as well as ensuring control objectives at both generator and grid sides simultaneously. At $t = 4$ s, the wind speed increases back to 1 pu. As a result, the generator speed, dc-link current, and captured wind power return to 1 pu.

Figure 3.10 demonstrates the simulated current balancing control. The balancing control functions effectively under both steady state (wind speed = 1 pu) and dynamic states (wind speed reduced from 1 pu to 0.8 pu). Additionally, as previously analyzed, this modular structure remains stable upon disturbance, and the balancing control is optional. For instance, as shown in the figure, without current balancing, the power mismatch among the six modules remains stable and fixed at a maximum of around 10% mainly due to the mismatch in the used transformers. In practice, parameter mismatches are well below 10%, making this control optional.

Figure 3.11 presents the simulated harmonics performance. The 6-phase generator with two sets of isolated 3-phase windings is equivalent to a 3-phase generator + a phase-shifting transformer. As depicted, i_{s1} and i_{s2} are predominantly distorted by the 5th and 7th harmonics, which are eliminated in the generator current i_s.

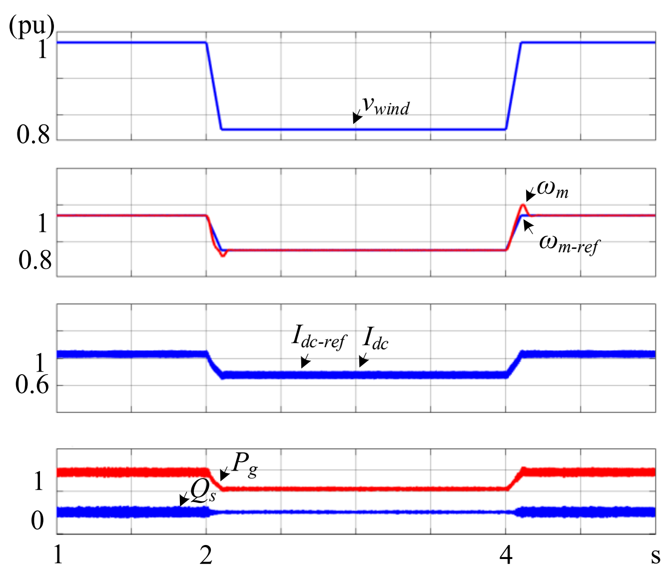

Figure 3.9: Simulated waveforms of the LV converter under steady and dynamic states.

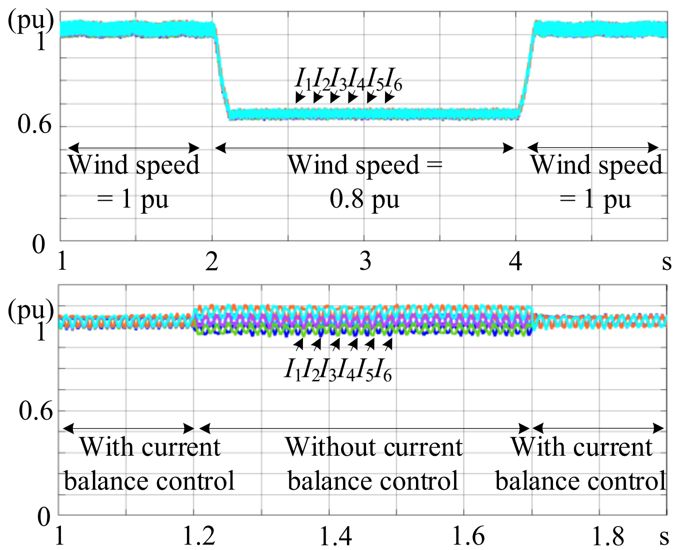

Figure 3.10: Simulated current balancing performance of the LV converter.

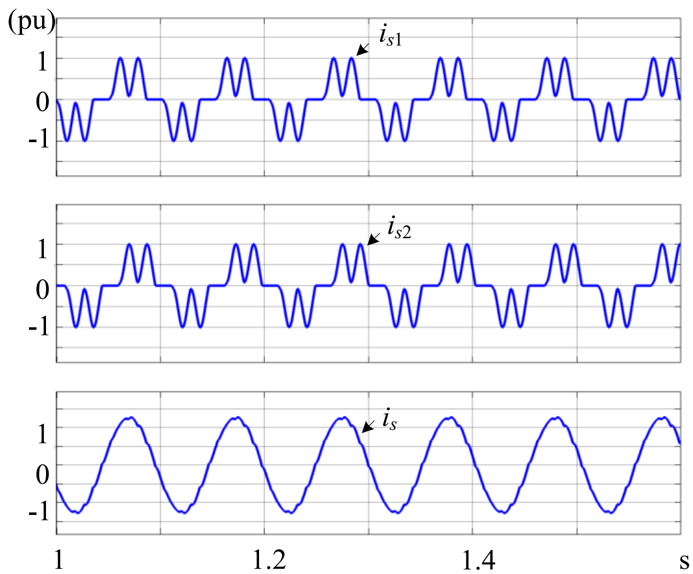

Figure 3.11: Simulated simulated harmonics performance of the LV converter.

3.4.2 Simulated results of MV converter

Figure 3.12 displays the simulated waveforms of the proposed MV converter. Prior to t = 2 s, the converter operates under rated conditions, with the wind speed (v_{wind}) set to 12 m/s (1 pu), the generator speed (ω_m) tracking its reference ($\omega_{m\text{-}ref}$) at 1 pu, the dc-link current (I_{dc}) at 1 pu, and the real power (P_g) and reactive power (Q_s) at 1 pu and 0 pu, respectively. At t = 2 s, the wind speed decreases from 1 pu to 0.8 pu. The generator speed control adjusts to a new speed reference according to MPPT. Once the new speed settles, the captured wind power reduces to around 0.5 pu, and the dc-link current is regulated to around 0.6 pu to ensure control objectives on both sides and minimize power loss. At $t = 4$ s, the wind speed steps up to 1 pu. Consequently, the generator speed, dc-link current, and captured wind power are controlled back to 1 pu. All control variables are well-controlled in both steady and dynamic states.

Figure 3.13 depicts the simulated voltage balancing control. Unlike the LV converter, where current balancing control is optional, the MV converter requires mandatory voltage balancing control. For instance, with a maximum mismatch of 10% in transformer turn ratios, the maximum power mismatch reaches 100% (V_{C4} = 2250 V and V_{C6} = 1100 V) without balancing control. However, with balancing control, capacitor voltages balance well ($V_{C1} = V_{C2} = V_{C3} = V_{C4} = V_{C5} = V_{C6}$ = 1800 V) under both steady (wind speed = 1 pu) and dynamic states (wind speed reduced from 1 pu to 0.8 pu).

Figure 3.14 illustrates the simulated harmonics performance of the MV converter. Similar to the LV version, the diode rectifier currents (i_{s1} and i_{s2}) are highly distorted by the 5th and 7th harmonics, while the generator current i_s does not exhibit such issues.

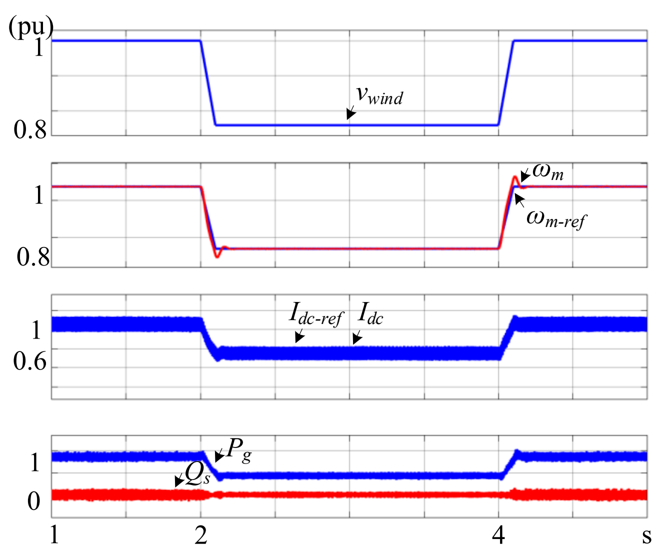

Figure 3.12: Simulated waveforms of the MV converter under steady and dynamic states.

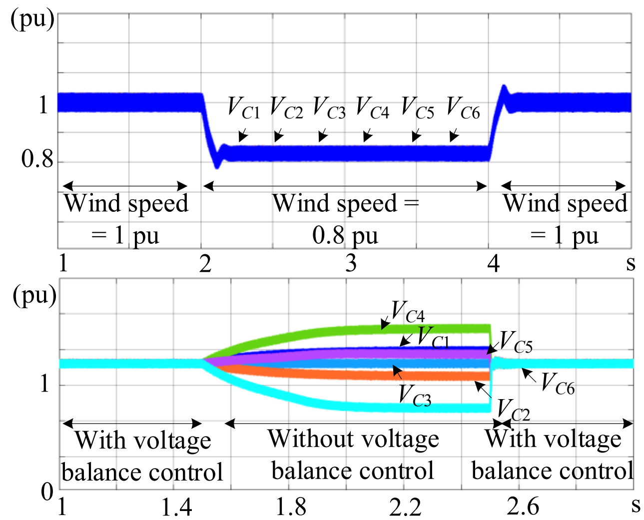

Figure 3.13: Simulated voltage balancing performance of the MV converter.

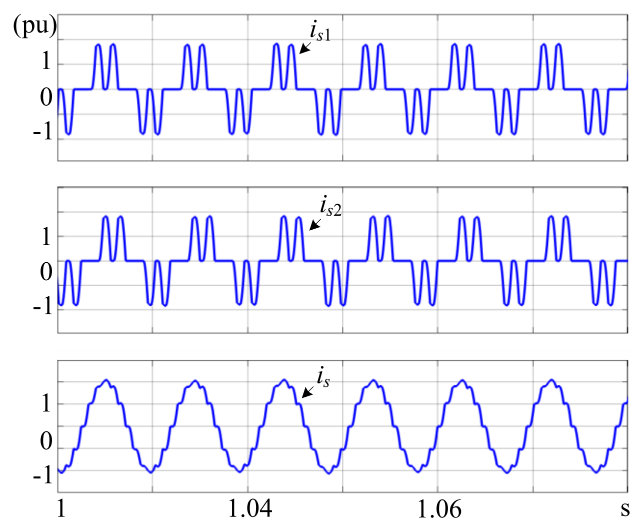

Figure 3.14: Simulated simulated harmonics performance of the MV converter.

3.4.3 Experimental results of LV converter

Lab-scale experiments have been conducted to verify the performance of the proposed converter. Since grid-side controls, including DC-link current control and reactive power control, have been well studied in previous research [8][106], they are not repeated here. As shown in Figure 3.15, grid + variac + phase-shifting transformer is used to simulate the turbine + 6-phase generator system. In experiments, 4 H-bridge modules with different connections are used for both LV and MV converters. The parameters used in experiments are listed in Table 3.1.

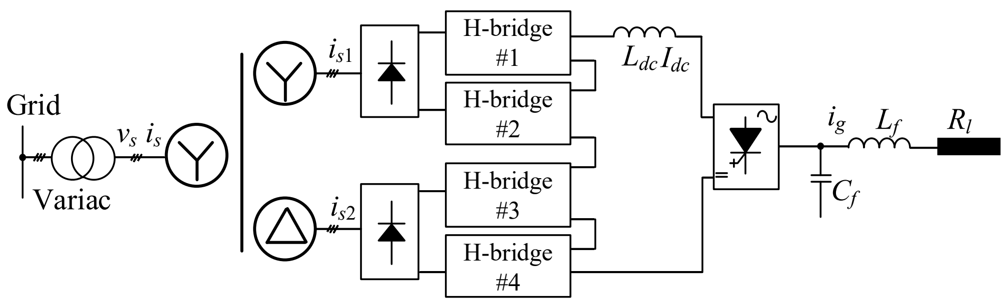

Figure 3.15: Converter circuit used for lab-scale experiments of both LV and MV converters.

Figure 3.16 depicts the experimental results of the LV converter. In the top plot, the converter operates under rated conditions where the RMS of the input grid voltage is 35 V (1 pu), dc-link current I_{dc} = 7 A (1 pu) and load current i_g = 5 A (1 pu). The bottom plot illustrates the response when the input voltage v_s increases from around 0.6 pu to 1 pu, resulting in proportional increases in I_{dc} and i_g. The experimental results demonstrate that the LV converter operates effectively under both steady and dynamic states.

Figure 3.17 displays the experimental waveforms of the input average currents of the LV converter without current balancing control under steady and dynamic states. The transformers listed in Table 3.1 have a tolerance of ±2% in their turn ratios. Under rated conditions, as shown in the top figure, the average currents (I_1, I_2, I_3, and I_4) of the four H-bridge converter modules are almost balanced with a mismatch of around 2%. Similarly, under dynamic conditions, as depicted in the bottom figure, the average currents increase from around 0.6 pu to 1 pu, maintaining a similar level of imbalance. As previously analyzed, such current imbalance due to parameter tolerance is small, fixed, and stable. This aligns well with the earlier conclusion that current balancing control is optional.

Figure 3.18 illustrates the experimental harmonic performance of the LV converter under rated conditions. i_{s1} and i_{s2} represent two secondary currents of the phase-shifting transformer, while i_s denotes the primary current of the phase-shifting transformer. Notably, i_{s1} and i_{s2} exhibit significant distortion primarily from the 5th and 7th harmonics, whereas i_s demonstrates considerably better harmonic performance. However, it is worth noting that i_s still contains some 5th and 7th harmonics, attributed to transformer parameter tolerance.

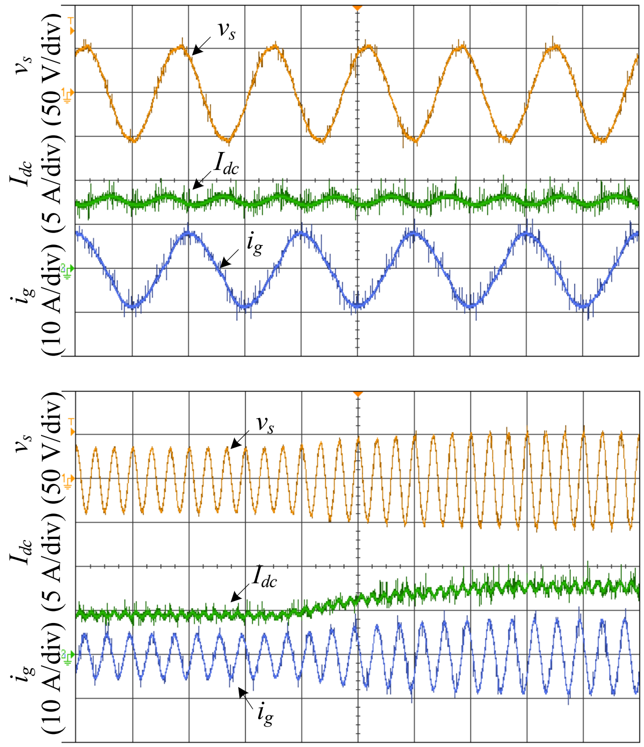

Figure 3.16: Experimental waveforms of the proposed LV converter under steady and dynamic states.

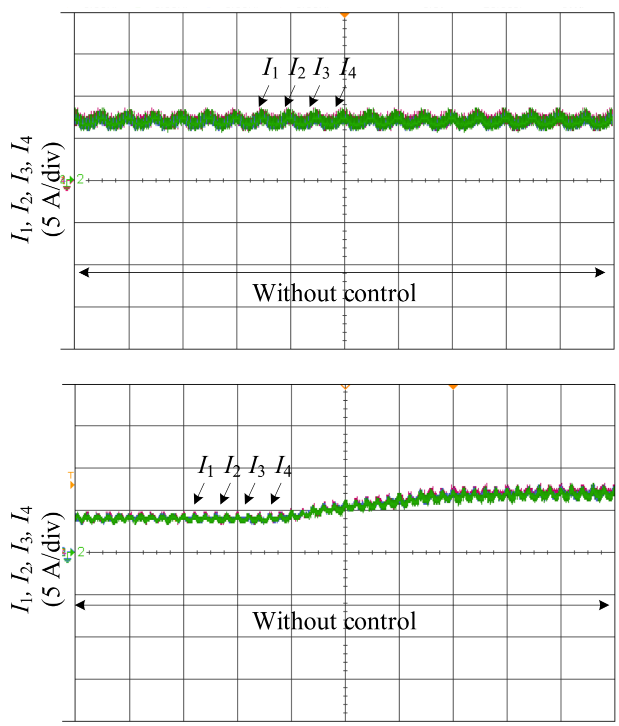

Figure 3.17: Experimental waveforms of current balancing of the proposed LV converter.

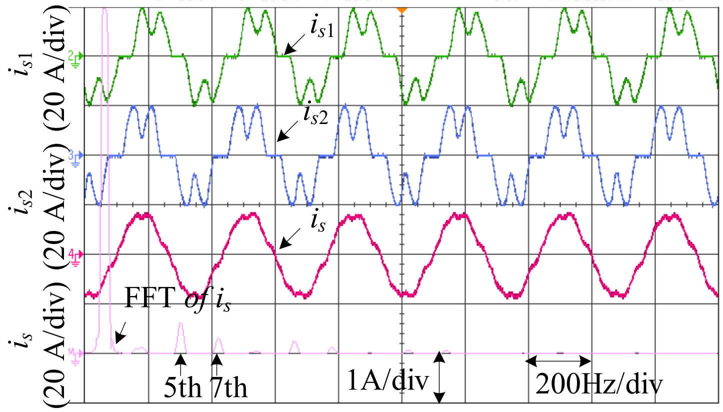

Figure 3.18: Experimental harmonic performance of the proposed LV converter.

3.4.4 Experimental results of MV converter

Figure 3.19 illustrates the experimental waveforms of the MV version under both steady and dynamic states. The converter operates successfully under rated conditions, as depicted in the top figure, where RMS of v_s is 50 V (1 pu), I_{dc} = 7 A (1 pu), and i_g = 5 A (1 pu). In the bottom figure, when v_s increases from around 0.6 pu to 1 pu, both I_{dc} and i_g increase proportionally from around 0.6 pu to 1 pu accordingly. The experimental results verify that the MV converter operates effectively under both steady and dynamic states.

Figure 3.20 presents the experimental results of the balancing control under both steady and dynamic states. As discussed earlier, despite the small tolerance within ±2% in the turn ratios of the used transformers, significant voltage imbalance occurs, necessitating mandatory voltage balancing control. As depicted in the top figure, without voltage balancing control, the maximum imbalance occurs between the capacitor voltages of H-bridge modules 3 and 4, with $V_{C3} = 1.35V_{C4}$. However, with the proposed voltage balancing control, well-balanced voltages are achieved under both steady and dynamic states, as shown in both figures.

Figure 3.21 showcases the experimental harmonic performance of the MV converter under rated conditions. Similar to the LV version, i_{s1} and i_{s2} exhibit significant distortion from the 5th and 7th harmonics, while i_s demonstrates better harmonic performance thanks to the use of multi-phase generators.

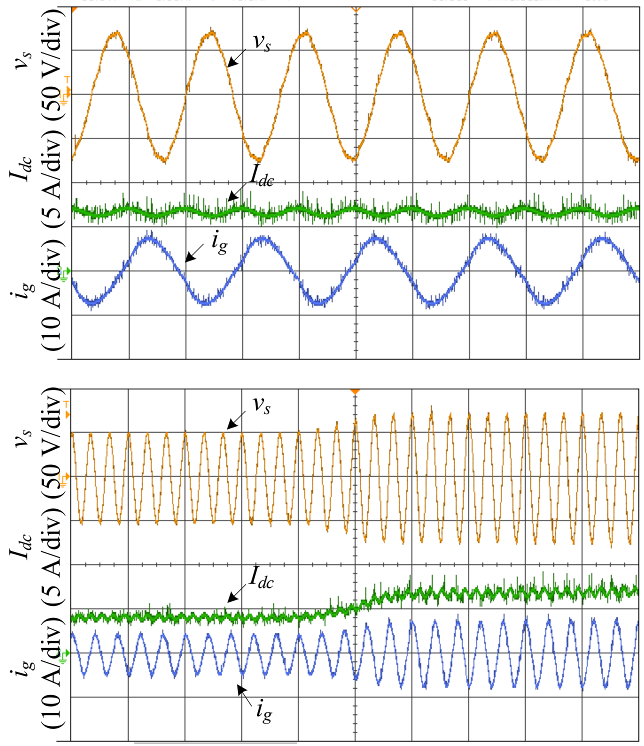

Figure 3.19: Experimental waveforms of the proposed MV converter under steady and dynamic states.

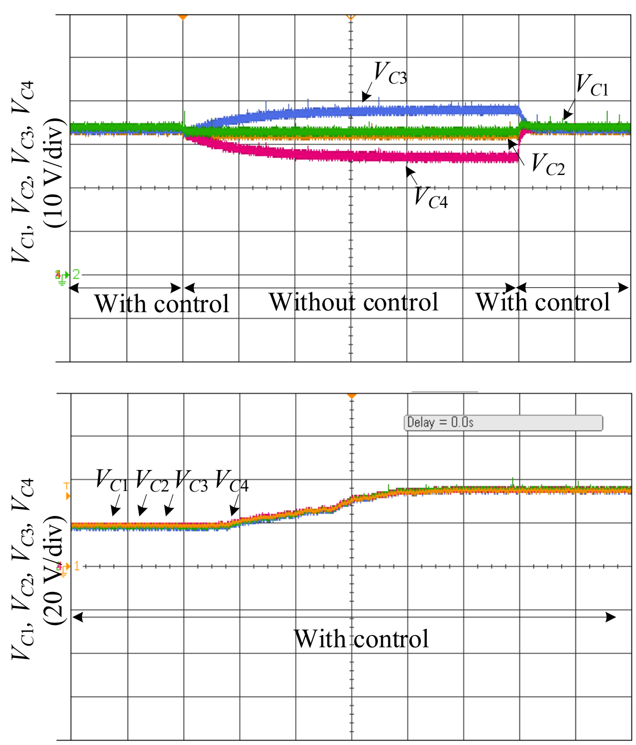

Figure 3.20: Experimental waveforms of voltage balancing of the proposed MV converter.

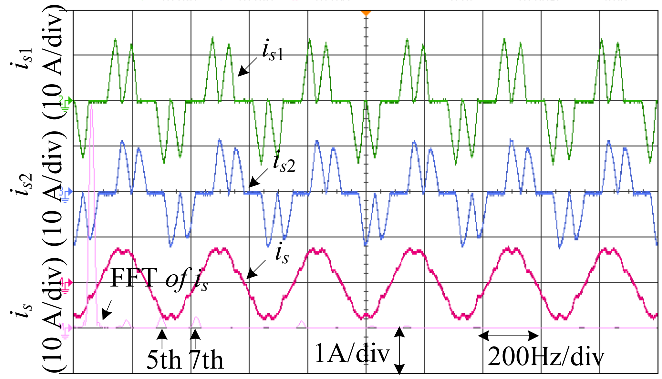

Figure 3.21: Experimental harmonic performance of the proposed MV converter.

In summary, the following points have been verified through analysis, simulations and experiments: 1) the proposed converters, including the LV converter and the MV converter, maintain the advantages associated with passive rectifiers, 2) the proposed converters offer superior current harmonic performance thanks to the use of multi-phase generators, 3) the proposed converters exhibit reduced size and weight due to the use of MFTs rather than LFTs, and 4) the proposed controls including balancing controls work well for the proposed converters.

3.5 Conclusions

The LFT and passive rectifier-based converters are well-studied power converters utilized on the generator side of WECS. The LFT, a mature technology, serves to isolate the generator from HVDC levels, allowing the use of generators with regular insulation levels. On the other hand, its large size and weight introduce significant burden to WECS where the space in nacelles is limited. The use of passive rectifiers offers WECS with low cost, high reliability, simplicity, and scalability. However, the utilization of passive rectifiers results in highly distorted generator stator currents, leading to increased power losses and reduced lifespan of generators. Though the proposed phase-shifting transformer-based converter introduced in Chapter 2 well solves this issue, the adoption of a phase-shifting transformer, also an LFT, suffers from large size and weight.

To address the respective challenges associated with the bulky LFT and passive rectifiers while preserving their respective advantages and functions, a new type of power converter is proposed. It is a multi-phase generator-based converter comprising a multi-phase generator, diode rectifiers, and a modular MFT-based DC-DC converter on the generator side, and a conventional CSC on the grid side. The use of diode rectifiers allows the proposed converter to retain advantages associated with diode rectifiers, such as low cost and high reliability, while the utilization of a multi-phase generator enables the elimination of specific current harmonics generated by diode rectifiers, thereby significantly improving the performance of generator stator current harmonics, and reducing power losses, ultimately prolonging the service life of generators. The employment of MFT allows the use of generators with regular insulation requirements as well as contributing to reduced size and weight of WECS compared with the LFT. Considering that the MFT with high-voltage insulation requirements and high-power ratings are not mature, modular MFTs are employed. Each MFT carries one part of the rated power, reducing its manufacturing burden.

To enable the utilization of low-cost, low-voltage, low-current switches for generator systems with different voltage ratings, two versions of the proposed converter have been developed. The LV converter is tailored for generators with LV ratings, while the MV converter is designed for generators with MV ratings. Control schemes have been devised for both conversion systems. These schemes share common features such as generator-side MPPT control and grid-side DC-link current and reactive power controls. However, the MV converter necessitates mandatory voltage balancing control, whereas an optional current balancing control is suggested for the LV converter.

Both simulations and experiments have been conducted to validate the performance of the proposed converter and effectiveness of proposed controls.

Chapter 4

Generator-Side Active Rectifier-Based Converter with Modular Medium-Frequency Transformers

In CSC-type series DC-based WECS, the use of passive rectifier-based converters on the generator side offers advantages of low cost, high reliability, and scalability, but it generates highly distorted generator stator currents, resulting in significant torque ripples and a reduced lifespan of the generator. The use of LFT, including both conventional isolated transformers and phase-shifting transformers, provides a practical solution for addressing the generator insulation issue, but it suffers from large size and weight. On the other hand, active rectifier-based converters present superior current harmonics performance, making them a good candidate for addressing issues associated with passive rectifiers. Similarly, compared to LFT, MFT features smaller size and weight, making it a favorable solution for WECS, where space in the turbine nacelle is limited. In this chapter, a new converter using both an active rectifier and a modular MFT is proposed. The active rectifier ensures superior generator stator current harmonics performance, and the modular MFT gives the conversion system smaller size and weight. This chapter begins with an introduction to the proposed power converter, including its operational principles, features, and controls. Finally, the performance of the proposed converter is validated through both simulations and laboratory-scale experiments.

4.1 Existing generator-side converters

Figure 4.1 illustrates the existing passive rectifier-type converters used on the generator side of CSC-type series DC-based WECS. While passive rectifiers offer benefits such as low cost, high reliability, and scalability to WECS, they produce highly distorted generator stator current harmonics, resulting in increased power loss and reduced lifespan of generators. In contrast, Figure 4.2 illustrates the existing active rectifier-type converters used on the generator side of CSC-type series DC-based WECS. Although active rectifiers cannot match their counterpart, passive rectifiers, in terms of cost, reliability, and scalability, they are also a mature technology and offer superior harmonics performance. This contributes to reduced power loss and increased lifespan of generators.

In series DC-based WECS, either LFT or MFT is utilized to ensure the use of generators with standard insulation levels. LFT [46-51], although a mature technology, is burdened by larger size and weight. Conversely, MFT [41-43] [52-53] offers the advantage of smaller dimensions and weight, making it well-suited for WECS installations where space within the turbine nacelle is constrained. However, the application of MFT with high-voltage insulation requirements and high-power ratings is not yet matured in the industry. To alleviate manufacturing challenges, a modular design has been proposed, wherein multiple MFT units are employed, each handling a portion of the total power rating.

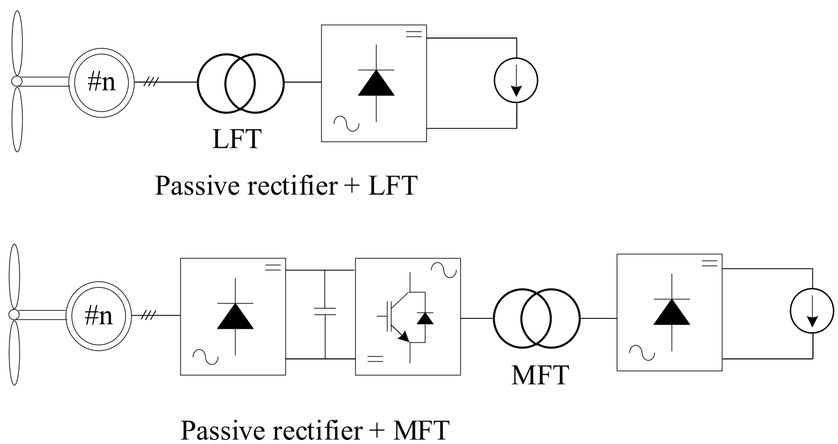

Figure 4.1: Existing generator-side converters with passive rectifies.

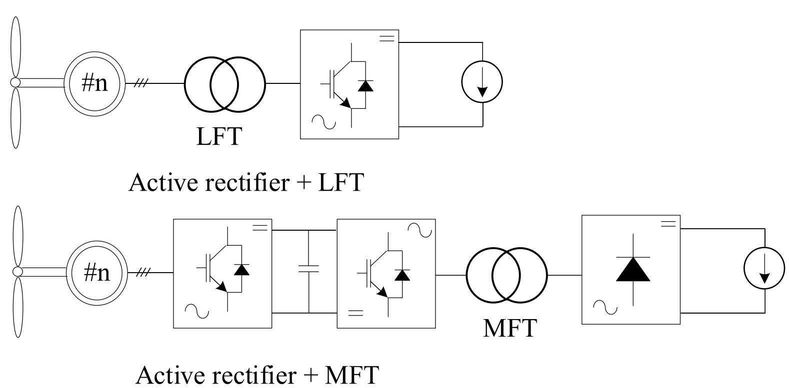

Figure 4.2: Existing generator-side converters with active rectifies.

In summary, depending on the types of transformers and converters utilized on the generator side of WECS, generator-side converters can be realized through four combinations: passive converter + LFT, passive converter + MFT, active converter + LFT, and active converter + MFT. Among these combinations, the last one, comprising an active converter + MFT, not only delivers superior generator stator current harmonic performance but also offers compact size and weight, making it a promising candidate for series DC-based WECS. However, this type of converter has not been extensively discussed for series DC-based WECS in the literature. To the best of the author's knowledge, only one such converter, comprising a matrix converter and an MFT, has been developed for WECS. While retaining all the associated advantages, this matrix converter-based system does have a couple of drawbacks, including the requirement of a high number of switches and the utilization of complex modulation, commutation, and control schemes.

4.2 Active rectifier-based converter with modular medium-frequency transformers

To address the challenges associated with the matrix converter-based WECS while retaining all the advantages of the active converter + MFT configuration, a new conversion system has been developed and is presented in this chapter, as shown in Figure 4.3.

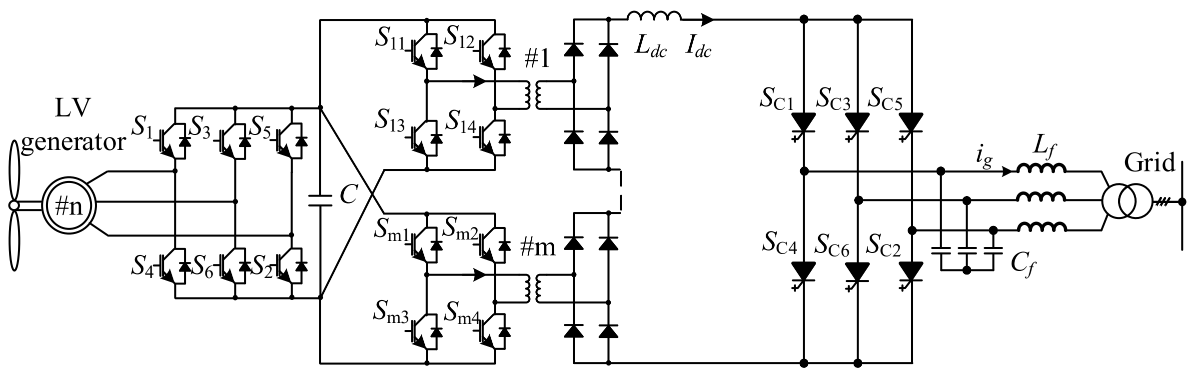

Figure 4.3: Proposed generator-side converter with active rectifier and a modular MFT: LV version.

As depicted in Figure 4.3, the proposed conversion system for high-power LV PMSG #n comprises an active rectifier (a conventional 2-level VSR) and a modular MFT-based converter on the generator side, along with a conventional CSC on the grid side. The modular MFT-based converter consists of m identical H-bridge converters connected in parallel at the input and in series at the output. These MFTs serve to isolate the generator from high voltage, allowing for the use of generators with regular insulation levels. The modular structure of the MFT-based converter enables the utilization of low-cost low-voltage low-current devices and distributes the power evenly, with each MFT carrying $1/m$ of the rated power, thereby reducing the manufacturing burden of MFT.

The active rectifier offers superior generator stator current harmonics performance compared with passive rectifiers. The use of modular MFTs enables size and weight reductions in comparison with LFT. Another advantage of the proposed converter is that its design can follow existing ones. For instance, the design of the 2-level VSC, which includes switch selection, filter design, and DC voltage selection, remains consistent with the existing three-phase 2-level VSCs used in WECS [106]. Similarly, the number of modules (m) in the modular MFT-based converter is determined in the same manner as the multi-phase generator-based converter described in Chapter 3. Additionally, the grid-side CSC, along with passive components such as the DC inductor and output AC LC filter, is designed using the same methodology as existing grid-connected CSCs [8].

To allow the use of low-cost, low-voltage low-current switches, the proposed converter is extended to different versions for turbine-generator systems with different power and voltage ratings.

Figure 4.4 illustrates the converter modified for MV PMSG systems. In contrast to LV PMSG systems, MV PMSG systems operate at high voltage and relatively low current. Therefore, unlike the converter shown in Figure 4.3 for LV PMSG systems, the converter for MV PMSG systems utilizes a different configuration for the modular MFT-based converter. As depicted in Figure 4.4, the modules of the MFT-based converter are connected in series at the input, enabling the use of low-voltage switches.

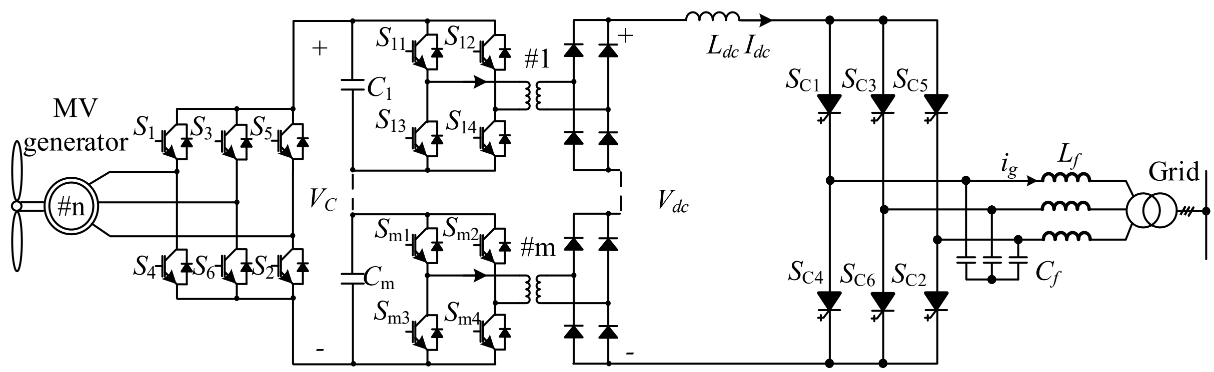

Figure 4.4: Proposed generator-side converter modified for MV PMSG with 2-level VSR.

For MV WECS, the utilization of multi-level VSRs provides several advantages over two-level VSRs, including a smaller filter size and the elimination of the need for series-connected switches. Figure 4.5 illustrates another modified version of the proposed converter, where the two-level VSR is replaced with the three-level NPC converter. NPC-based WECS is a well-proven technology in the industry and can be directly adopted here [8].

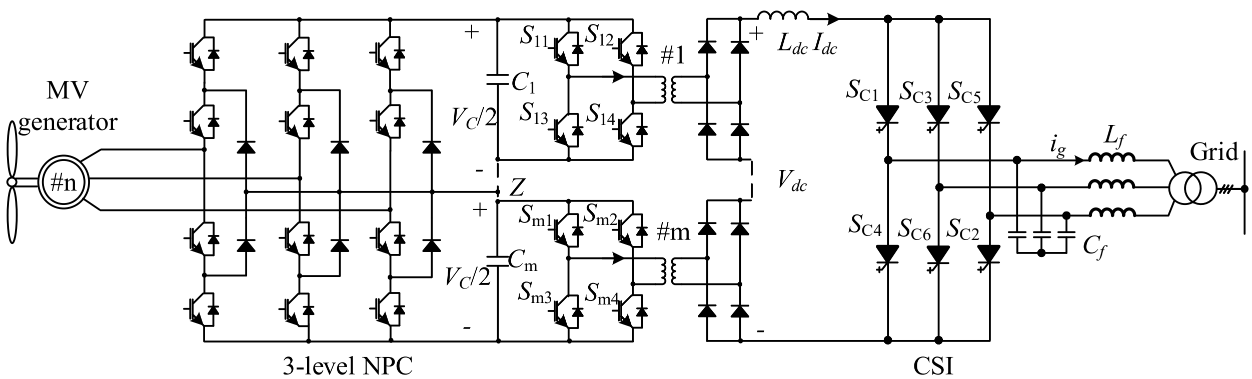

Figure 4.5: Proposed generator-side converter modified for MV PMSG with 3-level NPC.

4.3 Control scheme

The proposed CSC features a distinctive structure, comprising a two-stage VSC on the generator side and a CSC on the grid side. Theoretically, it can operate as either a VSC or a CSC. In the VSC mode, as depicted in Figure 4.6, the voltage V_C is controlled to remain constant. Meanwhile, the modular MFT-based converter and the grid-side CSC function as the grid-side converter, allowing for variable dc current (I_{dc}). Conversely, in the CSC mode, the dc-link current I_{dc} is controlled to be constant, while the modular MFT-based converter and the 2-level VSC function as the generator-side converter, with variable voltage V_C. The CSC mode preserves unique advantages for the series DC-based wind system. On the other hand, the VSC mode simplifies the control system design for the generator-side converter. To ensure the benefits of both modes, a hybrid control scheme that combines the CSC and VSC modes is proposed.

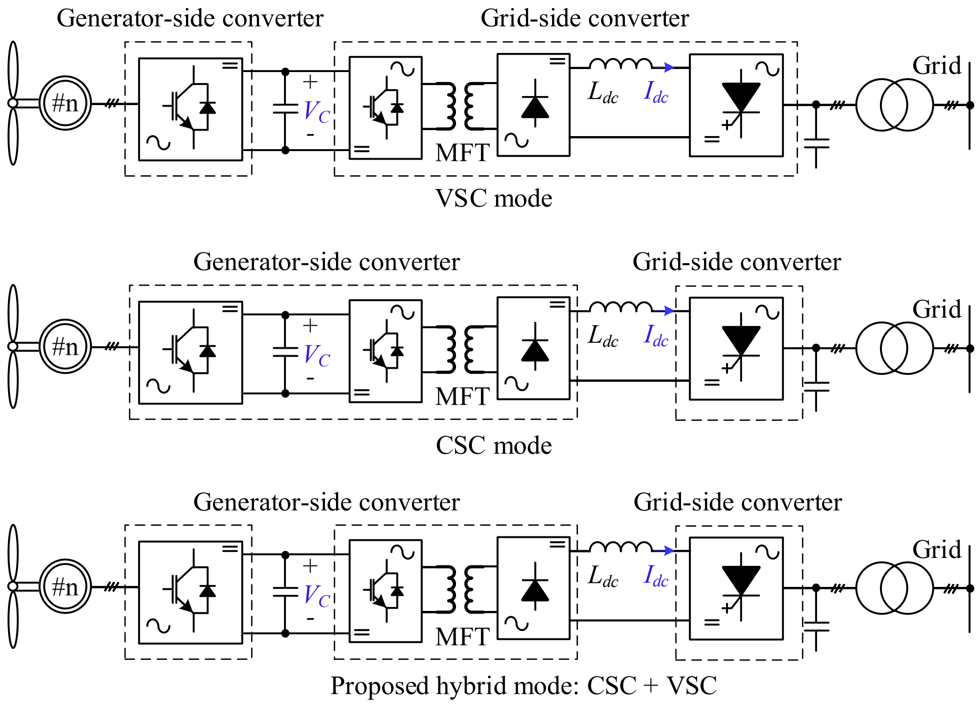

Figure 4.6: Simplified circuit of the converter under VSC and CSC modes.

The overall control strategy of the CSC-type series DC-based WECS has been discussed in the previous chapter and will not be repeated in this chapter. The same as Chapter 2 and Chapter 3, the power converter, comprising a generator-side converter #n and a grid-side CSC #n, is taken as an example to illustrate the control system design of the proposed converter.

The hybrid control scheme is illustrated in Figure 4.7, includes three parts: generator-side control, control of the modular MFT-based converter, and grid-side control.

4.3.1. Control of generator-side active rectifier

Generator-side controls include MPPT and generator speed control. The generator-side active rectifier controls the active wind power, while its output voltage, the DC voltage V_{dc}, is kept constant by controlling the MFT-based converter. Based on this premise, the proposed converter is simplified and equivalent to the one shown in Figure 4.8, where the two-level VSC is used as an example to illustrate the control, and a constant voltage source represents the load of the two-level VSC.

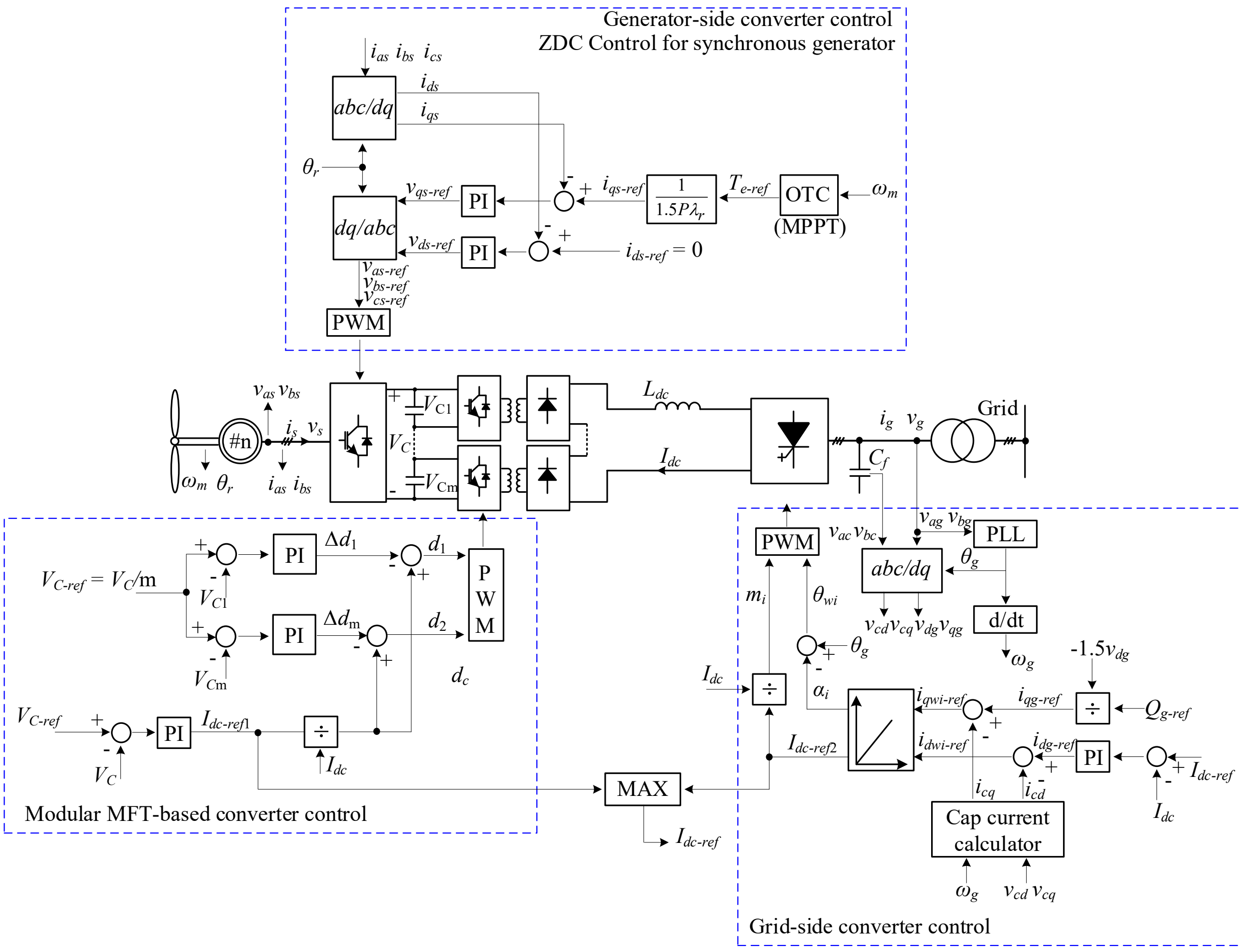

Figure 4.7: Proposed hybrid control for the proposed converter.

All well-proven controls, including zero *d*-axis current (ZDC) control, maximum torque per ampere control, and unity power factor control, can be applied to the proposed converter. In the following, ZDC is taken as an example. As shown in Figure 4.7, the MPPT is achieved by optimal torque control (OTC), and the generator is controlled by ZDC [19].

According to the measured rotor speed ω_m, OTC outputs the reference torque $T_{e\text{-}ref}$ which then provides the torque-producing stator current reference $i_{qs\text{-}ref}$. $i_{qs\text{-}ref}$ is calculated based on the ZDC scheme, in which the *d*-axis stator current reference $i_{ds\text{-}ref}$ is set to 0.

$$T_e = \frac{3}{2} P \lambda_r i_{qs} \tag{4.1}$$

where P is the number of pole pairs and λ_r is the rotor flux linkage.

The measured three-phase stator currents (i_{as}, i_{bs}, i_{cs}) are transformed into dq-axis currents (i_{ds}, i_{qs}) which are then compared with their respective reference currents ($i_{ds\text{-}ref}$, $i_{qs\text{-}ref}$). The resultant errors are then sent to PI controllers, generating the dq-axis reference voltages ($v_{ds\text{-}ref}$, $v_{qs\text{-}ref}$) for the generator-side converter. The use of dq/abc transformation gives abc-frame reference voltages ($v_{as\text{-}ref}$, $v_{bs\text{-}ref}$, $v_{cs\text{-}ref}$) which are then sent to the PWM generation block. In this study, a conventional SPWM is used. and in both abc/dq and dq/abc transformations, the rotor position angle θ_r is used. The stator voltages of the generator are then controlled according to their references such that the active power is controlled.

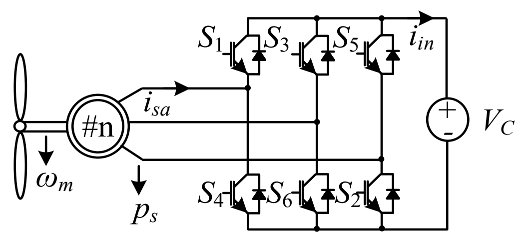

Figure 4.8: Equivalent circuit for generator-side active rectifier control.

4.3.2. Control of modular MFT-based converter

The MFT-based modular converter controls the DC voltage V_{dc} to remain constant across its full operational range. The dc current I_{dc} is regulated by the grid-side converter. Therefore, from the perspective of control system design, the proposed converter is equivalent to the one depicted in Figure 4.9. The input of the MFT-based converter is represented by a voltage-controlled current source I_{in}, and the output by a constant current source. It's important to note that the constant current source has varying values under different wind speeds, which will be addressed in the control of the grid-side converter.

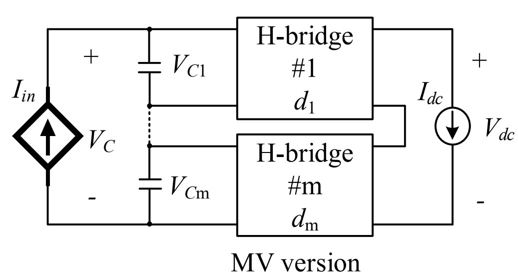

Figure 4.9: Equivalent circuit for MFT-based modular converter: MV version with series connection at input.

Moreover, the modular structure of the MFT-based converter necessitates power balancing control. As illustrated in Figure 4.9, all modules share the same I_{dc} output, but there's an issue of voltage imbalance due to parameter mismatches. For instance, although the turn ratio of all transformers is intended to be 1:1, this may not be guaranteed due to manufacturing tolerances. Consequently, modules with higher turn ratios experience higher capacitor voltages. However, the structure of the series connection, both at the input and output, is not stable in the event of a mismatch, necessitating voltage balancing control.

As shown in Figure 4.7, the measured DC voltage V_C is compared with its reference $V_{C\text{-}ref}$ value. Note that the reference voltage $V_{C\text{-}ref}$ is chosen to be consistent with existing VSC-based wind systems [106], thus not repeated here. The resulting error is fed into the PI controller, which generates the current reference $I_{dc\text{-}ref1}$. The required duty cycle d_c for DC voltage control is then obtained by comparing the reference current $I_{dc\text{-}ref1}$ with the actual DC current I_{dc}.

To ensure voltage balancing, voltage balancing control is implemented. As depicted in Figure 4.7, the measured capacitor voltages V_{C1} and V_{Cm} are compared with their respective reference values. Subsequently, these errors are processed by individual PI controllers to generate the required duty cycles for voltage balancing. The final duty cycle for each module comprises two components: d_c for DC voltage control and Δd_m for voltage balancing. The former ensures DC voltage control, while the latter ensures voltage balancing across modules.

The DC current reference $I_{dc\text{-}ref1}$ as shown in Figure 4.7 is the current obtained upon achieving DC voltage control under MPPT conditions. Essentially, it represents the current necessary for MPPT operation. Conversely, if the actual current falls below this reference value $I_{dc\text{-}ref1}$, MPPT is not achieved. Consequently, this DC current reference $I_{dc\text{-}ref1}$ is transmitted to the grid-side converter to determine the final DC-link current reference.

The modular MFT-based converter for the LV PMSG system employs parallel connections at the input and series connections at the output, as illustrated in its equivalent circuit in Figure 4.10. This configuration differs from the series-connected input and series-connected output configuration depicted in Figure 4.9. The parallel-input, series-output configuration is stable, unlike the former, where the current imbalance introduced by parameter mismatches remains stable. Consequently, current balancing control becomes optional. Detailed discussions and analyses concerning optional current balancing have been thoroughly addressed in the preceding chapter and will not be reiterated here.

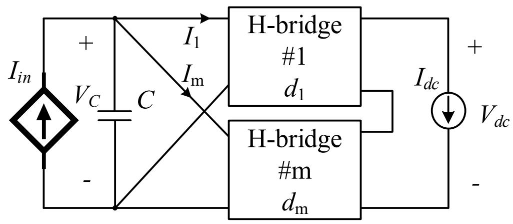

Figure 4.10: Equivalent circuit for MFT-based modular converter: LV version with parallel connection at input.

4.3.3. Control of grid-side CSC

The grid-side converter is responsible for the DC current control and reactive power control. The simplified equivalent circuit is shown in Figure 4.11, where the input is represented by a current controlled voltage source in series with the dc inductor.

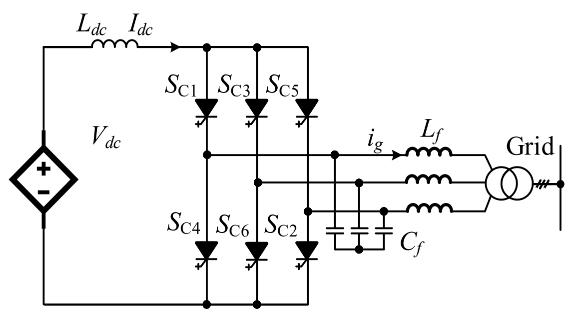

Figure 4.11: Equivalent circuit for grid-side CSC.

The grid-side control includes two independent control loops in the *dq* frame, one is the dc current control loop and the other reactive power control loop. The *d*-axis grid current reference ($i_{dg\text{-}ref}$) is obtained by the dc current PI controller. The reference for the *q*-axis grid current ($i_{qg\text{-}ref}$) is obtained according to the following reactive power reference ($Q_{g\text{-}ref}$) and the *d*-axis grid voltage (v_{dg}). i_{dg} and i_{qg} are *d*-axis and *q*-axis grid currents respectively.

$$
\begin{aligned}
P_s &= \frac{3}{2} v_{dg} i_{dg} \\
Q_s &= -\frac{3}{2} v_{dg} i_{qg}
\end{aligned}
\tag{4.2}
$$

The calculation of the dq-axis PWM currents ($i_{dwi\text{-}ref}$ and $i_{qwi\text{-}ref}$) requires the compensation of the filter capacitor currents.

$$\begin{cases} i_{dwi-ref} = i_{dg-ref} + i_{cd} = i_{dg-ref} - \omega_g C_f v_{cq} \\ i_{qwi-ref} = i_{qg-ref} + i_{cq} = i_{qg-ref} + \omega_g C_f v_{cd} \end{cases} \tag{4.3}$$

where i_{cd} and i_{cq} are the dq-axis capacitor currents, and the v_{cd} and v_{cq} are the dq-axis capacitor voltages.

$$\begin{cases} v_{cd} = v_{dg} - \omega_g L_f i_{qg} \\ v_{cq} = \omega_g L_f i_{dg} \end{cases} \tag{4.4}$$

The DC current reference ($I_{dc\text{-}ref2}$) and delay angle (α_i) of the grid-side CSC are calculated based on the following.

$$\begin{aligned} I_{dc-ref2} &= \sqrt{(i_{dwi-ref})^2 + (i_{qwi-ref})^2} \\ \alpha_i &= \tan^{-1}(i_{qwi-ref} / i_{dwi-ref}) \end{aligned} \tag{4.5}$$

It's essential to note that both the DC current references $I_{dc\text{-}ref1}$ generated by the generator-side control and $I_{dc\text{-}ref2}$ generated by the grid-side control need to be taken into consideration to determine the final DC current reference $I_{dc\text{-}ref}$. The larger of the two references is selected to be the DC current reference $I_{dc\text{-}ref}$ to ensure that controls on both sides are achieved simultaneously.

The modulation index (m_i) for the CSC is then obtained by $I_{dc\text{-}ref2}/I_{dc}$. And the angle of the PWM current (θ_{wi}) is calculated based on $\theta_{wi} = \theta_g - \alpha_i$ in which θ_g is the grid voltage angle. After applying m_i and θ_{wi} to the grid-side CSC, reactive power and dc current controls are achieved. Upon applying $I_{dc\text{-}ref}$, the controls at both sides can be ensured.

4.4 Simulation and experimental results

MATLAB simulations have been carried out to evaluate the performance of the proposed converter. The wind turbine model is provided by MATLAB, and MPPT control is implemented using the optimal tip ratio. To simplify the process and effectively assess the converter's performance, a two-level VSC is utilized on the generator side as an illustrative example. For the purpose of investigating the balancing control performance, six modular H-bridge converters are employed. These converters feature a maximum tolerance of 10% in the turn ratios of the six MFTs. This tolerance variation allows for thorough evaluation of the balancing control functionality. Key parameters utilized in the simulations are listed in Table 4.1. Figure 4.12 shows the converter circuit used for simulations.

Table 4.1: Simulation and experiment parameters

Parameters	Simulation	Experiment
Nominal power	1 MW	866 W
Grid voltage, V_g	4160 V	110 V
Generator	PMSG, 4000 V	Variac
Generator-side converter		
Filter inductor, L	20 mH	10 mH
DC voltage, V_{dc}	8000 V	160 V
Switching frequency	1 kHz	1 kHz
MFT-based modular converter		
Number of modules, m	6	2
Transformer	6	2
Transformer turn ratio	1:1, 1:1.01, 1:1.02, 1:1.03, 1:1.04, 1:1.05	1:1, 1: 1 (Extra resistor R_p = 600 Ω)
Capacitor, C_{m}	1000 uF	1000 uF
Switching frequency	1.2 kHz	1.2 kHz
Grid-side converter		
DC inductor, L_{dc}	45 mH	45 mH
Filter inductor, L_f	5 mH	5 mH
Filter capacitor, C_f	70 uF	100 uF
Switching frequency	540 Hz	540 Hz

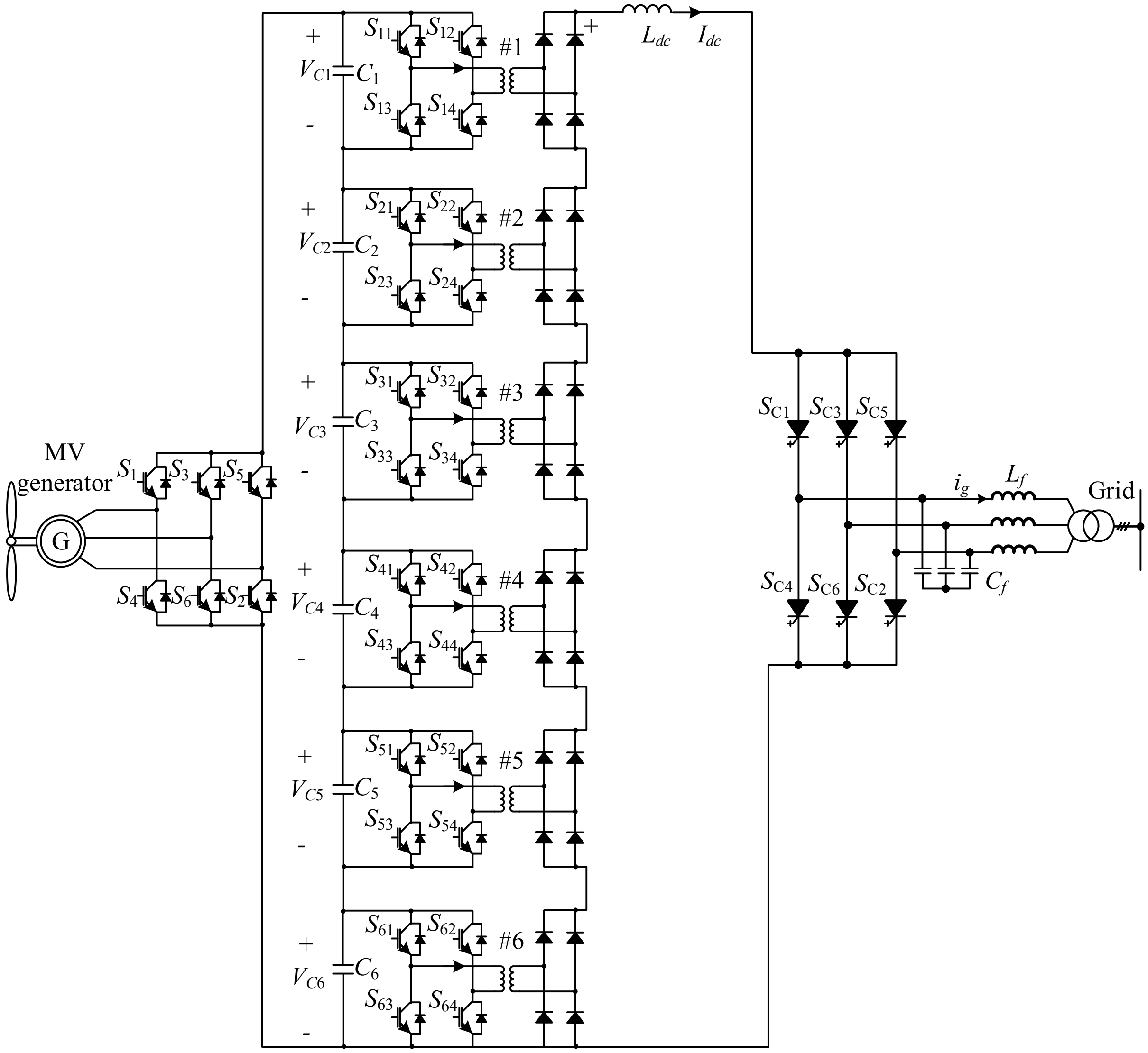

Figure 4.12: Converter circuit used for simulations.

4.4.1 Simulated results

Figure 4.13 displays the simulated waveforms during both steady and dynamic states. Before t = 1.5 sec, the converter operates under rated conditions. On the generator side, the generator torque T_e is controlled at its reference value $T_{e\text{-}ref}$ obtained by the OTC, and both terminal voltage (v_{as}) and stator current (i_{as}) remain at rated values. The controls of the MFT-based converter are also successfully achieved. The DC voltage is controlled at 1 pu and evenly distributed among the capacitors ($V_{C1} = V_{C6}$). On the grid-side, the DC current is controlled at its rated value, and the real power and reactive power are maintained at 1 pu and 0 pu, respectively.

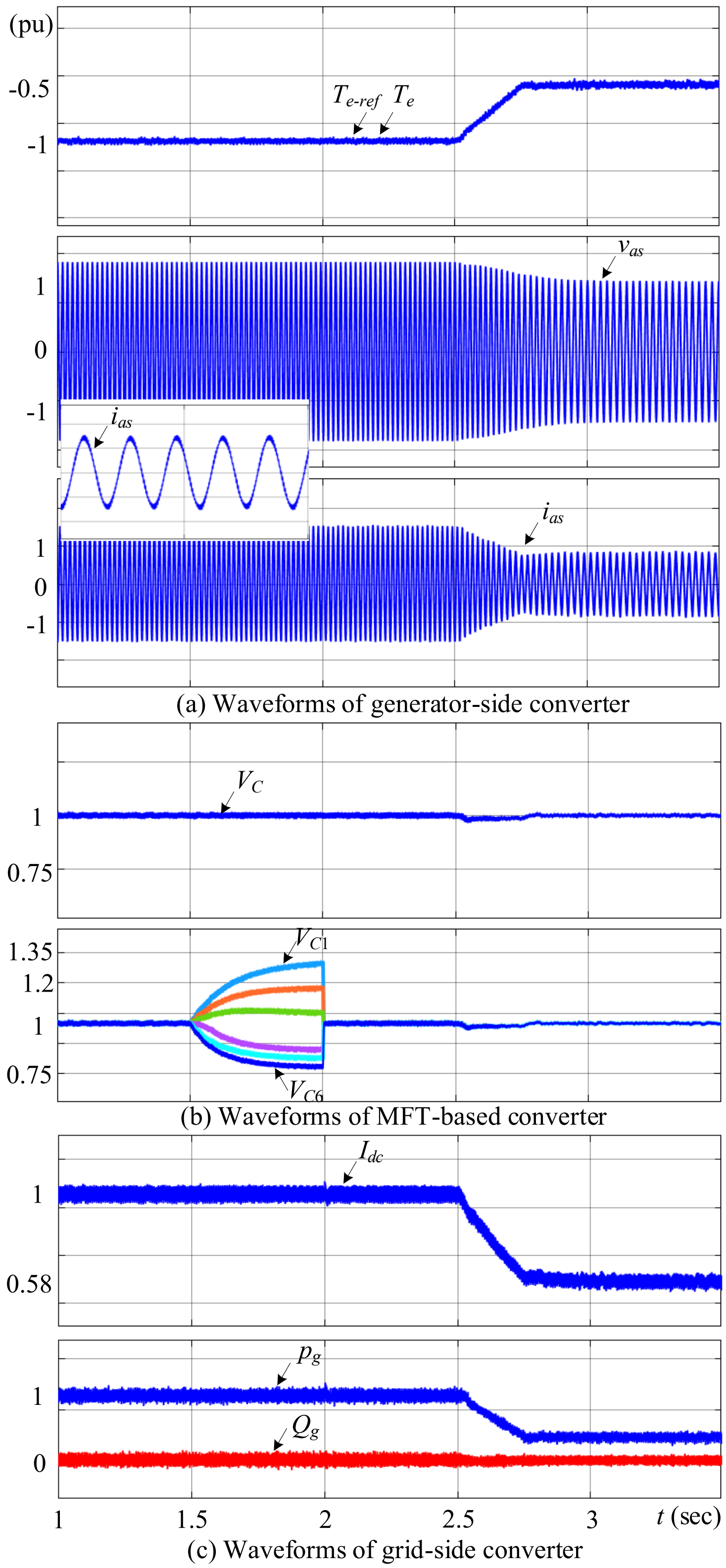

Figure 4.13: Simulated waveforms under steady and dynamic states-synchronous generator.

As previously analyzed, one of the advantages of the proposed converter is its superior performance in reducing generator stator current harmonics compared to diode rectifier-based converters. The zoomed waveform of stator current (i_{as}) depicted in Figure 4.13(a) highlights such superior harmonics performance.

At t = 1.5 sec, the voltage balancing control is deactivated. Consequently, the capacitor voltages begin to deviate due to mismatch in the transformers used. As discussed earlier, modules with higher turn ratios suffer from higher capacitor voltages. In this case, v_{c1} increases to 1.3 pu, while v_{c6} decreases to around 0.75 pu.

At t = 2 sec, the voltage balancing control is reactivated, causing the capacitor voltages to track their reference values and return to a balanced state. During this period, the generator-side controls (Figure 4.13(a)), grid-side controls (Figure 4.13(c)), and the DC voltage control of the MFT-based converter (Figure 4.13(b)) are all achieved.

At t = 2.5 sec, the generated reference torque $T_{e\text{-}ref}$ starts to decrease from -1 pu down to -0.5 pu at t = 2.75 sec, and then remains constant. With the proposed control scheme, the actual torque tracks well with the reference torque. Consequently, the generated terminal voltage (v_{as}) and current (i_{as}) at the generator side decrease accordingly. The DC voltage (V_{dc} is maintained constant under control, and the capacitor voltages are well-balanced under control. The captured real power (P_g) decreases from 1 pu to around 0.25 pu at the grid-side accordingly. The DC current (I_{dc}) tracks well with its reference $I_{dc\text{-}ref}$, which is reduced from 1 pu to around 0.58 pu to lower power loss and ensure grid-side control. The reactive power is controlled to 0, achieving unity power factor at the grid-side.

In summary, the simulated results validate the effectiveness of the proposed control scheme in achieving the defined control objectives.

Figure 4.14 depicts the simulated waveforms during the start-up of the PMSG wind system. At t = 0.1 sec, the generator torque T_e begins to increase following its reference up to its rated value at t = 0.6 sec, after which it remains constant. The rotor speed ω_m changes correspondingly, reaching the rated speed at t = 0.6 sec. The generator outputs, including the phase voltage (v_{as}) and current (i_{as}), are also illustrated in Figure 4.14. During the start-up phase, the voltage V_C of the generator-side converter is controlled to track its reference value $V_{C\text{-}ref}$, which is set in proportion to the generator rotor speed. The DC-link current I_{dc} is controlled differently during start-up. Before t = 0.6 sec, when the rotor speed has not yet reached its rated value and the captured power is low, the DC-link current reference is set to a lower value. At $t = 0.6$ sec, when the system reaches its rated conditions, the DC-link current I_{dc} starts to be controlled to follow its rated value. It's important to note that various control scenarios can be applied during start-up, and the one illustrated here serves as an example. Different strategies may be employed depending on specific system requirements and operational considerations.

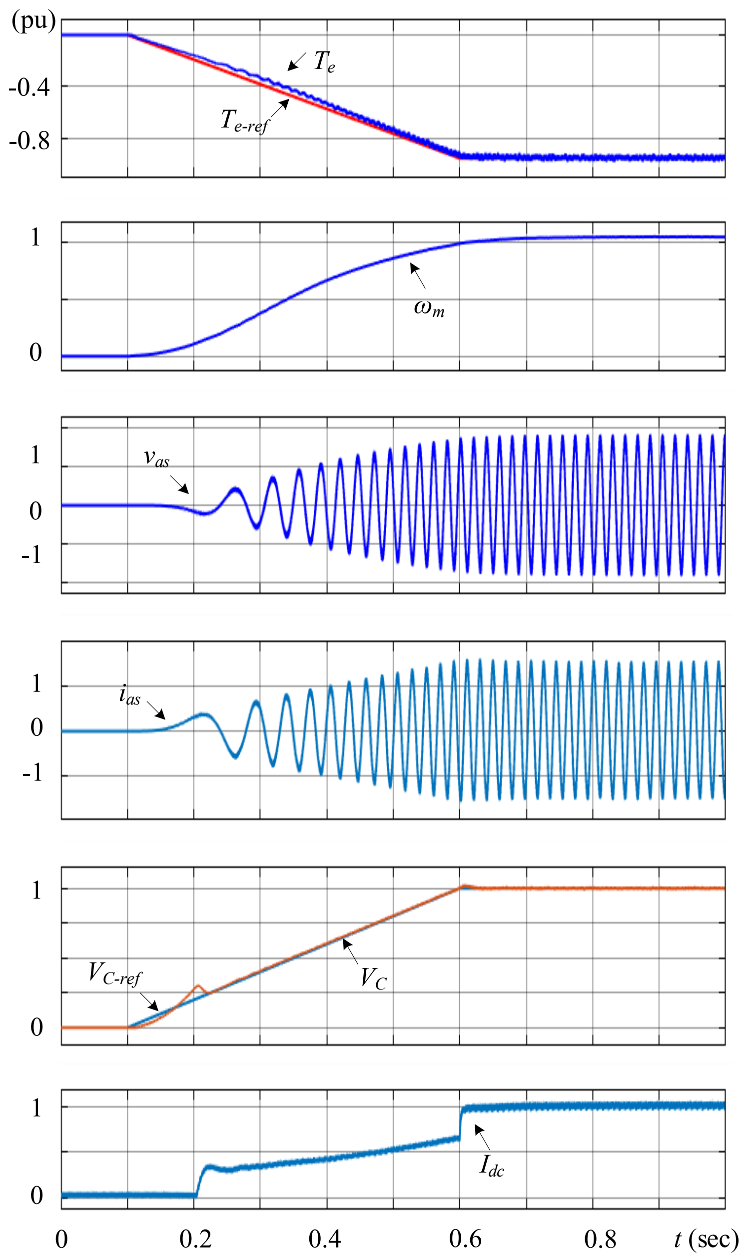

Figure 4.14: Simulated waveforms of the proposed converter during start-up.

4.4.2 Experimental results of LV converter

A downscaled setup, as depicted in Figure 4.15, has been constructed to validate the performance of the proposed converter and control system. In this setup, a variac is employed to operate the turbine-generator set, while a transformer is utilized at the grid to step up the output voltage to the grid voltage level. Additionally, an extra resistor (R_p = 600Ω) is incorporated to introduce voltage imbalance in the MFT-based converter. The parameters associated with this setup are listed in Table 4.1. The converter circuit of the setup is illustrated in Figure 4.15.

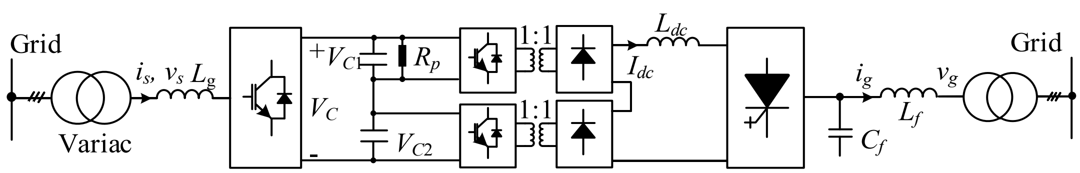

Figure 4.15: Converter circuit used for lab-scale experiments.

Figure 4.16 presents the experimental waveforms of the proposed converter under rated conditions: the generator-side voltage (vs, line-to-line voltage) is 71 V, and the grid-side voltage (vg, line-to-line voltage) is 104 V. As illustrated in the figure, the generator-side current (i_{as}, phase current) at 7.1 A is well controlled under steady-state conditions. The phase displacement between vs and i_{as} is 30 degrees, indicating unity power factor at the generator side. Additionally, both the DC voltage (V_C = 160 V) and the DC current (I_{dc} = 6.5 A) are well controlled to their respective references. Also, as shown in Figure 16 (a), the generator-side current (i_{as}) exhibits superior harmonics performance. Figure 4.16 (b) shows the steady-state waveforms of the grid voltage and grid current under the same rated conditions. As depicted, the grid voltage (v_g, line-to-line voltage) is 104 V, and the grid current (i_{ag}, phase current) at 4.3 A is achieved under unity power factor control ($Q_{g\text{-}ref}$ = 0). These results demonstrate the effectiveness of the proposed converter in achieving stable and controlled operation under steady-state conditions.

Figure 4.17 exhibits the experimental waveforms of the proposed converter under dynamic conditions. In a wind system utilizing a turbine-generator set, the generator-side voltage and current change simultaneously in response to changes in wind speed. However, due to the use of a variac in the experiments to simulate the turbine-generator set, it is not feasible to change both voltage and current simultaneously. Therefore, two separate experiments are conducted: one with a constant generator-side voltage (v_s) while the generator-side current (i_{as}) is varied, and the other with a constant generator-side current while the generator-side voltage is varied.

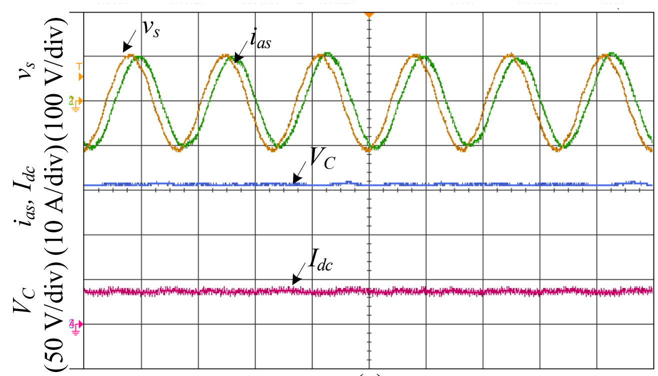

(a)

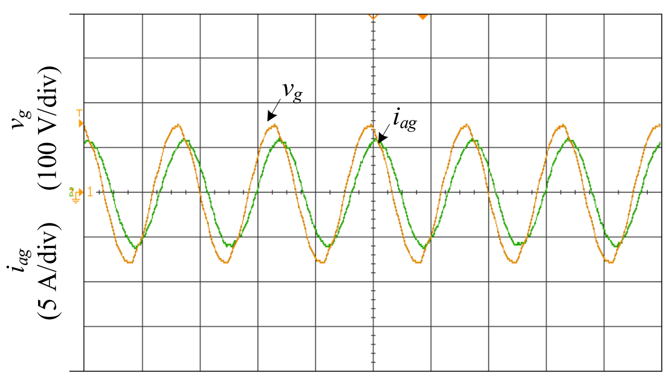

(b)

Figure 4.16: Experimental waveforms of the proposed converter under steady states.

In Figure 4.17(a), the performance under a stepped change of i_{as} is depicted, where i_{as} is controlled to step from 3.5 A to 7 A. Under such a change, the DC voltage (V_C = 160 V) is well maintained, and the DC current (I_{dc}) changes accordingly to ensure control objectives at both the generator and grid sides.

Similarly, in Figure 4.17(b), i_{as} is maintained at 7 A while v_s is increased from around 35 V to 70 V by manually adjusting the variac. The DC voltage control ensures V_C = 160 V, and the DC current control adapts to the corresponding change.

Figure 4.17(c) demonstrates the performance of the voltage balancing control under both steady-state and dynamic conditions. With the balancing control, V_{C1} = V_{C2} is ensured, while without the balancing control, a voltage deviation occurs. V_{C1} decreases while V_{C2} increases due to the introduction of the extra resistor R_p. In summary, the simulated and experimental results validate the performance of the proposed converter and control scheme effectively.

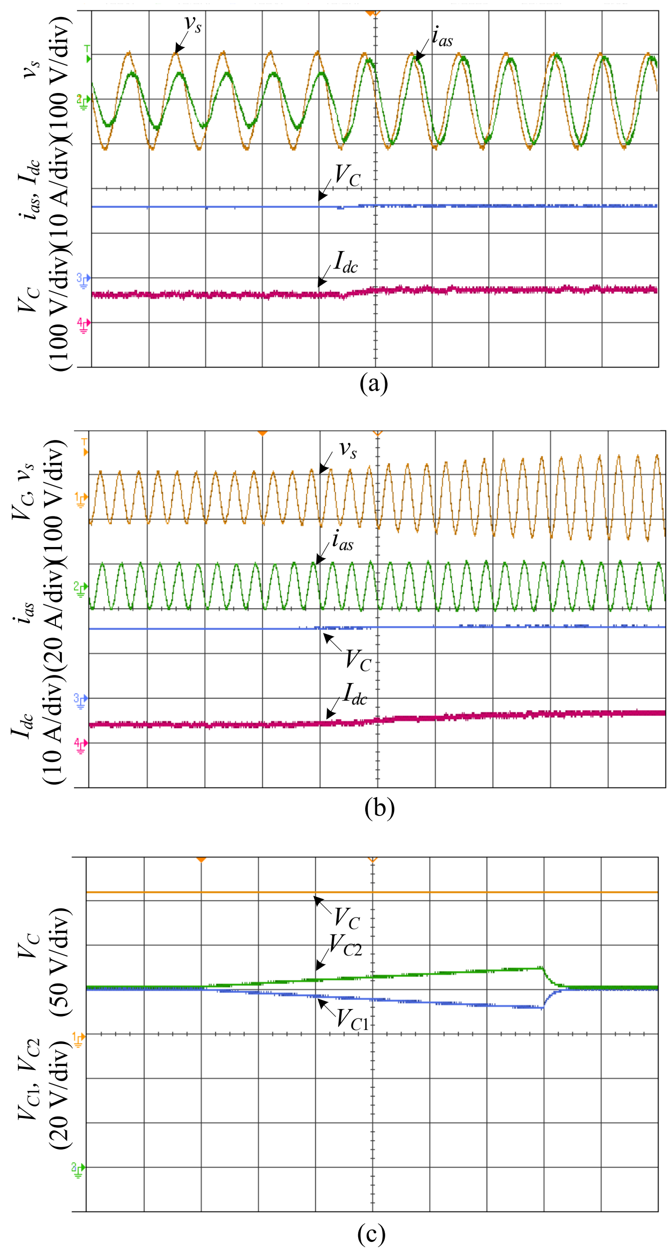

Figure 4.17: Experimental waveforms of the proposed converter under dynamic states.

4.5 Conclusions

In the realm of CSC-type series DC-based WECS, the generator-side converters can be categorized into four types: passive rectifier + LFT, passive rectifier + MFT, active rectifier + LFT, and active rectifier + MFT. While LFT technology is well-established, it tends to be bulky. In contrast, MFT technology offers a smaller size and weight, making it preferable for WECS installations where space in the nacelle is limited. Passive rectifiers are known for their low cost, high reliability, simplicity, and scalability, whereas active rectifiers provide superior performance in terms of generator stator current harmonics.

In this chapter, a hybrid converter based on the active rectifier + MFT configuration has been proposed and studied. It comprises an active rectifier and a modular MFT-based converter on the generator side, while a conventional CSC is employed on the grid side. Different versions of the proposed converter have also been developed to accommodate various generator systems with different voltage ratings. The integration of an active rectifier ensures superior harmonics performance of generator stator currents, while the use of modular MFTs contributes to size and weight reductions in the generator-side conversion system.

A hybrid control system has been devised for the proposed hybrid converter, offering the flexibility of operating in either CSC mode or VSC mode. The CSC mode retains the benefits of traditional CSC-type WECS, such as reliable short-circuit protection and variable DC-link voltage operation, while the VSC mode simplifies the control system design. To harness the advantages of both CSC and VSC modes, a hybrid control strategy comprising both CSC and VSC controls has been developed and examined.

Both simulations and experiments have been conducted to validate the performance of the proposed converter and the effectiveness of the proposed control strategies. These investigations have demonstrated the feasibility and efficacy of the hybrid converter in wind energy systems.

Chapter 5

Grid-Side Transformerless Series-Connected Current Source Converters

In CSC-type series DC-based WECS [91-96], current source converters (CSCs) are employed as the grid-side converter. These CSCs require the use of line-frequency multi-winding transformers, which are bulky and costly. In this chapter, transformerless CSCs are developed to eliminate the use of line-frequency multi-winding transformers, thereby resulting in reductions in cost and size. The chapter begins with an introduction to the proposed transformerless CSC, followed by a modulation scheme developed for the transformerless CSCs. Finally, the performance of the proposed converter and the effectiveness of the developed modulation are validated through both simulations and laboratory-scale experiments.

5.1 Existing grid-side current source converters

Figure 5.1 illustrates the existing series-connected CSCs used on the grid side of CSC-type series DC-based WECS. These CSCs are connected in series at their inputs to withstand the HVDC, while they are connected in parallel at their outputs through multi-winding transformers [51-56] [103-105] before being connected to the grid. Figure 5.2 shows an improved version of series-connected CSCs, where a smaller number of switches is needed, thanks to the specific configuration of the multi-winding transformers. Figure 5.3 shows phase-shifting transformer-based CSCs operating at a fundamental switching frequency. Operating with a fundamental switching frequency reduces switching losses but generates highly distorted currents, particularly these low-order harmonics. The use of a phase-shifting transformer, on the other hand, eliminates these low-order harmonics, enabling the CSC to operate with low switching frequencies.

The multi-winding transformers serve two functions: one mandatory and one optional. The mandatory function is to provide an independent current path for each CSC, allowing series connections at the inputs of CSCs. Additionally, they boost the output voltages of CSCs to higher values for grid connections.

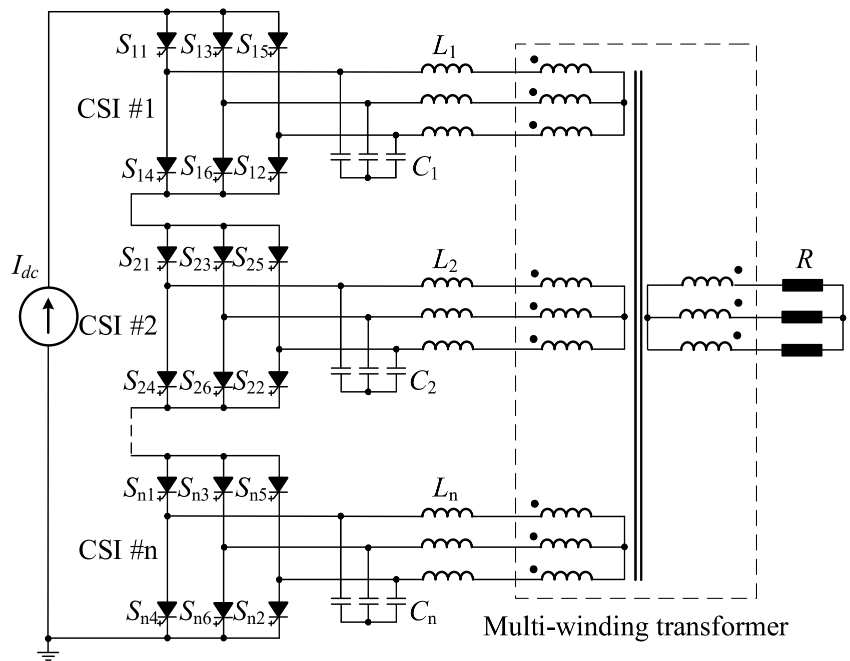

Figure 5.1: Grid-side CSCs with multi-winding transformers.

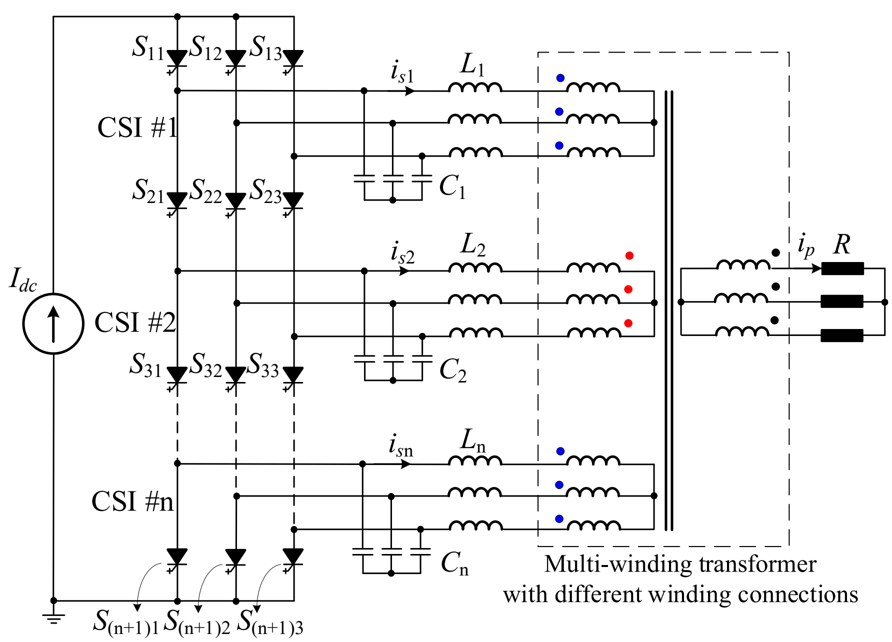

Figure 5.2: Grid-side CSCs with multi-winding transformers-modified version.

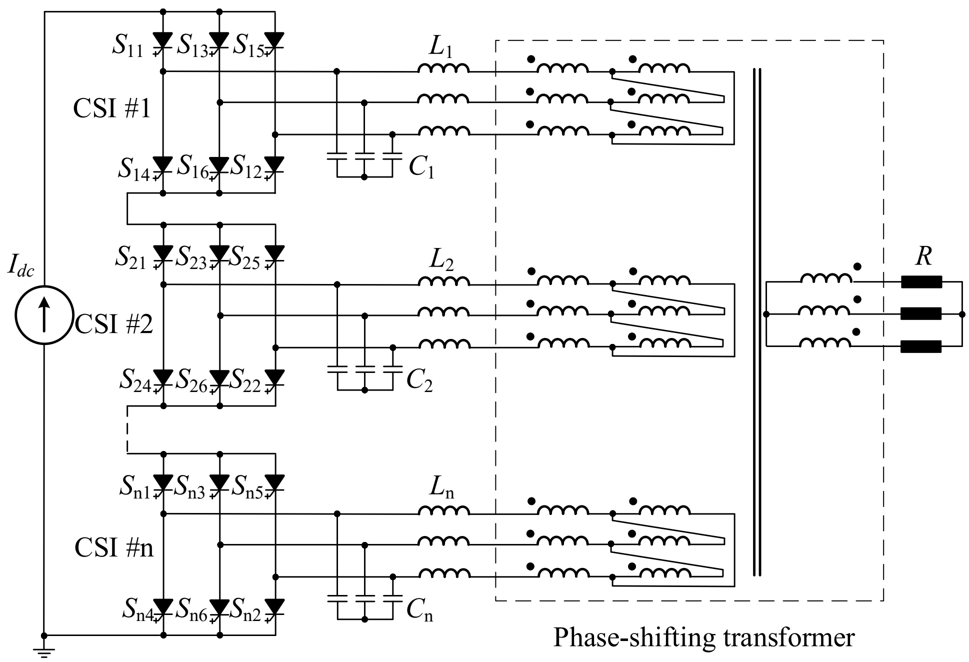

Figure 5.3: Existing grid-side CSC with phase-shifting transformers.

In summary, existing series-connected CSCs utilized on the grid side of CSC-type series DC-based WECS require the utilization of line-frequency transformers. These transformers, due to their bulkiness, high cost, and low efficiency, pose challenges to WECS.

5.2 Transformerless series-connected current source converters

Fig 5.4 shows the single-phase version of the proposed series-connected CSCs without the need for transformers, and its three-phase version is illustrated in Figure 5.5. In this chapter, the single-phase converter is studied.

As depicted in Figure 5.4, the proposed transformerless CSCs consist of n identical single-phase CSC modules. Each single-phase CSC module comprises a conventional H-bridge CSC and an additional switch S_n (where n = 1, 2…). These identical CSC modules are connected in series at both inputs and outputs without transformers. The series connection at the inputs of CSCs allows the proposed converter to withstand HVDC, while the series connection at the outputs of CSCs enables the proposed converter to establish HVAC.

The proposed converter operates in two modes: Mode 1 and Mode 2. Figure 5.6 demonstrates these modes using a 2-module converter as an example.

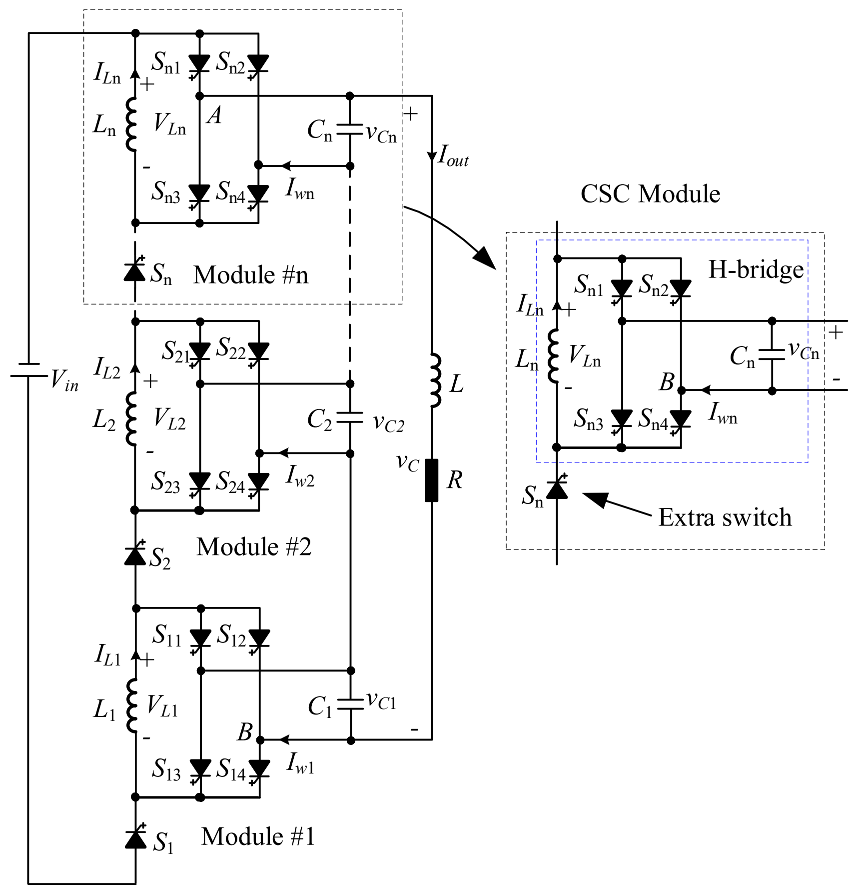

Figure 5.4: Proposed transformerless CSCs: Single-phase version.

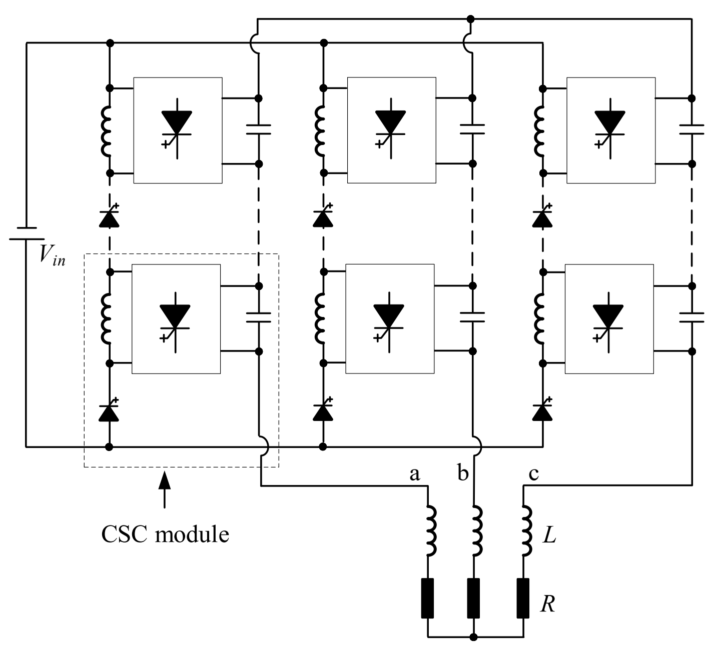

Figure 5.5: Proposed transformerless CSCs: Three-phase version.

Mode 1: In Figure 5.6, the extra switches of each CSC module (S_1 for CSC module #1 and S_2 for CSC module #2) are turned on simultaneously, while the H-bridge CSCs are off. The respective DC inductors of each CSC module (L_1 for CSC module #1 and L_2 for CSC module #2) charge in series, resulting in balanced DC inductor currents ($I_{L1} = I_{L2}$). No power is delivered to the load due to the off-state of the H-bridge CSCs.

Mode 2: The extra switches S_1 and S_n are turned off, while the H-bridge CSCs operate in a synchronous manner, delivering power to the load. The respective DC inductors of each CSC module discharge independently through the respective H-bridge CSC to the load. The output capacitors are connected in series to realize HVAC. Since each conventional H-bridge CSC has four operation modes, Mode 2 is further divided into four modes: Mode 2_1 (positive cycle), Mode 2_2 (positive cycle), Mode 2_3 (negative cycle), Mode 2_4 (negative cycle), as illustrated in Figure 5.6. Here, positive cycle refers to the positive cycle of the output PWM current i_{w1} and i_{w2} of the CSC module #1 and #2, while negative cycle refers to the negative cycle of i_{w1} and i_{w2}. For example, in Mode 2_1 (positive cycle), switches S_{11}, S_{14}, S_{21} and S_{24} are turned on, generating a positive current of $i_{w1} = I_{L1}$ and $i_{w2} = I_{L2}$, and in Mode 2_3 (negative cycle), switches S_{12}, S_{13}, S_{22} and S_{23} are turned on, resulting in a negative current of $i_{w1} = - I_{L1}$ and $i_{w2} = - I_{L2}$.

The capacitor currents for CSC module #1 and #2 are $i_{C1} = i_{w1} - i_{out}$ and $i_{C2} = i_{w2} - i_{out}$ according to KCL, where i_{C1} and i_{C2} are the capacitor currents for CSC #1 and 2, and i_{out} is the load current shared by all CSC modules. In Mode 1, balanced DC inductor currents are achieved, $I_{L1} = I_{L2}$. Under ideal conditions, balanced capacitor currents are obtained in Mode 2, $i_{C1} = i_{C2}$, leading to balanced capacitor voltages, $v_{C1} = v_{C2}$. To sum up, DC inductor currents and AC capacitor voltages are inherently achieved.

5.3 Modulation scheme

All CSC modules are identical: the switches at the same locations of CSC modules are controlled synchronously. For example, the extra switch S_1 of the CSC module #1 and the extra switch S_n of the CSC module #n are turned on and off synchronously. Switches S_{11}, S_{12}, S_{13}, and S_{14} of the CSC module #1 and their respective counterparts S_{n1}, S_{n2}, S_{n3}, and S_{n4} of the CSC module #n are also turned on and off in a synchronous manner. Following this principle, the proposed transformerless CSCs are simplified to a converter with one CSC module, as illustrated in Figure 5.7, where the input DC voltage and output AC voltage for each CSC module is remaining at V_{in}/n and v_C/n respectively.

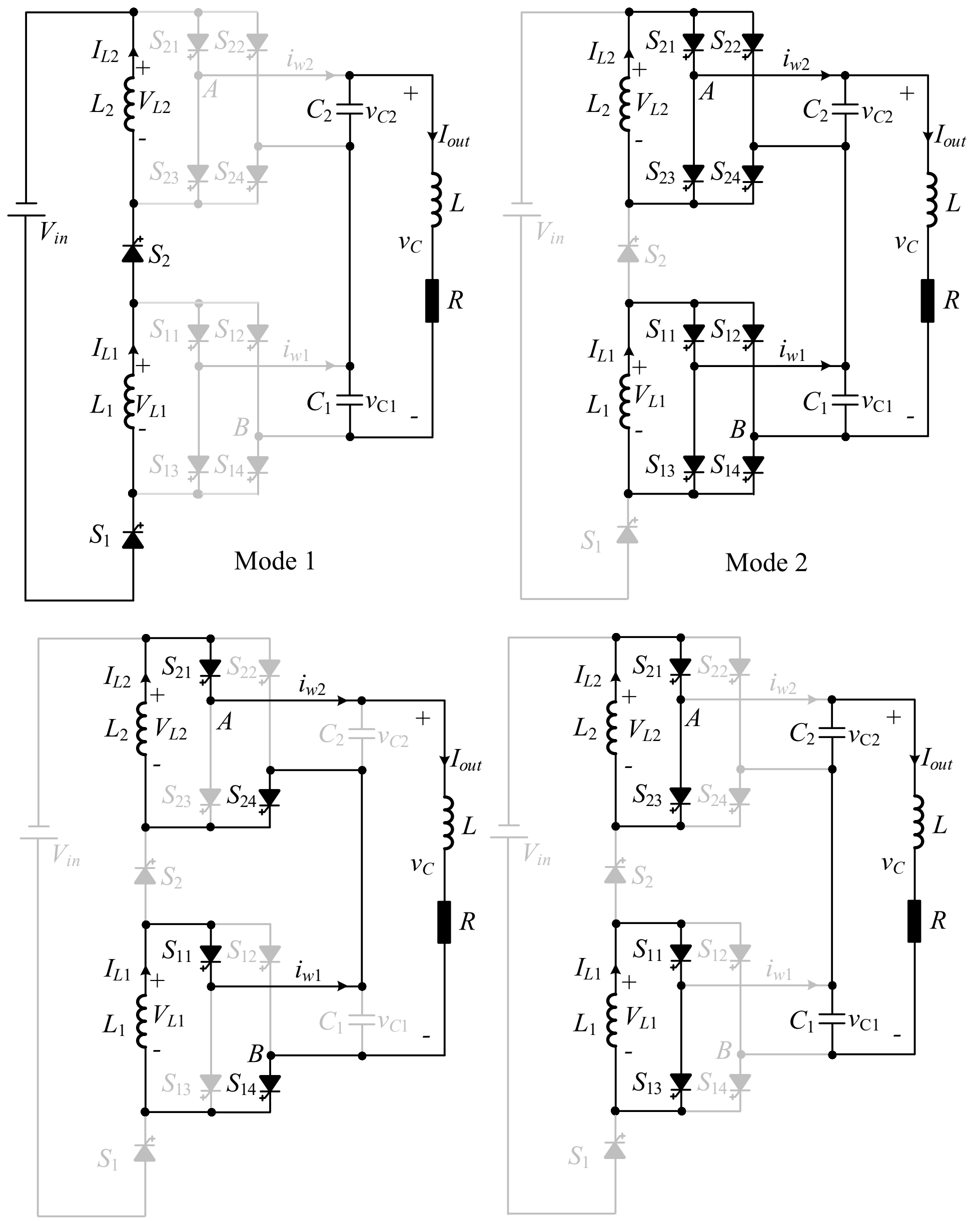

Mode 2_1(positive cycle) Mode 2_2(positive cycle)

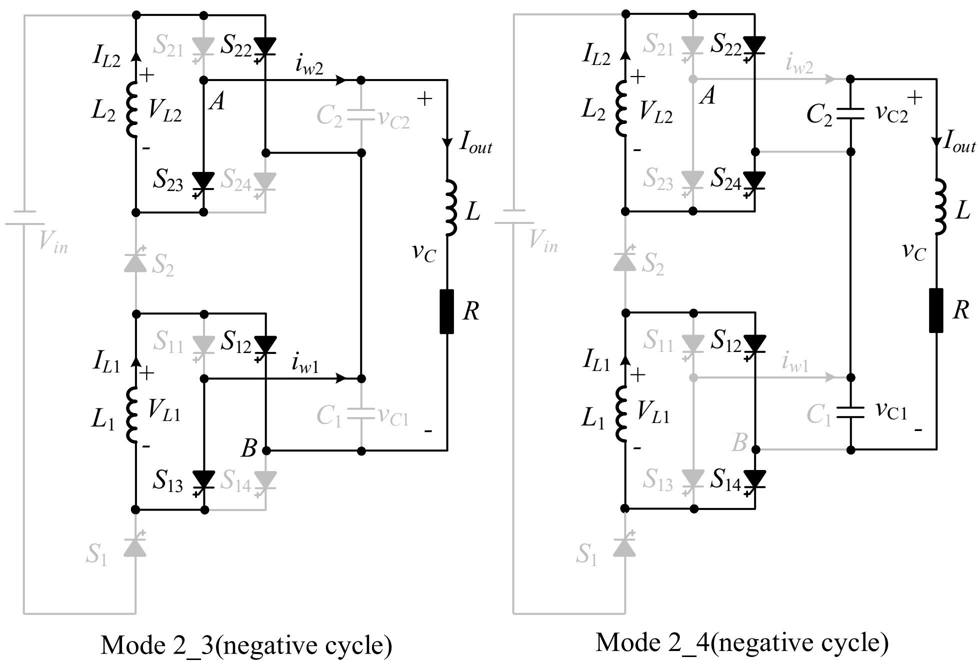

Figure 5.6: Operation modes of proposed transformerless CSCs.

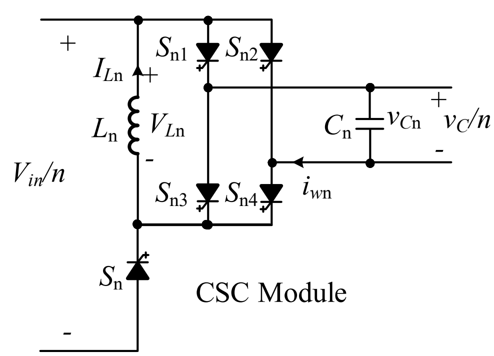

Figure 5.7: Simplified converter for modulation scheme development.

As discussed earlier, each CSC module operates at different modes, generating different output PWM currents i_{wn}. These different modes are converted to two states: active state and zero state. The active state refers to the state where $i_{wn} = I_{Ln}$ in its positive half cycle or $i_{wn} = - I_{Ln}$ in its negative half cycle, while the zero state refers to the state where $i_{wn} = 0$. The corresponding on-state switches to the active switch in each half cycle are fixed, while the zero state has two options of on-state switches. For example, in the positive half cycle, to receive an output PWM current of $i_{wn} = I_{Ln}$, S_{n1} and S_{n4} need to be turned on, while $i_{wn} = 0$ can be realized by either turning on S_{n1} and S_{n3} or turning on S_n. The different states, their corresponding on-state switches and their dwell times, and the resultant output PWM current i_{wn} are illustrated in Table 5.1.

Table 5.1: Switching states and output PWM current i_{wn}

States	On-State Switches	Dwell Time	Output PWM Current i_{wn}
Active state (positive half cycle)	S_{n1} and S_{n4}	T_1	I_{Ln}
Active state (negative half cycle)	S_{n2} and S_{n3}	T_1	$- I_{Ln}$
Zero state (positive half cycle)	S_{n1} and S_{n3}	T_{01}	0
	S_n	T_{02}	0
Zero state (negative half cycle)	S_{n2} and S_{n4}	T_{01}	0
	S_n	T_{02}	0

Figure 5.8 shows the proposed modulation. The positive half cycle of i_{wn} is taken as an example to illustrate the implementation of the proposed modulation.

The dwell time T_1 for the active state is obtained by applying the conventional SPWM. As shown in Figure 5.8, the reference wave T_1 is compared with the carrier wave, resulting in the dwell time T_1.

$$T_1 = m_a \sin(\omega t) T_s \tag{5.1}$$

where m_a is the modulation index, ω is the angular speed, and T_s is the switching period.

The dwell time for the zero state is therefore expressed as

$$T_0 = 1 - T_1 = 1 - m_a \sin(\omega t) T_s \tag{5.2}$$

As discussed earlier, the dwell time for the zero state includes two parts: T_{01} and T_{02}.

$$T_0 = T_{01} + T_{02} \tag{5.3}$$

The dwell time T_{01} is obtained by applying the voltage-second principle to the inductor L_n:

$$\begin{cases} v_{Cn}T_1 = \dfrac{V_{in}}{n}T_{01} \\ v_{Cn} = \dfrac{\sqrt{2}V_C}{n}\left|\sin(\omega t-\theta)\right| \end{cases} \rightarrow T_{01} = \frac{\sqrt{2}V_C}{V_{in}}T_1\left|\sin(\omega t-\theta)\right| \tag{5.4}$$

where θ is the phase displacement between capacitor voltage v_{Cn} and output current i_{wn}, V_C is the RMS value of the output capacitor voltage v_C. θ is obtained based on the LRC circuit.

$$\theta = \arctan\left(\frac{\omega RC_n / n}{1-\omega^2 LC_n / n}\right) - \arctan\left(\frac{\omega L}{R}\right) \tag{5.5}$$

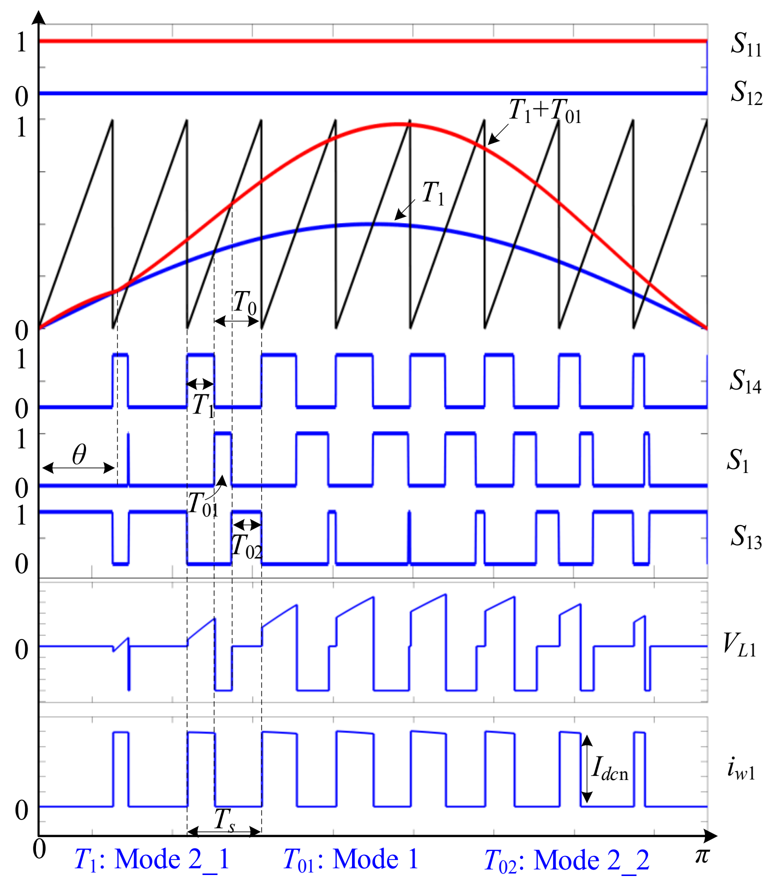

Figure 5.8: Proposed modulation: Positive half cycle of i_{w1}.

Assuming a lossless converter, the voltage gain of the proposed converter is obtained by combining (5.1), (5.2) and (5.4).

$$\frac{\sqrt{2}V_C\sin(\omega t-\theta)}{V_{in}}=\frac{k(T_s-T_1)}{T_1}\rightarrow\frac{V_C}{V_{in}}=\frac{k(1-m_a\sin(\frac{\pi}{2}+\theta))}{\sqrt{2}m_a\sin(\frac{\pi}{2}+\theta)} \tag{5.6}$$

where k is defined as $k = T_{01}/T_0$ at the time instant of $\omega t=\pi/2+\theta$, ranging from 0 to 1.

As illustrated in Equation (5.6), for a given ma, the minimum and maximum gains occur at k = 0 and k = 1, respectively. For a given k, m_a = 0 results in an infinite gain, while the minimum gain approaches zero as m_a approaches 1. This converter functions as a buck-boost converter.

The passive components of the proposed CSC, including the DC inductor and AC filter, are designed using the same procedure as the conventional CSC. The DC inductor (L_n for CSC module #n) is calculated by applying the voltage-second principle to the inductor in either Mode 1, where the inductor is charging, or Mode 2_1, where the inductor is discharging.

$$L_n=\frac{v_{Cn}T_1}{\Delta I_{Ln}} \tag{5.7}$$

where ΔI_{Ln} is the inductor current ripple, and v_{Cn} is the instantaneous value of the filter capacitor voltage of the CSC module #n.

Substituting v_{Cn} and T_1 into (5.7) results in

$$L_n=\frac{1}{\Delta I_{Ln}}\frac{\sqrt{2}v_{Cn}}{f_s}m_a\sin(\omega t)\sin(\omega t-\theta) \tag{5.8}$$

where f_s is the switching frequency.

As shown in Equation (5.8), the required DC inductor is inversely proportional to the switching frequency and proportional to the modulation index (m_a). Additionally, due to the variable dwell time (T_1) and variable voltage (v_{Cn}) in a fundamental frequency cycle, the required inductance varies within a fundamental frequency cycle. The maximum value among these different inductances is selected as the final one for CSC module #n. The design procedure for the AC filter of the proposed CSC follows that of the conventional CSC and will not be repeated here.

5.4 Simulations and experimental results

MATLAB simulations have been carried out to evaluate the performance of the proposed converter. Three CSC modules are utilized in simulation. The parameters used for simulation are listed in Table 5.2. And the converter circuit for simulation is illustrated in Figure 5.9.

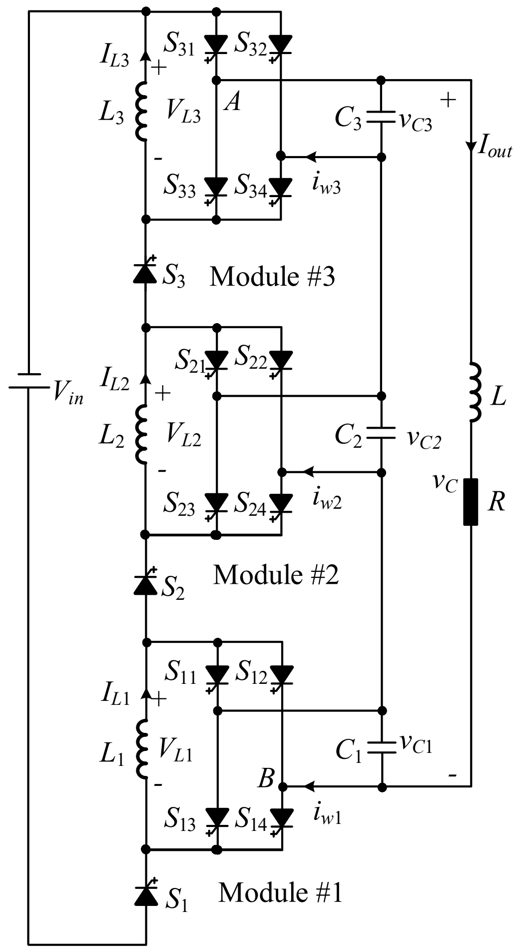

Figure 5.9: Converter circuit used for simulation.

5.4.1 Simulated results

Figure 5.10 displays the simulated gating signals of the switches of the three-module transformerless CSCs over one fundamental-frequency cycle. Switches S_{n1} and S_{n2}, situated at top of each CSC module, switch at the fundamental frequency of 60 Hz. The switching frequencies of switches S_{n3}, S_{n4}, and S_n are equal to the carrier frequency of 1080 Hz.

Table 5.2: Simulated and experiment parameters.

Parameters	Simulation	Experiment
Input DC voltage V_{in}	6000 V	120 V
Output AC voltage V_C (RMS of v_C)	4160 V	70 V
DC inductor current $I_{L\mathrm{n}}$	685 A	14 A
Load current I_{out}	240 A	5 A
Modulation index m_a	0.5	0.5
Coefficient k	0.95	0.95
Switching frequency f_{sw} ($S_{\mathrm{n}1}$, $S_{\mathrm{n}2}$)	60 Hz	60 Hz
Switching frequency f_{sw} ($S_{\mathrm{n}3}$, $S_{\mathrm{n}4}$, S_{n})	1080 Hz	1080 Hz
DC inductor L_{n}	10 mH	20 mH
AC filter capacitor C_{n}	200 µF	200 µF
AC filter inductor L_f	5 mH	5 mH
Load resistor R	17 Ω	10 Ω
Number of CSC modules n	3	2

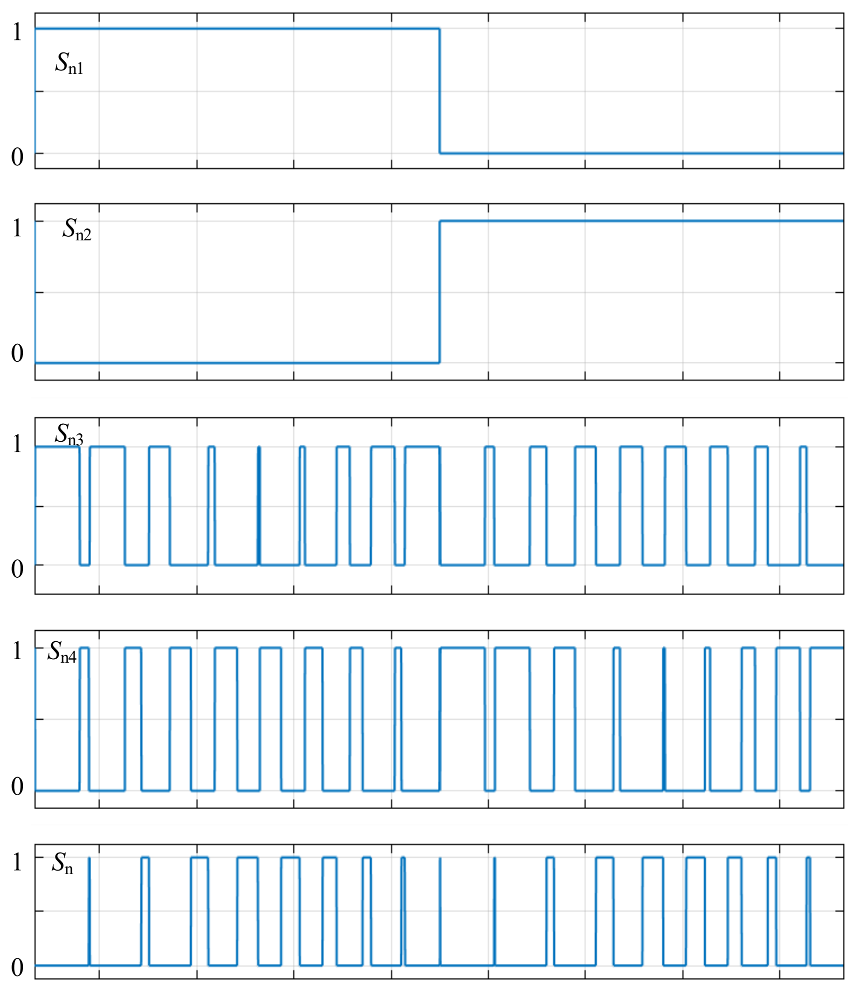

Figure 5.10: Gating signals over a fundamental-frequency cycle.

Figure 5.11 shows simulated waveforms of the proposed transformerless CSCs under both steady and dynamic states. Prior to t = 1s, the converter operates under a DC-link voltage of V_{in} = 3000 V (0.5 pu). The resultant DC inductor currents I_{L1}, I_{L2}, and I_{L3} balance around 340 A, the output AC capacitor voltages v_{C1}, v_{C2}, v_{C3} also balance at approximately 680 V, and the load current i_{out} is approximately equal to 120 A. After t = 1s, the DC-link voltage V_{in} increases to its rated value at 6000 V (1 pu). Consequently, the resultant DC inductor currents I_{L1}, I_{L2}, and I_{L3} increase to 680 A, the output AC capacitor voltages v_{C1}, v_{C2}, v_{C3} also increase to at approximately 1360 V, and the load current i_{out} increases to 240 A. In this process, DC inductor currents and AC capacitor voltages are well balanced.

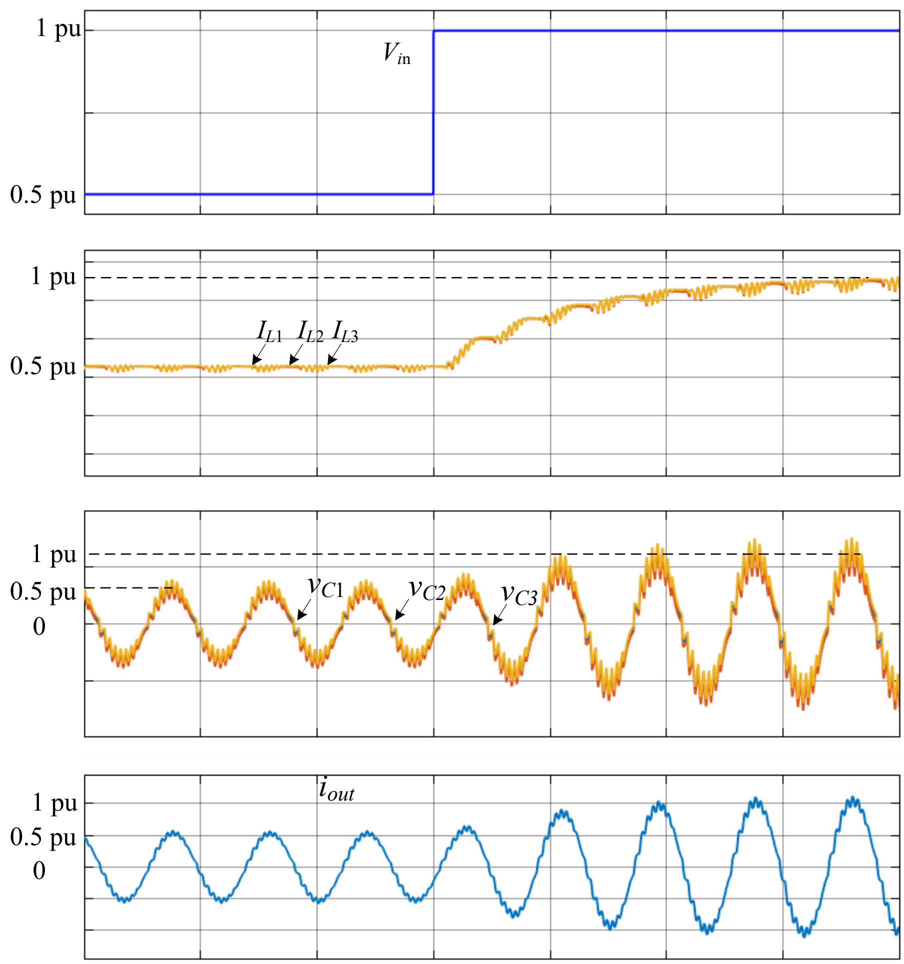

Figure 5.11: Simulated waveforms of the proposed converter under both steady and dynamic states.

5.4.2 Experiment results

A downscaled setup has been constructed to validate the performance of the proposed converter and modulation scheme. In this setup, the input DC voltage (V_{in}) is realized by using a variac and a diode rectifier. Two CSC modules are employed in the experiment setup. The parameters associated with this setup are listed in Table 5.2. The converter circuit of the experiment setup is illustrated in Figure 5.12.

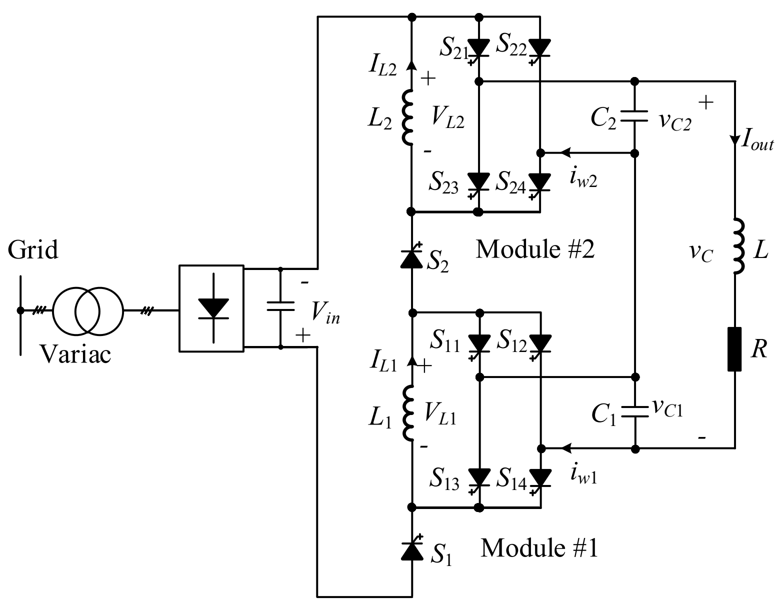

Figure 5.12: Converter circuit used for lab-scale experiments.

Figure 5.13 depicts the gating signals of the switches for the two-module transformerless CSCs over one fundamental-frequency cycle. Switches S_{n1} and S_{n2}, situated at top of each CSC module, switch at the fundamental frequency. The switching frequencies of switches S_{n3}, S_{n4}, and S_{n} are consistent and equal to the carrier frequency.

In Figure 5.14, experimental waveforms of the proposed transformerless CSCs under steady state are illustrated. When the inverter operates with V_{in} = 120 V, the DC inductor currents I_{L1} and I_{L2} balance around 14 A, and the output AC capacitor voltages v_{C1} and v_{C2} also balance at approximately 35 V. i_{w1} and i_{w2} represent the output PWM currents of the two CSC modules, while i_{out} denotes the load current.

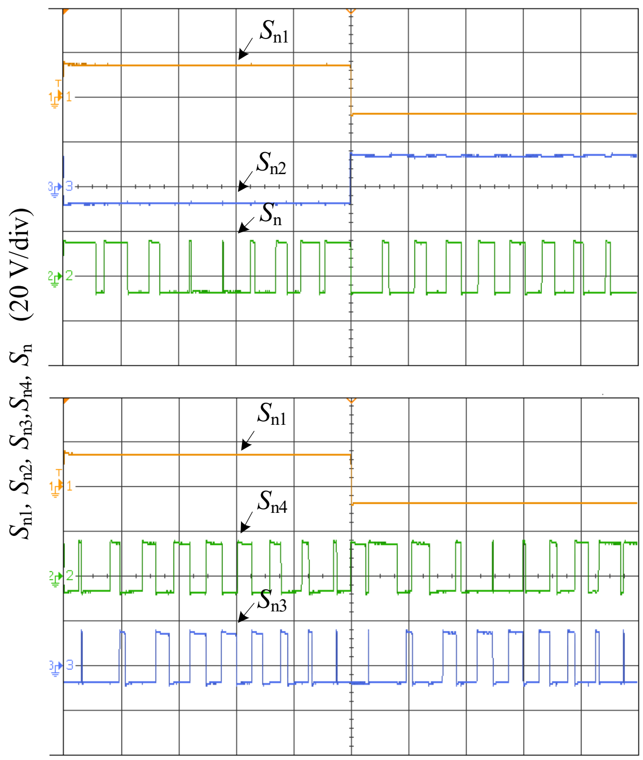

Figure 5.13: Gating signals over a fundamental-frequency cycle.

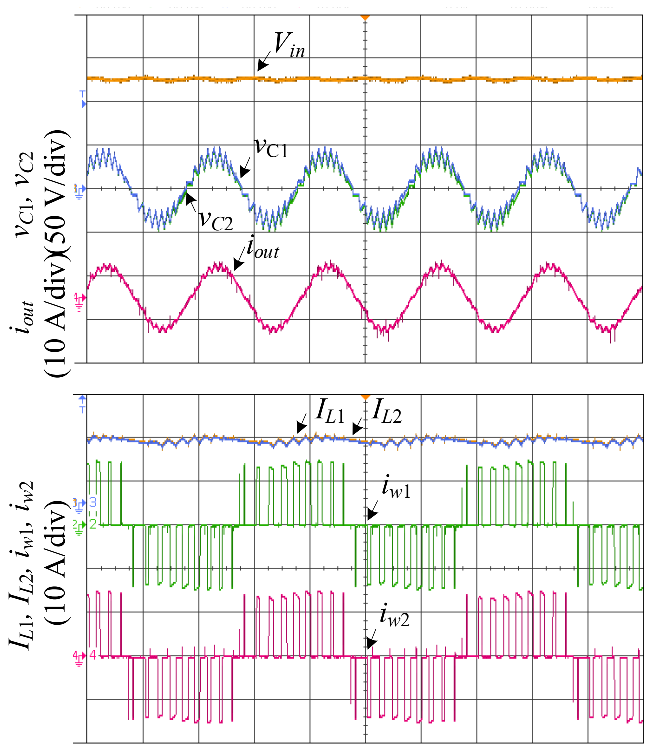

Figure 5.14: Experimental waveforms of the proposed converter under steady states.

Figure 5.15 showcases the proposed transformerless CSCs under dynamic conditions. As the input DC voltage V_{in} increases from 90 V to 120 V, the output AC capacitor voltages rise from 18 V to 35 V, and the input DC inductor currents increase from 10 A to 14 A. Throughout this transition, both DC inductor currents and AC capacitor voltages remain well balanced. In summary, the proposed inverter exhibits inherent current and voltage balancing.

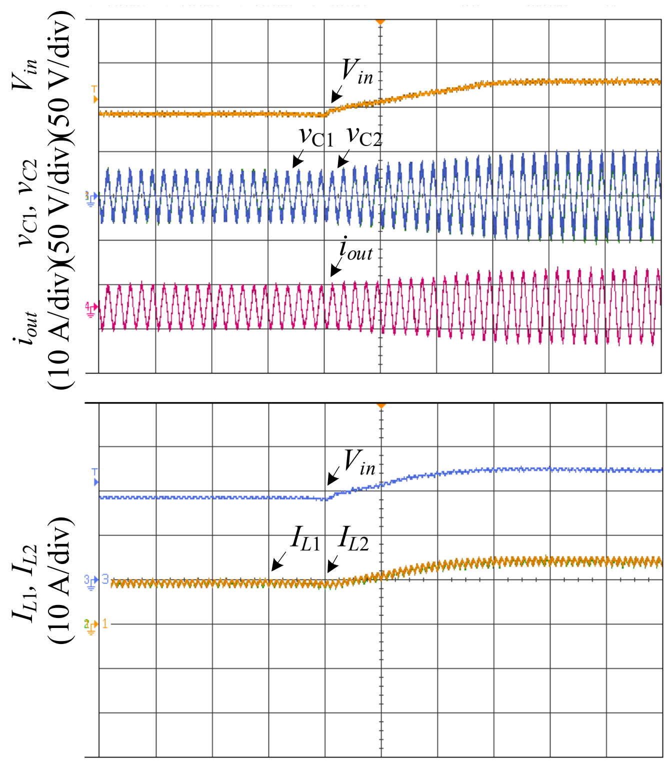

Figure 5.15: Experimental waveforms of the proposed converter under dynamic states.

5.5 Conclusions

In the domain of CSC-type series DC-based WECS, grid-side converters typically employ conventional three-phase CSC modules connected in series at their input and in parallel at their output. However, this configuration necessitates the use of line-frequency transformers to provide isolated current paths for each CSC module at the input and to boost low voltage to high voltage levels as required. These transformers, with power ratings matching that of the entire wind system, are cumbersome and expensive, posing a significant burden to WECS.

In this chapter, transformerless CSCs were introduced, eliminating the need for transformers in series-connected CSCs for the first time. This elimination yields substantial cost and size reductions. Additionally, a novel modulation scheme tailored for these transformerless CSCs was developed. This scheme enables the proposed converter to achieve buck-boost operation and inherently balance DC inductor currents and AC capacitor voltages without the need for extra balancing controls.

The operational principles of the proposed transformerless CSCs and the accompanying modulation scheme have been thoroughly investigated. Furthermore, their performance has been examined and validated through lab-scale experiments.

Chapter 6

Grid-Side Transformerless Series-Connected Current Source Converters without Series-Connected Switches

In CSC-type series DC-based WECS, conventional CSCs are typically utilized as the grid-side converter. Identical CSC modules are connected in series at the input and in parallel at the output. However, this configuration necessitates the use of bulky and costly line-frequency transformers. In the preceding chapter, transformerless CSCs were introduced and investigated. The transformerless CSCs eliminate the need for bulky and costly transformers, leading to significant reductions in the size and weight of WECS. However, the transformerless CSCs require additional switches, including one with an HVDC-level rating, which results in the necessity of series-connected switches. The operation of series-connected switches requires mandatory voltage balancing controls, which are expensive and complicated. Therefore, in this chapter, a modified version of the transformerless CSCs has been developed. This modification eliminates the need for series-connected switches while retaining all the advantages of the original transformerless CSCs. The chapter commences with an introduction to the proposed modified converter of the transformerless CSCs, along with a newly developed modulation scheme to accommodate the changes in the converter. Finally, the performance of the proposed converter and the effectiveness of the developed modulation are validated through both simulations and laboratory-scale experiments.

6.1 Transformerless series-connected current source converters

Figure 6.1 illustrates the transformerless CSCs presented in Chapter 5. The transformerless CSCs consist of *n* identical single-phase CSC modules. Each single-phase CSC module comprises a conventional H-bridge CSC and an additional switch S_n (n = 1, 2…). These CSC modules are connected in series at both inputs and outputs without transformers. The series connection at the inputs of CSCs allows the proposed converter to withstand HVDC, while the series connection at the outputs of CSCs enables the proposed converter to establish HVAC.

All CSC modules are controlled synchronously. Each CSC has two operation modes: Mode 1 and Mode 2. In Mode 1, the extra switch of each CSC module (S_n for CSC module #n) is turned on, while the H-bridge CSC is off. The DC inductor of each CSC module (L_n for CSC module #n) is charging. No power is delivered to the load due to the off-state of the H-bridge CSCs in Mode 1. In Mode 2, the extra switch S_n is turned off, while the H-bridge CSC operates and delivers power to the load. The DC inductor of each CSC module is discharging through the H-bridge CSC to the load. Since each conventional H-bridge CSC has four operation modes, Mode 2 is further divided into four modes: Mode 2_1 (positive cycle), Mode 2_2 (positive cycle), Mode 2_3 (negative cycle), Mode 2_4 (negative cycle). Here, positive cycle refers to the positive cycle of the output PWM current i_{wn} of the CSC module #n, while negative cycle refers to the negative cycle of i_{wn}. For example, in Mode 2_1 (positive cycle), switches S_{1n} and S_{4n} are turned on, generating a positive current of $i_{wn} = I_{Ln}$, and in Mode 2_3 (negative cycle), switches S_{2n} and S_{3n} are turned on, resulting in a negative current of $i_{wn} = - I_{Ln}$.

One challenge posed by transformerless CSCs is that the additional switch S_1 experiences high voltage stress and is implemented using series-connected switches. It's important to note that the extra switches S_2, S_3… S_n do not encounter such issues.

The voltage stress (v_s) of S_1 under different operation modes is detailed in Table 6.1. The maximum value of v_s occurs in Mode 2_1 ($S_{11} = S_{14} = S_{n1} = S_{n4} =$ ON), where v_s is equal to $V_{in} + v_C$. Here, v_C represents the instantaneous value of the output voltage of the transformerless CSCs. The equivalent circuit of transformerless CSCs under Mode 2_1 is shown in Figure 6.2. Figure 6.3 illustrates the waveform of v_s over one fundamental-frequency cycle. As shown, v_s reaches its peak value: $v_s = V_{in} + v_{C\text{-}peak}$ in Mode 2_1. $v_{C\text{-}peak}$ denotes the positive peak value of v_C. The selection of switch S_n is based on its maximum value, necessitating the utilization of series-connected switches.

For instance, considering a converter with n CSC modules and a voltage gain of 1 ($V_{in} = v_{C\text{-}peak}$), the maximum voltage stress for S_{13} is $v_{C\text{-}peak}/n$, whereas it is $2v_{C\text{-}peak}$ for S_1. If a switch with the same voltage rating as S_{13} is selected, it would necessitate the use of $2n$ switches connected in series to achieve the equivalent of S_1. The voltage balancing of series-connected switches poses a challenge, requiring complex balancing schemes.

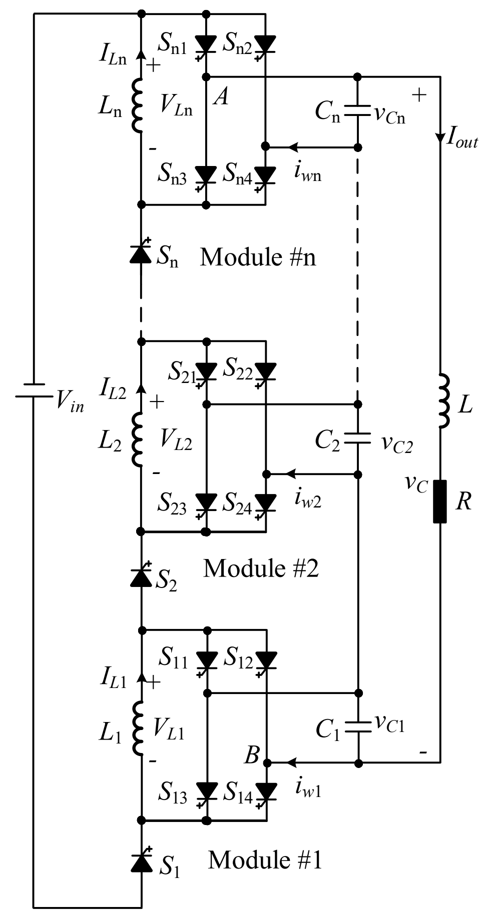

Figure 6.1: Transformerless CSCs.

Table 6.1: Voltage stress of S_1

Modes		On-state switches	Voltage stress of S_1
Mode 1		S_1, S_n	$v_s = 0$
Mode 2	Mode 2_1	S_{11}, S_{14}, S_{n1}, S_{n4}	$v_s = V_{in} + v_C$
	Mode 2_2	S_{11}, S_{13}, S_{n1}, S_{n3}	$v_s = V_{in} + v_C(\text{n-1})/\text{n}$
	Mode 2_3	S_{11}, S_{13}, S_{n2}, S_{n3}	$v_s = V_{in}$
	Mode 2_4	S_{12}, S_{14}, S_{n2}, S_{n4}	$v_s = V_{in} + v_C(\text{n-1})/\text{n}$

In summary, while transformerless CSCs eliminate the need for line-frequency transformers, they do require the utilization of series-connected switches to realize S_1. However, the use of series-connected switches introduces voltage imbalance issues, presenting a significant challenge to the system. To tackle this challenge, a modified converter is proposed and will be discussed in this chapter.

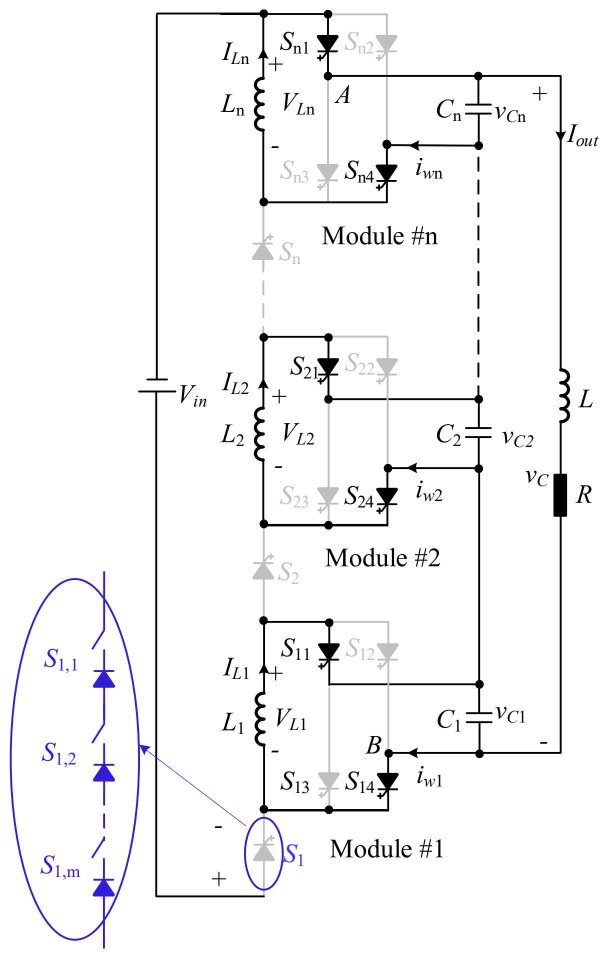

Figure 6.2 Equivalent circuit of transformerless CSCs under Mode 2_1.

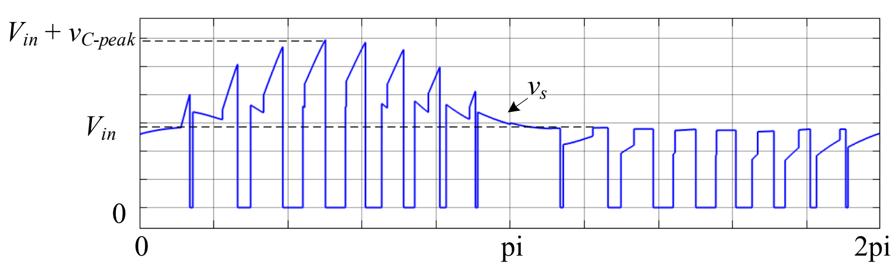

Figure 6.3 Voltage stress of S_1 over one fundamental-frequency cycle.

6.2 Transformerless series-connected current source converters without series-connected switches

Figure 6.4 shows the modified transformerless CSCs without the need for series-connected switches. In the original converter, as shown in Figure 6.2, *m* switches connected in series are needed to realize the switch S_1. In the proposed modification depicted in Figure 6.4, these m switches are replaced with (m-1) half-bridge converters and one switch $S_{1\text{-m}}$. The (m-1) half-bridge converters function as the (m-1) switches in the original converter. The remaining circuits of the modified converter remain the same as the original converter. If the switch with the same voltage rating as S_{13} is selected for these series-connected switches, then m equals to 2n.

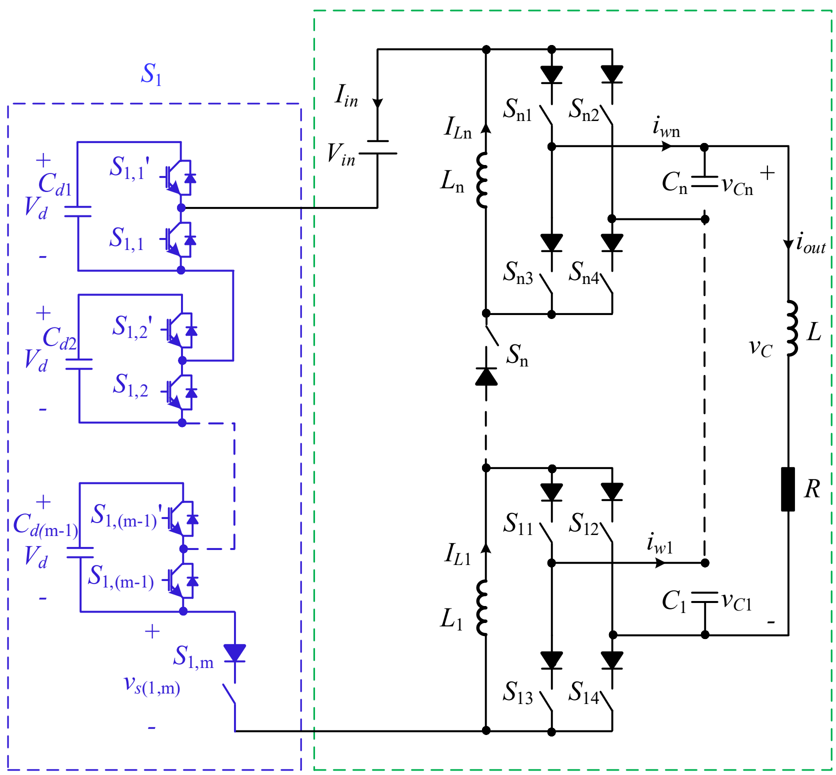

Figure 6.4 Proposed modified transformerless CSCs without series-connected switches.

6.2.1 Operation principles

As discussed earlier, the modified converter differs from the original in that the additional switch (S_1) for the #1 CSC module in the original converter is replaced by m-1 half-bridge converters connected in series with one switch, $S_{1,m}$, in the modified converter. The remaining circuitry of the modified converter is identical to that of the original. The (m-1) half-bridge converters and the switch $S_{1,m}$ operate on the same principle as their counterparts, the m series-connected switches in the original converter. Additionally, the remaining circuitry of the proposed converter functions the same as that of the original. Consequently, the modified converter, depicted in Figure 6.4, shares the same operational principles as the original converter shown in Figure 6.2, encompassing two operational modes: Mode 1 and Mode 2.

Mode 1: In the same manner as the original converter, all H-bridge converters are off, while the additional switches of all CSC modules are on. Specifically, S_2, S_{n-1} and S_n correspond to the additional switches of CSC modules #2, #(n-1), and #n, respectively. Additionally, the switch $S_{1,m}$, which serves as the extra switch of the #1 CSC module, is also turned on. All the half-bridge converters are turned off (bypass operation) by turning on the respective bottom switches: $S_{1,1}$ for half-bridge converter #1, $S_{1,2}$ for half-bridge converter #2, and $S_{1,(m-1)}$ for half-bridge converter #(m-1). DC inductors are charging in series in this mode, resulting in balanced inductor currents ($I_{L1} = I_{Ln}$). The equivalent circuit of the modified converter in this mode is shown in Figure 6.5. Shown in the figure, the equivalent circuit of the modified converter is the same as the original converter that the ON-state switches are providing path for DC inductor charging current.

Mode 2: The same as the original converter, H-bridge converters are on, while the extra switches of all CSC modules are off. Specifically, switches S_2 (CSC#2), S_{n-1} (CSC #(n-1)), S_n (CSC #n) and the switch $S_{1,m}$ (CSC #1) are turned off. It is important to note that rather than turning off all half-bridge converters, some of half-bridge converters are selected to be on, while the remaining half-bridge converters are turned off. By doing so, the voltage stress of the switch $S_{1,m}$ is reduced and the use of a single switch for $S_{1,m}$ is allowed.

For example, as shown in the equivalent circuit of the converter in Figure 6.5, two half-bridge converters are turned on by turning on their respective top switches, and the other half-bridge converters are bypassed by turning on their bottom switch. The resultant voltage stress of the switch $S_{1,m}$ for the #1 CSC module is now reduced from v_s to v_s - $2V_d$. V_d is the input voltage of each half-bridge converter. The voltage stress of off-state switches of the half-bridge converters is clamped by the input voltage V_d.

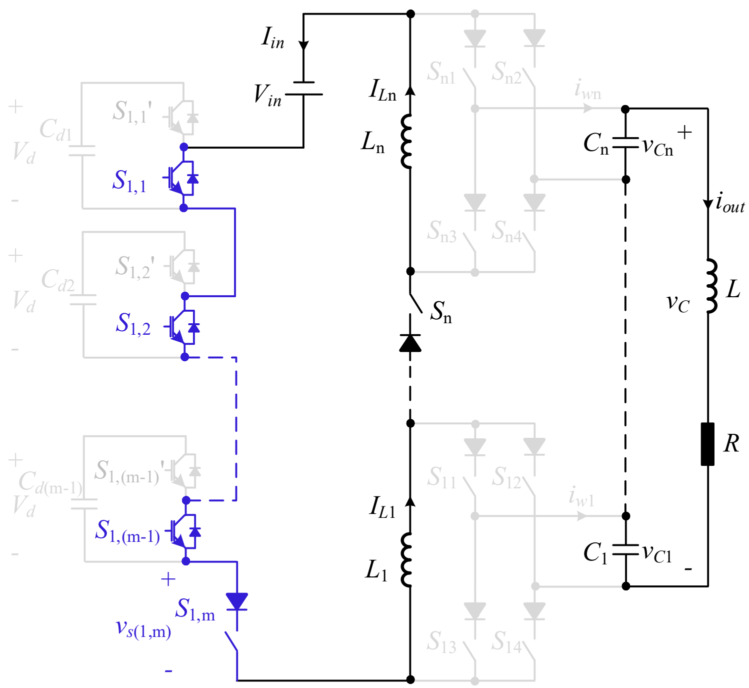

Mode 1

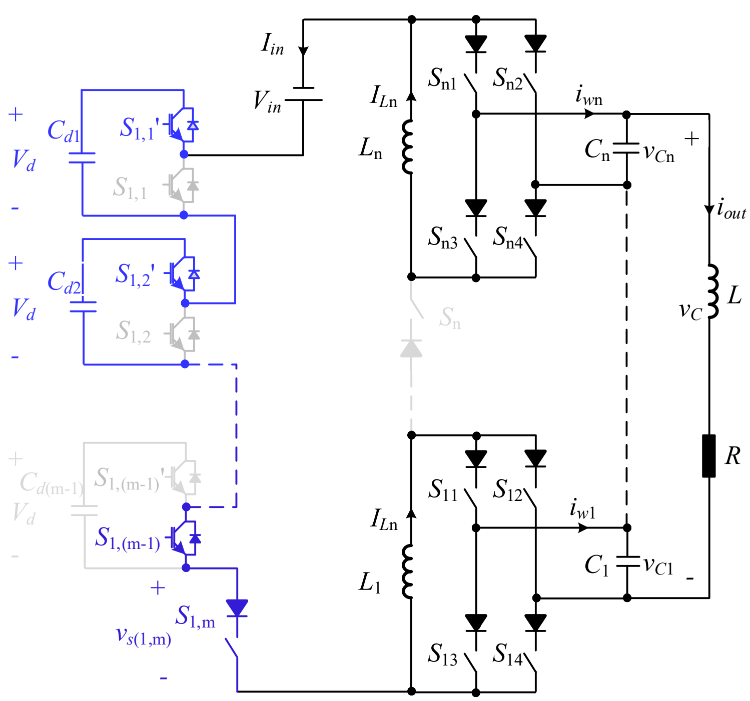

Mode 2

Figure 6.5 Equivalent circuits of the modified converter under Mode 1 and Mode 2.

As a general case where the number of bypassed H-bridge converters is h, the voltage stress of the switch $S_{1,m}$ for the #1 CSC module is reduced to:

$$v_s' = v_s - hV_d \tag{6.1}$$

where v_s' is the voltage across the extra switch $S_{1,m}$ of the #1 CSC in the modified converter, v_s is the instantaneous voltage across the extra switch S_1 of the #1 CSC in the original converter, and h is the number of ON-state half-bridge converters. ON-state half-bridge converters are converters with an output voltage of V_d, while OFF-state half-bridge converters are converters with an output voltage of zero.

When $m = 2n$, the required input voltage of each half-bridge converter V_d is expressed as

$$V_d = \frac{V_{in} + v_{C-peak}}{2n} \tag{6.2}$$

where V_{in} is the DC-link voltage of the system.

The number of ON-state half-bridge converters is determined in such a way that the voltage across the switch $S_{1,m}$ of the #1 CSC module falls into the operating range of the selected single switch $S_{1,m}$ under all the operation modes as listed in Table 6.1. If a switch with the same voltage rating as S_{13} is selected for $S_{1,m}$, the number of ON-state half-bridge submodules h is selected following the criteria shown below.

$$\left| v_s - hV_d \right| \le v_{S13} = v_{C-peak} / n \tag{6.3}$$

where v_{S13} is the maximum voltage stress of the switch S_{13}, being equal to v_{C-peak}/n.

Rearranging (6.2) generates the required number of ON-state half-bridge converters.

$$h = \frac{v_s - v_{C-peak} / n}{V_d} \tag{6.4}$$

where v_s listed in Table 6.1 is the instantaneous voltage across the extra switch S_1 of the #1 CSC in the original converter.

Substituting (6.3) into Table 6.1 results in Table 6.2, where different numbers of ON-state half-bridge converters are needed in different modes of a fundamental-frequency cycle. As shown in Table 6.2, since v_s is variable in a fundamental-frequency cycle, different number of ON-state half-bridge converters are needed to reduce the voltage stress of the switch $S_{1,2n}$ of the #1 CSC to allow the use of a single switch for this switch in Mode 2. In other words, not all half-bridge converters are always involved in a fundamental-frequency cycle and in the full operation range. Only a portion of half-bridge converters are turned on in Mode 2, resulting in a reduced average switching frequency compared with their counterparts of the original converter where all series-connected switches are switched on and off simultaneously in all modes of a fundamental-frequency cycle. Reduced switching frequencies contribute to reduced switching losses.

Substituting (6.3) into Table 6.1 yields Table 6.2, indicating varying numbers of ON-state half-bridge converters required in different modes of a fundamental-frequency cycle. As shown in Table 6.2, due to the variable nature of v_s in a fundamental-frequency cycle, a different number of ON-state half-bridge converters is necessary to reduce voltage stress on switch $S_{n\text{-}2n}$ of the n^{th} CSC module, enabling the use of a single switch for this switch $S_{1,2n}$. In essence, not all half-bridge converters are consistently involved throughout a fundamental-frequency cycle or across the entire operational range. Only a portion of half-bridge converters is activated in Mode 2, resulting in a reduced average switching frequency compared to their counterparts in the original converter, where all series-connected switches are involved simultaneously in all modes of a fundamental-frequency cycle. The reduction in switching frequencies contributes to reduced switching losses.

Table 6.2: Selection of ON-state half-bridge converters

Modes		Voltage stress of S_1	Number of ON-state half-bridge converters, h
Mode 1		$v_s = 0$	0
Mode 2	Mode 2_1	$v_s = V_{in} + v_C$	$h = \dfrac{v_s - v_{C-peak}/n}{V_d}$
	Mode 2_2	$v_s = V_{in} + v_C(n-1)/n$	
	Mode 2_3	$v_s = V_{in}$	
	Mode 2_4	$v_s = V_{in} + v_C(n-1)/n$	

6.2.2 Realization of half-bridge converters

The half-bridge converters possess a unique feature: zero-load operation. As illustrated in Figure 6.5, in Mode 1, all half-bridge converters are bypassed with an output voltage of zero. Meanwhile, in Mode 2, regardless of the state of the half-bridge converter, all have an output current of zero. In both operation modes, the output power of each half-bridge converter is zero.

This zero-load feature offers flexibility in realizing half-bridge converters, leading to smaller component sizes. For instance, the input DC voltage of each half-bridge converter can be achieved using conventional DC capacitors. These capacitors are supplied by passive rectifiers powered by grid-connected isolated transformers. Thanks to the zero-load operation, very small capacitors with just a few microfarads are sufficient. In addition, the VA ratings of isolated transformers and switches are small, with no significant burdens introduced to the system. An example of the half-bridge converter realization is depicted in Figure 6.6.

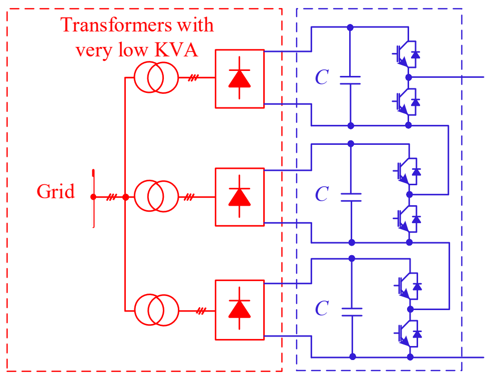

Figure 6.6: An example of half-bridge converter realization.

6.2.3 Modulation of modified converter

The modulation of the modified transformerless CSCs remains the same as that of the original converter, except for that of the half-bridge converters. Figure 6.7 illustrates the implementation of the modulation scheme, where the modulation scheme of the original converter presented in Chapter 5 is entirely inherited. In Mode 1, the bottom switches of the half-bridge converters and the respective extra switches of CSC modules are on, while the H-bridge converters are off. In Mode 2, the H-bridge converters are on, while the extra switches of CSC modules are off. Among the total of 2n-1 half-bridge converters, *h* half-bridge converters are on, while the remaining half-bridge converters are off. Consequently, the top switches of these ON-state half-bridge converters are turned on, and the bottom switches of these OFF-state half-bridge converters are turned on. The dwell times of these ON-state switches in Mode 1 and Mode 2 of the modified converter are the same as those of the original converter.

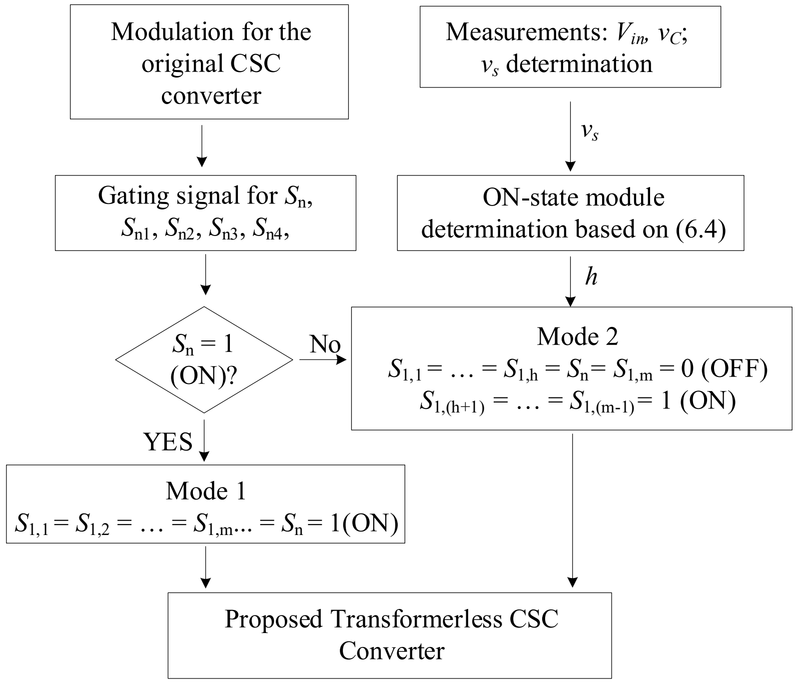

Figure 6.7: Modulation of the modified converter.

6.2.4 Comparisons and discussions

The original transformerless CSCs require the use of series-connected switches, necessitating expensive and complicated voltage balancing schemes. However, the modified converter in this chapter eliminates the need for series-connected switches, thus eliminating the use of complex and expensive voltage balancing schemes.

The elimination of series-connected switches is achieved by using cascaded half-bridge converters, which require more switches and extra components, including isolated transformer-based charging systems. Nonetheless, thanks to the zero-load operation of the half-bridge converters, the VA ratings of isolated transformers and switches remain very small, with no significant burdens introduced to the system.

Furthermore, unlike the original converter, where the series-connected switches maintain the same constant switching frequency throughout the full operation range, the modified converter achieves reduced switching frequencies due to its unique operation in Mode 2. In Mode 2, rather than turning off all half-bridge converters, only a portion of them is selected to be turned off according to a variable voltage in the full operation range, resulting in a reduced average switching frequency. These reduced switching frequencies contribute to reduced switching losses.

It is also worth noting that the cascaded half-bridge converters used in the modified converter differ from those found in MMC and CHB converters [8] . Instead of generating AC voltages, they are designed to provide variable DC voltages to reduce the voltage stress of the switch $S_{1,m}$, enabling the use of a single switch for $S_{1,m}$. Additionally, they feature a variable switching frequency, which contributes to fewer switches and reduced switching losses. Moreover, they are characterized by a unique zero-load feature, allowing the use of components with small ratings.

6.3 Simulation and experimental results

The circuit used for simulations is depicted in Figure 6.8, with the parameters listed in Table 6.3. The simulation employs two CSC modules and three half-bridge converters. Vin is realized using a three-phase variac, while capacitor charging of the half-bridge converters is facilitated by three single-phase transformers.

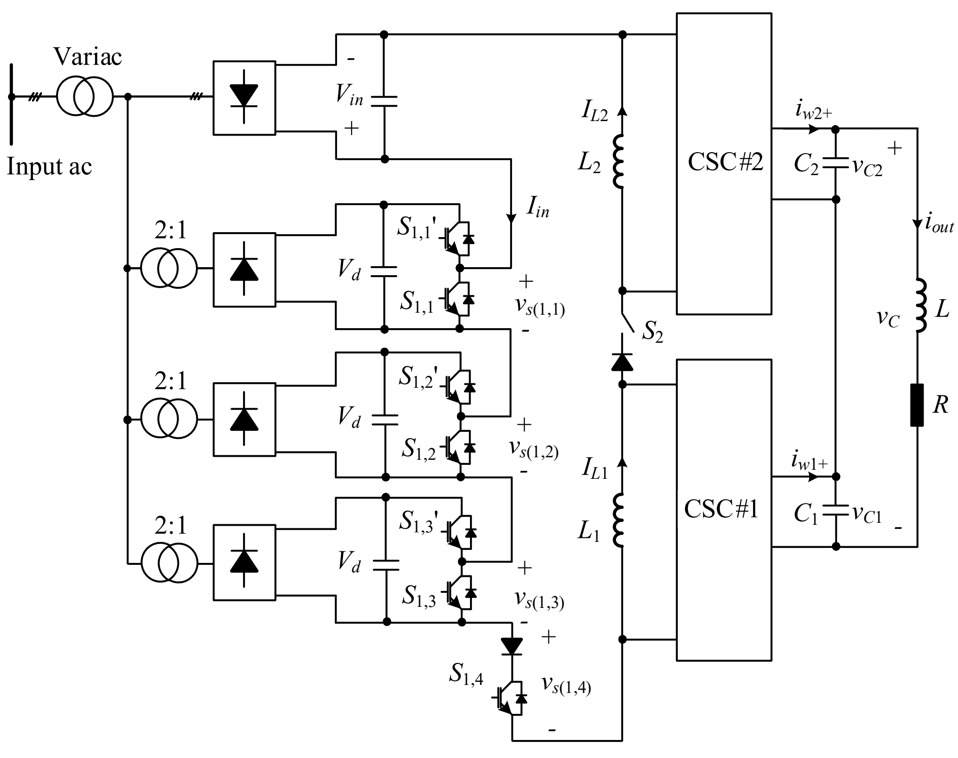

Figure 6.8: Converter circuit used for simulation.

Table 6.3: Simulation and experimental parameters

Parameters	Simulation	Experiment
V_{in}	5882 V	120 V
V_C (RMS of v_C)	4160 V	70 V
$I_{L1} = I_{L2}$	400 A	14 A
I_{out}	140 A	5 A
f_s (S_{11}, S_{12}, S_{21}, S_{22})	60 Hz	60 Hz
f_s (S_{13}, S_{14}, S_{23}, S_{24}, S_2, $S_{1,4}$)	1080 Hz	1080 Hz
f_s ($S_{1,1}$)	≤1080 Hz	≤1080 Hz
f_s ($S_{1,2}$)	≤1080 Hz	≤1080 Hz
f_s ($S_{1,3}$)	≤420 Hz	≤420 Hz
L	5 mH	5 mH
R	17.3 Ω	10 Ω

6.3.1 Simulation results

Figure 6.9 shows the simulated waveforms of the modified converter under steady and dynamic states. Before t = 1.6s, the converter is operating with rated conditions where both input voltage V_{in} and output voltage v_C are 1 pu. At t = 1.6s, V_{in} is decreased to 0.5 pu, and v_C is reduced to 0.5 pu accordingly. As shown in the figure, under both steady and dynamic states, the inductor currents ($I_{L1} = I_{L2}$) and the output capacitor voltages ($v_{C1} = v_{C2}$) are all well balanced without extra balancing controls. The results well agree with the previous analysis that inherent current balancing and voltage balancing of the original converter are retained.

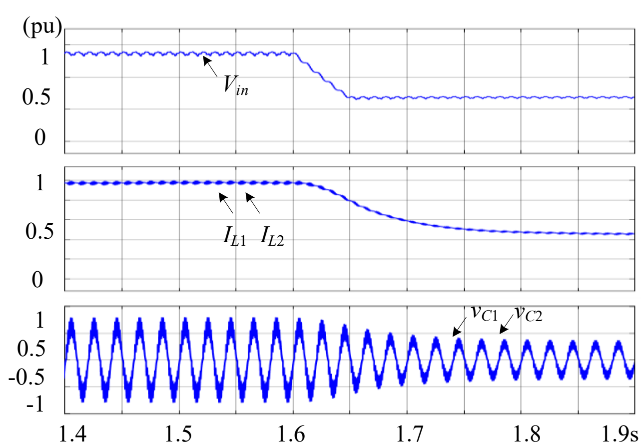

Figure 6.9: Simulated waveforms of the modified converter under both steady and dynamic states.

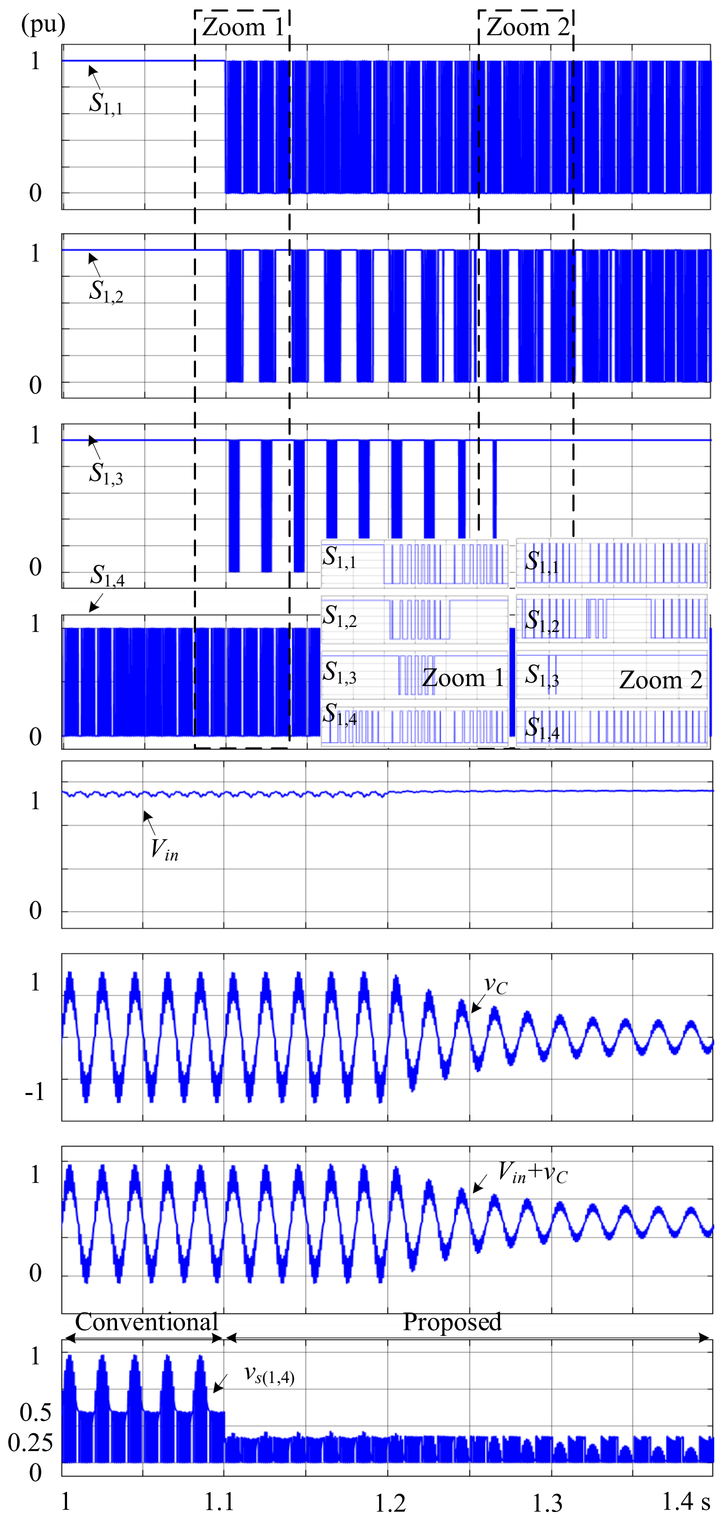

Figure 6.10: Simulated waveforms of the modified converter under different conditions: With and without the half-bridge converters; And with a change in output voltage.

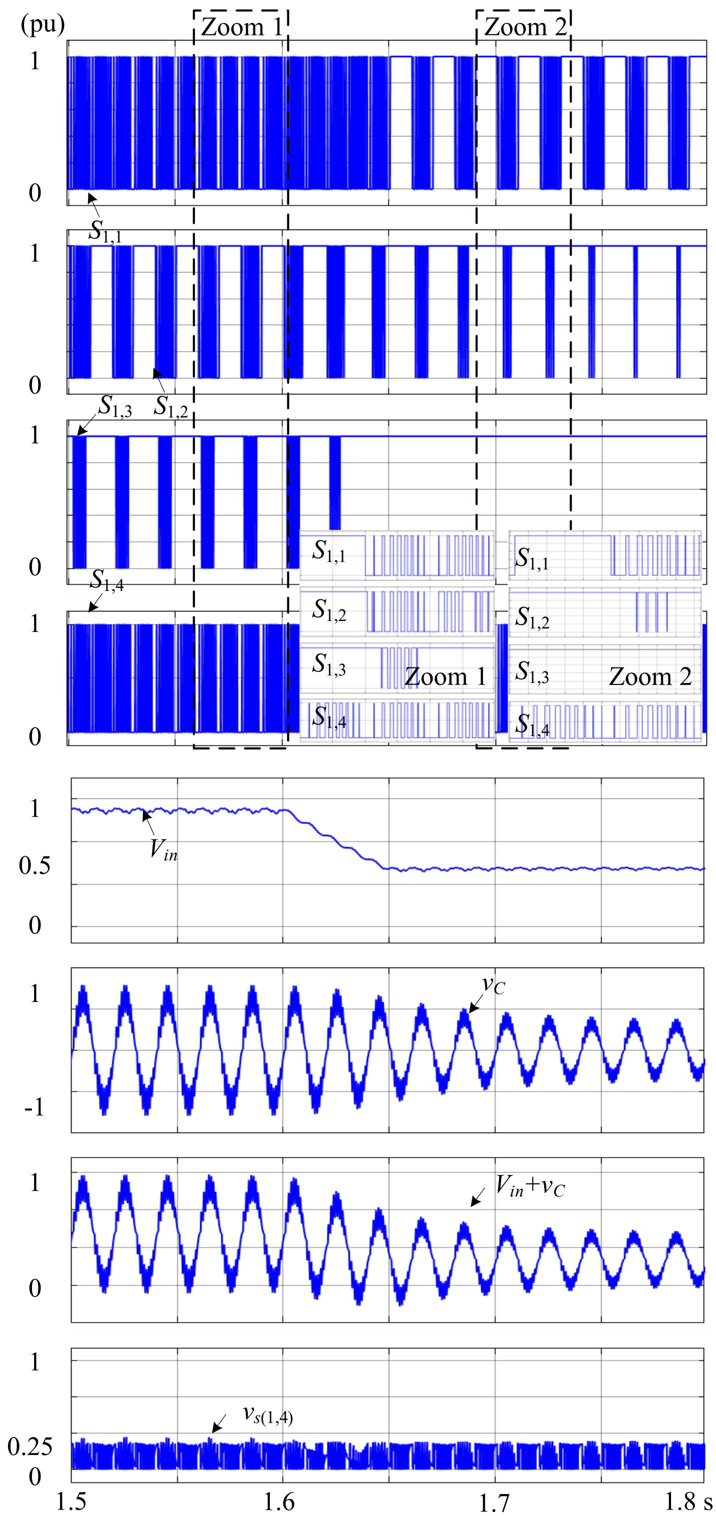

Figure 6.11: Simulated waveforms of the modified converter under different conditions: With changes in both DC-link voltage and output AC voltage.

Figure 6.10 depicts simulated waveforms of the proposed modified transformerless CSCs under various conditions, including scenarios with and without the half-bridge converters, as well as variations in output AC voltage. During the time interval $1 < t < 1.1$s, the bottom switches $S_{1,1}$, $S_{1,2}$, and $S_{1,3}$ of half-bridge converters remain on, while switch $S_{1,4}$ is switched on and off according to the original converter's modulation. The modified converter functions equivalently to the original one. Under rated conditions, with V_{in} = 1 pu and v_C = 1 pu, the maximum voltage stress on $S_{1,4}$ occurs during Mode 2_1 and is equal to $V_{in} + v_{C\text{-}peak}$ (1 pu).

During the time interval $1.1 < t < 1.2$s, the selection of the three half-bridge converters is guided by Equation (6.4) to manage the voltage stress on $S_{1,4}$, limiting it to 0.25 pu (1 pu = $V_{in} + v_{C\text{-}peak}$). The switches of the chosen half-bridge submodules are then turned on or off with details outlined in Zoom 1. Notably, the switching frequencies of $S_{1,2}$ and $S_{1,3}$ are lower than that of $S_{1,4}$, while $S_{1,1}$ shares the same switching frequency as $S_{1,4}$. This discrepancy arises from the earlier analysis indicating that not all half-bridge submodules are necessarily needed for operation, resulting in a reduced average of switching frequencies. Consequently, under rated conditions, the maximum voltage stress on $S_{1,4}$ is effectively reduced to 0.25 pu with a reduced average of switching frequencies.

During the time interval $1.2 < t < 1.4$s, at t = 1.2s, the converter is regulated to function with V_{in} = 1 pu and v_C = 0.3 pu. This ensures that the maximum voltage stress on $S_{1,4}$ remains within the 0.25 pu limit across all modes of operation. As illustrated in Zoom 2, $S_{1,3}$ remains ON during this period, while the other two switches are switched according to Equation (6.4). This well agrees with the previous analysis that the average switching frequency of half-bridge converters is reduced.

Figure 6.11 illustrates simulated waveforms of the proposed converter under various conditions, encompassing changes in both DC-link voltage and output AC voltage. During the time interval $1.5 < t < 1.6$s, the modified converter operates under rated conditions, with V_{in} = 1 pu and v_C = 1 pu. Utilizing the cascaded half-bridge converters, the maximum voltage stress on $S_{1,4}$ is constrained to 0.25 pu. Notably, as depicted in Zoom 1, the switching frequencies of $S_{1,2}$ and $S_{1,3}$ are lower than that of $S_{1,4}$, thanks to the distinctive operational principle of the half-bridge converters.

In the subsequent period, $1.6 < t < 1.8$s, the input voltage decreases to V_{in} = 0.5 pu at t = 1.6s, resulting in a corresponding reduction of the output voltage to v_C = 0.5 pu. Despite this decrease, the maximum voltage stress on $S_{1,4}$ remains within the 0.25 pu limit. As observed in Zoom 2, the switching frequencies of $S_{1,1}$, $S_{1,2}$, and $S_{1,3}$ are further reduced, reflecting the decreased need for half-bridge converters due to the lower V_{in} and v_C values. This reduction contributes to a further decrease in switching losses.

Both simulations have confirmed that the proposed modified converter successfully eliminates series-connected switches by incorporating the introduced half-bridge converters. These converters operate with reduced average switching frequencies compared to their counterparts in the original converter, contributing to reduced switching losses.

6.3.2 Experiment results

The circuit used for experiment is the same as that for simulation, depicted in Figure 6.8. The experiment also employs two CSC modules and three half-bridge converters. V_{in} is also realized using a three-phase variac, while capacitor charging of the half-bridge converters is realized by three single-phase transformers.

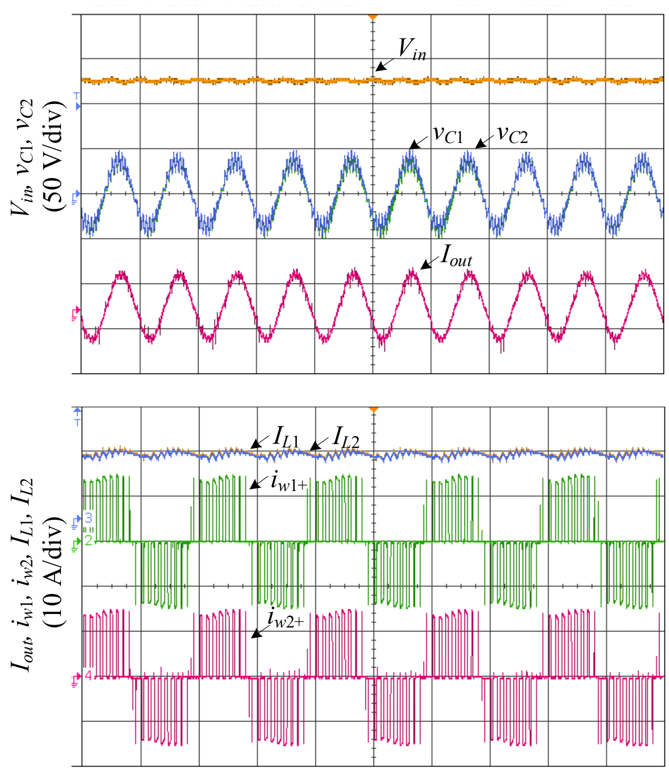

Figure 6.12: Experimental waveforms of the proposed converter under steady states.

Figure 6.12 shows the experimental waveforms of the modified converter under steady state. The converter is operating at rated conditions: the input voltage V_{in} is 1 pu (120 V), the output capacitor voltages v_{C1} and v_{C2} are 1 pu (35 V), the load current i_{out} is 1 pu (5 A), and the two inductor currents (I_{L1} and I_{L2}) are 1 pu (14 A). i_{w1} and i_{w2} are the respective output PWM currents of the two CSC modules. As shown in the figures, both inductor currents and output capacitor voltages are well balanced.

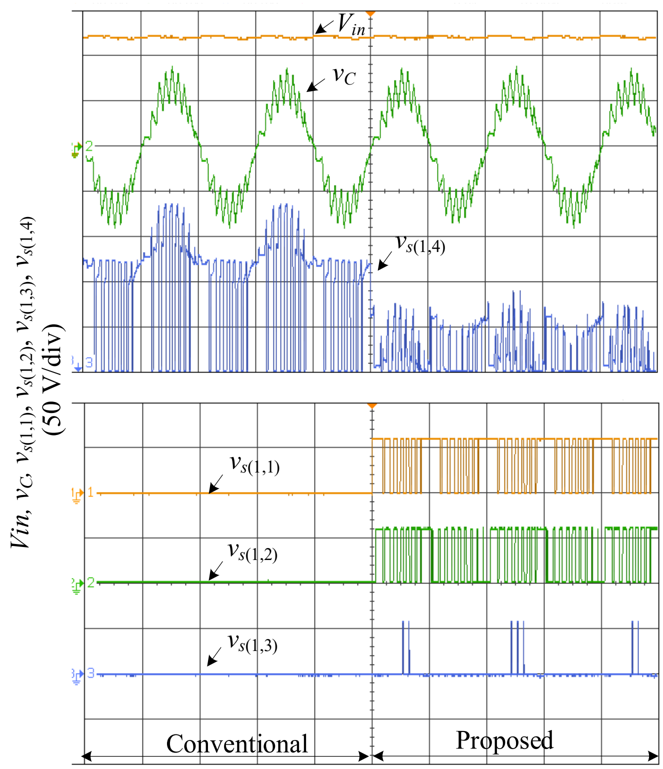

Figure 6.13: Experimental waveforms of the proposed converter under different conditions: With and without the half-bridge converters.

Figure 6.13 displays the experimental waveforms of the modified converter under different operating schemes. Initially, the modified converter operates identically to the original converter, with all bottom switches of the three half-bridge converters turned on, resulting in zero outputs ($v_{s(1,1)} = v_{s(1,2)} = v_{s(1\text{-},3)} = 0$), as depicted in the figure. Consequently, the voltage stress on switch $S_{1\text{-}4}$ remains the same as in the original converter.

Subsequently, the modified converter operates under the proposed scheme, where the three half-bridge submodules are selectively turned on or off according to Equation (6.4) to reduce the voltage stress $v_{s(1,4)}$. During the negative half cycle of v_C, two half-bridge submodules are turned off while the third one remains on ($v_{s(1,3)} = 0$), as illustrated in the figure. Conversely, during the positive half cycle, $v_{s(1,4)}$ reaches its maximum value around the peak of v_C, during which all three half-bridge submodules are turned on. In this case study, the switching frequency of $S_{1,3}$ is reduced from 1080 Hz in the original converter to just 300 Hz in the proposed scheme.

Figure 6.14 illustrates the experimental waveforms of the modified converter operating under a load change. Initially, the converter operates at rated conditions, after which the load is reduced from 1 pu to 0.6 pu, resulting in a decrease in the output voltage v_C. The waveform shows that the voltage stress $v_{s(1,4)}$ remains within the expected range before and after the load change. Notably, under the light load condition depicted in the figure, the third half-bridge converter ($v_{s(1,3)} = 0$) remains off. This is due to the reduction in v_C, which subsequently reduces the voltage stress on switch $S_{1,4}$. This observation aligns with the previous analysis, demonstrating that the switching frequencies of the half-bridge submodule switches are further reduced under light load conditions.

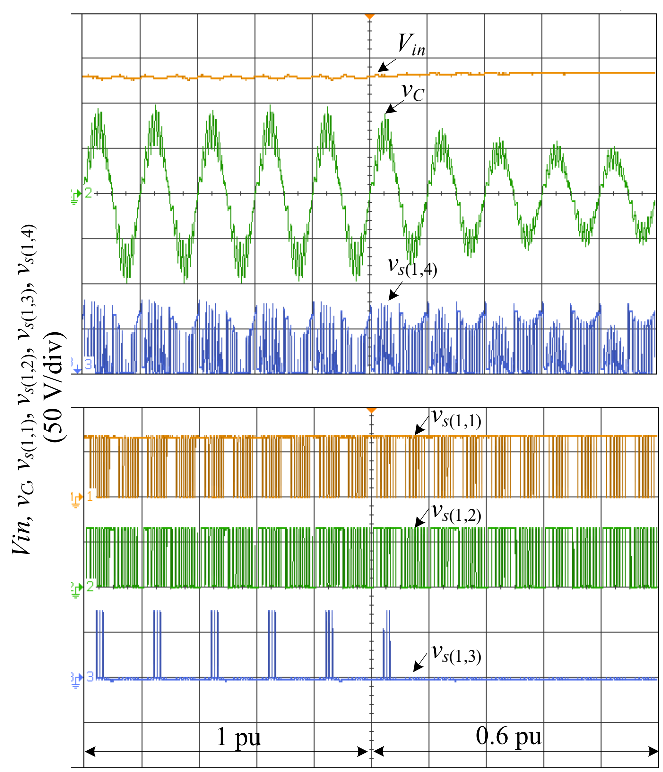

Figure 6.14: Experimental waveforms of the proposed converter under load change.

6.4 Investigation of integration of generator- and grid-side converters

On the generator side, three power converters are developed and presented in Chapters 2, 3, and 4. On the grid side, a transformerless converter and its modified version are introduced in Chapters 5 and 6. The power conversion system of a wind system is realized by integrating one of the three generator-side converters and one of the two grid-side transformerless converters. As discussed earlier, the proposed converters have distinct features and preferred applications. Consequently, different combinations of generator-side and grid-side converters result in various power conversion systems with different performance characteristics and applications. In this section, we examine an example power conversion system, combining the phase-shifting transformer-based generator-side converter (Chapter 2) with the grid-side transformerless converter (Chapter 6), to investigate the performance of the integrated power conversion system.

Figure 6.15 illustrates the simplified power conversion system, consisting of a generator-side phase-shifting transformer-based converter and a grid-side transformerless converter. The turbine-generator is modeled as an ideal three-phase voltage source, and an RL load is used on the grid side. L_f and C_f form an LC filter, which filters the harmonics of the output voltage of the cascaded buck converter on the generator side, enabling long transmission to the grid-side converter. Controls on both sides, including generator-side MPPT and grid-side reactive power control, are beyond the scope of this thesis and will be addressed in future work.

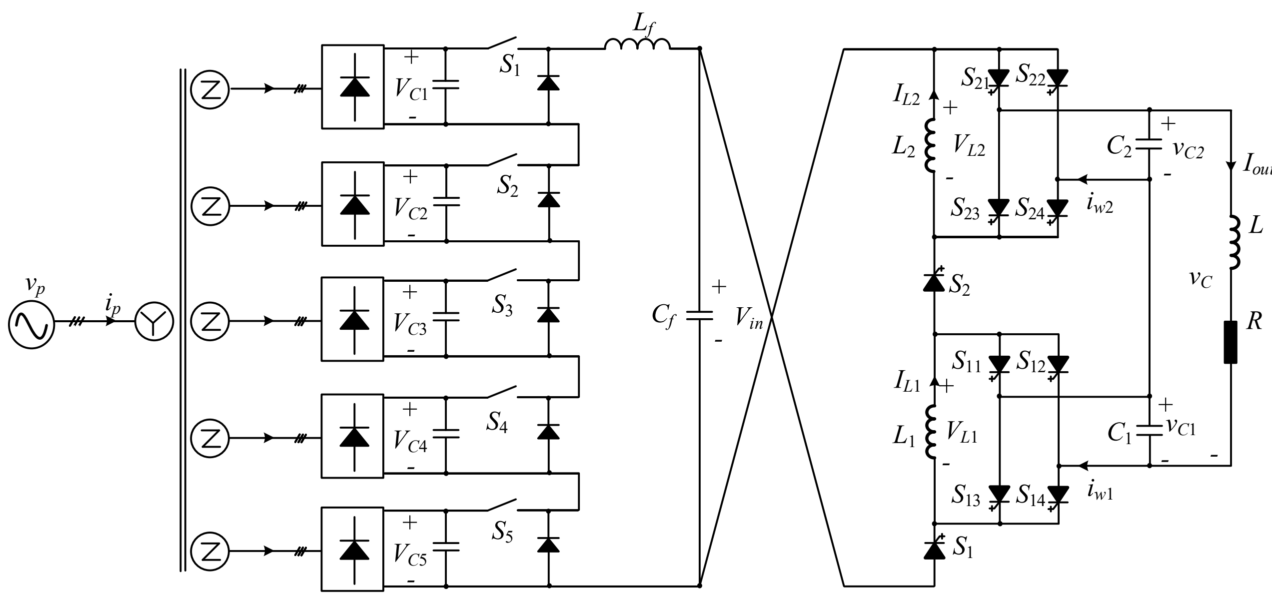

Figure 6.15: Circuit used in the simulation.

Figure 6.16 shows the simulated waveforms of the integration of generator- and grid-side converters under both steady and dynamic states. Before t = 0.5s, the converter is operating under rated conditions. On the generator side, the current i_p, used to simulate the generator stator current, exhibits superior harmonics performance thanks to the use of a phase-shifting transformer. On the grid side, both inductor currents balance ($I_{L1} = I_{L2}$) and capacitor voltage balance ($v_{C1} = v_{C2}$) are achieved.

At t = 0.5s, v_p, which simulates the generator output voltage, undergoes a step change from 1 pu to 0.5 pu, while the controls of the cascaded buck converter and the grid-side converter remain unchanged. The resultant DC-link voltage V_{in} reduces from 1 pu to 0.5 pu, and the inductor currents and capacitor voltages also drop to 0.5 pu, respectively. During the transition, the diode rectifier on the generator side becomes reverse-biased, resulting in zero current i_p, as shown in the figure.

In summary, the integration of generator- and grid-side converters operates successfully, ensuring the desired performance of power converters on both sides.

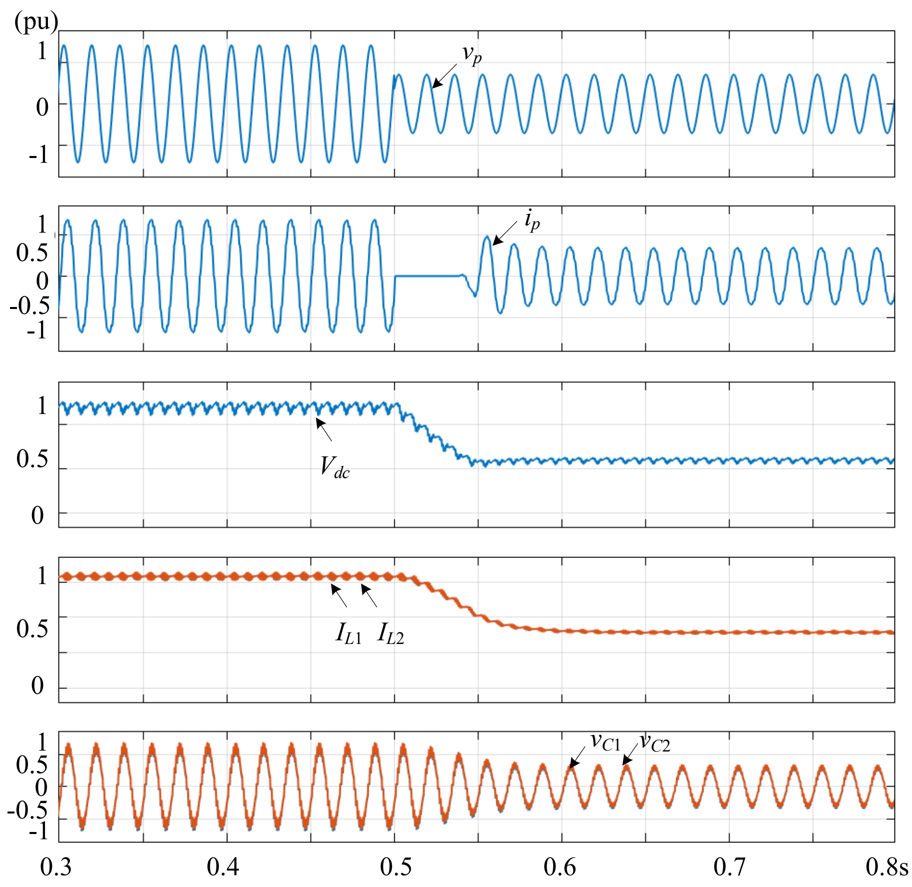

Figure 6.16: Simulation results under both steady and dynamic states.

6.5 Conclusions

In the CSC-type series DC-based WECS, grid-side CSCs traditionally incorporate bulky and expensive line-frequency transformers. To address this limitation, the preceding chapter introduced the first-ever transformerless CSCs, offering significant reductions in WECS size and weight. However, this solution necessitated additional switches, including one with an HVDC-level rating, leading to the use of series-connected switches and the mandatory implementation of costly and complex voltage balancing controls.

This chapter presents the development of a modified version of transformerless CSCs, achieved by using cascaded half-bridge converters. This modification eliminates the need for series-connected switches, thereby eliminating the requirement for expensive and complex voltage balancing schemes, while retaining all the advantages of the original converter. Unlike conventional half-bridge converters that generate AC voltages, the half-bridge converters used in the modified converter are designed to generate variable DC voltages. This reduction in voltage stress on the extra switch of the n^{th} CSC module eliminates the need for series-connected switches.

Although the implementation of these half-bridge converters requires additional components, including extra switches and charging systems, they offer a unique zero-load operation. This feature enables the use of components with very small VA ratings without imposing significant burdens on the system. Additionally, the average switching frequencies of the half-bridge converters are reduced compared to their counterparts in the original converter, leading to reduced switching losses.

The performance of the proposed modified transformerless CSCs under various conditions has been verified through both simulations and lab-scale experiments.

Chapter 7

Conclusions and Future Work

The thesis research objectives include the development of innovative generator-side power converters and grid-side power converters for the CSC-type series DC-based WECS. Existing generator-side converters are classified into four types: passive converter + LFT, passive converter + MFT, active converter + LFT, and active converter + MFT, each of which has its own advantages and disadvantages. In this thesis, innovative power converters have been proposed for the generator-side converter of WECS. They effectively addressed the challenges of existing generator-side power converters. Existing grid-side power converters are realized by using conventional three-phase CSCs connected in series at input and in parallel at output through bulky and costly line-frequency transformers. In this thesis, transformerless CSCs were proposed. They eliminate the use of line-frequency transformers, contributing to reductions in size and weight.

7.1 Contributions and conclusions

The contributions and conclusions are listed below.

(1) Generator-side passive rectifier-based converter with phase-shifting transformer

The LFT and passive rectifier-based converters are well-studied power converters utilized on the generator side of WECS. The LFT, a mature technology, serves to isolate the generator from HVDC levels, allowing the use of generators with regular insulation levels. Passive rectifier-based converters offer WECS with low cost, high reliability, simplicity, and scalability. However, the utilization of passive rectifiers results in highly distorted generator stator currents, leading to increased power losses and reduced lifespan of generators. To address this issue while retaining the advantages of both the LFT and passive rectifier-based converters, a phase-shifting transformer-based converter was proposed. This converter comprises a phase-shifting transformer, a multi-pulse diode rectifier, and a cascaded DC-DC converter. The phase-shifting transformer has the capability to eliminate specific current harmonics, thereby significantly improving the performance of generator stator current harmonics and reducing power losses, ultimately prolonging the service life of generators. Furthermore, like the LFT, the phase-shifting transformer is also a mature technology. The inclusion of a multi-pulse diode rectifier in the proposed converter ensures the retention of the advantages associated with passive rectifiers. Additionally, the cascaded DC-DC converter not only facilitates generator-side MPPT control but also features inherent capacitor voltage balancing. In summary, the proposed converter effectively addresses the shortcomings of existing LFT and passive rectifier-based converters while preserving all their advantages.

(2) Generator-side passive rectifier-based converter with multi-phase generators and medium-frequency transformers

The proposed passive rectifier-based converters using phase-shifting transformer effectively addressed the challenges of highly distorted generator stator currents associated with passive rectifiers while retaining all advantages of passive rectifiers including low cost, high reliability, simplicity, and scalability. However, the phase-shifting transformer is also an LFT, featuring large size and weight, posing a significant challenge to WECS, where the space in the tower nacelle is limited. To address the challenge associated with the bulky LFT while preserving advantages of passive rectifier, a new generator-side power converter was proposed. It is a multi-phase generator-based converter comprising a multi-phase generator, diode rectifiers, and a modular MFT-based DC-DC converter. The use of diode rectifiers allows the proposed converter to retain advantages associated with diode rectifiers, such as low cost and high reliability, while the utilization of a multi-phase generator enables the elimination of specific current harmonics generated by diode rectifiers, thereby significantly improving the performance of generator stator current harmonics, and reducing power losses, ultimately prolonging the service life of generators. The employment of MFT allows the use of generators with regular insulation requirements as well as contributing to reduced size and weight of WECS compared with the LFT.

(3) Generator-side active rectifier-based converter with modular medium-frequency transformers

Passive rectifiers are known for their low cost, high reliability, simplicity, and scalability, whereas active rectifiers provide superior performance in terms of generator stator current harmonics. While LFT technology is well-established, it tends to be bulky. In contrast, MFT technology offers a smaller size and weight, making it preferable for WECS installations where space in the nacelle is limited. A hybrid converter based on the active rectifier + MFT configuration was proposed and studied. It comprises an active rectifier and a modular MFT-based converter.

The use of an active rectifier ensures superior harmonics performance of generator stator currents, while the use of modular MFTs contributes to size and weight reductions in the generator-side conversion system. The hybrid converter achieves advantages associated with both active rectifiers and MFTs simultaneously.

(4) Grid-side transformerless series-connected current source converters

In CSC-type series DC-based WECS, grid-side converters employ conventional three-phase CSC modules connected in series at their input and in parallel at their output. However, this configuration necessitates the use of line-frequency transformers to provide isolated current paths for each CSC module at the input and to boost low voltage to high voltage levels as required. These transformers, with power ratings matching that of the entire wind system, are cumbersome and expensive, posing a significant burden to WECS. To address challenges associated with line-frequency transformers, transformerless series-connected CSCs were proposed, eliminating the need for transformers in series-connected CSCs for the first time. This elimination yields substantial cost and size reductions. Additionally, a novel modulation scheme tailored for these transformerless CSCs was developed. This scheme enables the proposed converter to achieve buck-boost operation and inherently balance DC inductor currents and AC capacitor voltages without the need for extra balancing controls.

(5) Grid-side transformerless series-connected current source converters without series-connected switches

In the CSC-type series DC-based WECS, grid-side CSCs incorporate bulky and expensive line-frequency transformers. To address this limitation, transformerless CSCs were propsoed, offering significant reductions in WECS size and weight. However, this solution necessitated additional switches, including one with an HVDC-level rating, leading to the use of series-connected switches and the mandatory implementation of costly and complex voltage balancing controls. To address this challenge while retaining all advantages of the original transformerless CSCs, a modified version of transformerless CSCs was propsoed. This modification eliminates the need for series-connected switches by using cascaded half-bridge converter, thereby eliminating the requirement for expensive and complex voltage balancing schemes, while retaining all the advantages of the original converter. In addition, although the implementation of these half-bridge converters requires additional components, including extra switches and charging systems, they offer a unique zero-load operation. This feature enables the use of components with very small VA ratings without imposing significant burdens on the system. Additionally, the average switching frequencies of the half-bridge converters are reduced compared to their counterparts in the original converter, leading to reduced switching losses.

7.2 Future work

(1) DC-link current minimization of the CSC-type series DC-based WECS

In CSC-type series DC-based WECS, the DC-link current plays an essential role. The achievement of generator-side control generates a DC-link current reference, and the achievement of grid-side control generates another DC-link current reference. To ensure control objectives at both the generator and grid sides, the greater of the two references is selected as the DC-link current reference of the system. Conversely, a lower DC-link current contributes to lower power losses of WECS. Achieving control objectives at both the generator and grid sides while minimizing the DC-link current simultaneously poses a challenge. A scheme to minimize the DC-link current of the proposed CSC-type WECS will be studied.

(2) Control scheme of the proposed WECS with grid-connected three-phase transformerless CSCs

In this thesis research, only the single-phase converter of the proposed transformerless CSCs with an RL load was studied, while its three-phase version under grid-connected operation was not investigated. One potential challenge involved in three-phase operation is the circulation of currents between interphases. Another challenge arises in its grid-connected operation, where DC-link current control becomes challenging due to the different configuration of transformerless CSCs compared to conventional CSCs. Additionally, integrating the proposed generator-side converter and grid-side converter requires a coordinated control scheme. These aspects will be planned for future work.

(3) Optimization of proposed transformerless CSCs

The proposed transformerless CSCs eliminate bulky and costly line-frequency transformers, resulting in significant reductions in the size and weight of WECS. However, they face a couple of challenges. One challenge is the overvoltage issue resulting from the operation of series-connected DC inductors. Another challenge is the need for charging systems consisting of isolated transformers and passive rectifiers, despite their small VA ratings. These challenges will be studied in future work.

References

[1] "Global offshore wind report 2023", Global wind energy council, 2023.

[2] "Wind energy in Europe 2011 statistic and outlook for 2013-2027", Wind Europe, 2023.

[3] Z. Chen, J. M. Guerrero and F. Blaabjerg, "A Review of the State of the Art of Power Electronics for Wind Turbines," in *IEEE Transactions on Power Electronics*, vol. 24, no. 8, pp. 1859-1875, Aug. 2009, doi: 10.1109/TPEL.2009.2017082.

[4] F. Blaabjerg and K. Ma, "Future on Power Electronics for Wind Turbine Systems," in *IEEE Journal of Emerging and Selected Topics in Power Electronics*, vol. 1, no. 3, pp. 139-152, Sept. 2013, doi: 10.1109/JESTPE.2013.2275978.

[5] J. M. Carrasco *et al*., "Power-Electronic Systems for the Grid Integration of Renewable Energy Sources: A Survey," in *IEEE Transactions on Industrial Electronics*, vol. 53, no. 4, pp. 1002-1016, June 2006, doi: 10.1109/TIE.2006.878356.

[6] M. Liserre, R. Cárdenas, M. Molinas and J. Rodriguez, "Overview of Multi-MW Wind Turbines and Wind Parks," in *IEEE Transactions on Industrial Electronics*, vol. 58, no. 4, pp. 1081-1095, April 2011, doi: 10.1109/TIE.2010.2103910.

[7] V. Yaramasu, B. Wu, P. C. Sen, S. Kouro and M. Narimani, "High-power wind energy conversion systems: State-of-the-art and emerging technologies," in *Proceedings of the IEEE*, vol. 103, no. 5, pp. 740-788, May 2015, doi: 10.1109/JPROC.2014.2378692.

[8] B. Wu, High-Power Converters and AC Drives. Hoboken, NJ, USA: Wiley, 2016.

[9] Olimpo Anaya-Lara, David Campos-Gaona, Edgar Moreno-Goytia, Grain Adam, Offshore Wind Energy Generation, Wiley, 2014.

[10] H. Wu, J. Yu, J. Liu, R. Mei, X. Ji and H. Wang, "Voltage control of offshore wind farm considering reactive ability of electrochemical energy storage," *2022 IEEE Sustainable Power and Energy Conference (iSPEC)*, Perth, Australia, 2022, pp. 1-5, doi: 10.1109/iSPEC54162.2022.10032975.

[11] F. Deng, Dong Liu, Yanbo Wang, Qingsong Wang and Z. Chen, "Modular multilevel converters based variable speed wind turbines for grid faults," *IECON 2016 - 42nd Annual Conference of the IEEE Industrial Electronics Society*, Florence, Italy, 2016, pp. 2420-2425, doi: 10.1109/IECON.2016.7793594.

[12] X. Zhao, B. Li, B. Zhang and D. Xu, "A High-Power Step-Up DC/DC Converter Dedicated to DC Offshore Wind Farms," in *IEEE Transactions on Power Electronics*, vol. 37, no. 1, pp. 65-69, Jan. 2022, doi: 10.1109/TPEL.2021.3102228.

[13] K. Musasa and N. I. Nwulu, "A Novel Concept for Offshore Wind-Power Plant with DC Collection System Based on Radial-Connected Converter Topology," in *IEEE Access*, vol. 6, pp. 67217-67222, 2018, doi: 10.1109/ACCESS.2018.2879347.

[14] O. Beik and A. S. Al-Adsani, "A Wind Turbine Generator Design and Optimization for DC Collector Grids," in *IEEE Journal of Emerging and Selected Topics in Power Electronics*, vol. 10, no. 1, pp. 484-493, Feb. 2022, doi: 10.1109/JESTPE.2021.3066278.

[15] M. Gholamian and O. Beik, "Coordinate Control of Wind Turbines in a Medium Voltage DC Grid," in *IEEE Transactions on Industry Applications*, vol. 59, no. 5, pp. 6480-6488, Sept.-Oct. 2023, doi: 10.1109/TIA.2023.3278648.

[16] D. Mukherjee and A. Banerjee, "DC Grid Interface for the Integrated Generator–Rectifier Architecture in Wind Energy Systems," in *IEEE Transactions on Power Electronics*, vol. 37, no. 12, pp. 14795-14808, Dec. 2022, doi: 10.1109/TPEL.2022.3197081.

[17] F. Blaabjerg, Z. Chen and S. B. Kjaer, "Power electronics as efficient interface in dispersed power generation systems," in *IEEE Transactions on Power Electronics*, vol. 19, no. 5, pp. 1184-1194, Sept. 2004, doi: 10.1109/TPEL.2004.833453.

[18] Essential energy, Horns Rev Offshore wind Farm, 2002.

[19] Hitachi Energy, VSC technology pioneers, Hitachi Energy, Sweden, 2023.

[20] P. Bresesti, W. L. Kling, R. L. Hendriks and R. Vailati, "HVDC Connection of Offshore Wind Farms to the Transmission System," in *IEEE Transactions on Energy Conversion*, vol. 22, no. 1, pp. 37-43, March 2007, doi: 10.1109/TEC.2006.889624.

[21] D. Das, J. Pan and S. Bala, "HVDC Light for large offshore wind farm integration," *2012 IEEE Power Electronics and Machines in Wind Applications*, Denver, CO, USA, 2012, pp. 1-7, doi: 10.1109/PEMWA.2012.6316363.

[22] R. Sharma, T. W. Rasmussen, K. H. Jensen and V. Akamatov, "Modular VSC converter based HVDC power transmission from offshore wind power plant: Compared to the conventional HVAC system," *2010 IEEE Electrical Power & Energy Conference*, Halifax, NS, Canada, 2010, pp. 1-6, doi: 10.1109/EPEC.2010.5697192.

[23] N. Flourentzou, V. G. Agelidis and G. D. Demetriades, "VSC-Based HVDC Power Transmission Systems: An Overview," in *IEEE Transactions on Power Electronics*, vol. 24, no. 3, pp. 592-602, March 2009, doi: 10.1109/TPEL.2008.2008441.

[24] Y. Xia, K. H. Ahmed and B. W. Williams, "A PWM Current Source-Based DC Transmission System for Multiple Wind Turbine Interfacing," in *IEEE Journal of Emerging and Selected Topics in Power Electronics*, vol. 2, no. 4, pp. 784-796, Dec. 2014, doi: 10.1109/JESTPE.2014.2352677.

[25] W. Chen, A. Q. Huang, C. Li, G. Wang and W. Gu, "Analysis and Comparison of Medium Voltage High Power DC/DC Converters for Offshore Wind Energy Systems," in *IEEE Transactions on Power Electronics*, vol. 28, no. 4, pp. 2014-2023, April 2013, doi: 10.1109/TPEL.2012.2215054.

[26] J. Robinson, D. Jovcic and G. Joos, "Analysis and Design of an Offshore Wind Farm Using a MV DC Grid," in *IEEE Transactions on Power Delivery*, vol. 25, no. 4, pp. 2164-2173, Oct. 2010, doi: 10.1109/TPWRD.2010.2053390.

[27] M. Pape and M. Kazerani, "An Offshore Wind Farm with DC Collection System Featuring Differential Power Processing," in *IEEE Transactions on Energy Conversion*, vol. 35, no. 1, pp. 222-236, March 2020, doi: 10.1109/TEC.2019.2951331.

[28] C. Meyer, M. Hoing, A. Peterson and R. W. De Doncker, "Control and Design of DC-Grids for Offshore Wind Farms," *Conference Record of the 2006 IEEE Industry Applications Conference Forty-First IAS Annual Meeting*, Tampa, FL, USA, 2006, pp. 1148-1154, doi: 10.1109/IAS.2006.256677.

[29] C. Zhan, C. Smith, A. Crane, A. Bullock and D. Grieve, "DC transmission and distribution system for a large offshore wind farm," *9th IET International Conference on AC and DC Power Transmission (ACDC 2010)*, London, 2010, pp. 1-5, doi: 10.1049/cp.2010.0981.

[30] P. Hu, R. Yin, B. Wei, Y. Luo and F. Blaabjerg, "Modular Isolated LLC DC/DC Conversion System for Offshore Wind Farm Collection and Integration," in *IEEE Journal of Emerging and Selected Topics in Power Electronics*, vol. 9, no. 6, pp. 6713-6725, Dec. 2021, doi: 10.1109/JESTPE.2021.3062677.

[31] M. Guan, "A Series-Connected Offshore Wind Farm Based on Modular Dual-Active-Bridge (DAB) Isolated DC–DC Converter," in *IEEE Transactions on Energy Conversion*, vol. 34, no. 3, pp. 1422-1431, Sept. 2019, doi: 10.1109/TEC.2019.2918200.

[32] F. An, B. Zhao, B. Cui and R. Bai, "Multi-Functional DC Collector for Future All-DC Offshore Wind Power System: Concept, Scheme, and Implement," in *IEEE Transactions on Industrial Electronics*, vol. 69, no. 8, pp. 8134-8145, Aug. 2022, doi: 10.1109/TIE.2021.3109539.

[33] F. Rong, G. Wu, X. Li, S. Huang and B. Zhou, "ALL-DC Offshore Wind Farm With Series-Connected Wind Turbines to Overcome Unequal Wind Speeds," in *IEEE Transactions on Power Electronics*, vol. 34, no. 2, pp. 1370-1381, Feb. 2019, doi: 10.1109/TPEL.2018.2834965.

[34] M. Pape and M. Kazerani, "A Generic Power Converter Sizing Framework for Series-Connected DC Offshore Wind Farms," in *IEEE Transactions on Power Electronics*, vol. 37, no. 2, pp. 2307-2320, Feb. 2022, doi: 10.1109/TPEL.2021.3106578.

[35] T. H. Nguyen, D. -C. Lee and C. -K. Kim, "A Series-Connected Topology of a Diode Rectifier and a Voltage-Source Converter for an HVDC Transmission System," in *IEEE Transactions on Power Electronics*, vol. 29, no. 4, pp. 1579-1584, April 2014, doi: 10.1109/TPEL.2013.2283368.

[36] G. Guo *et al.*, "Series-Connected-Based Offshore Wind Farms With Full-Bridge Modular Multilevel Converter as Grid- and Generator-side Converters," in *IEEE Transactions on Industrial Electronics*, vol. 67, no. 4, pp. 2798-2809, April 2020, doi: 10.1109/TIE.2019.2912777.

[37] G. Guo et al., "HB and FB MMC Based Onshore Converter in Series-Connected Offshore Wind Farm," in IEEE Transactions on Power Electronics, vol. 35, no. 3, pp. 2646-2658, March 2020, doi: 10.1109/TPEL.2019.2929689.

[38] G. H. Kim, M. H. Kang, J. H. Ahn, E. -H. Kim and S. H. Chae, "Operation of DC series connected offshore wind farm by using tap changing transformer with MMC-HVDC," *2018 5th International Conference on Renewable Energy: Generation and Applications (ICREGA)*, Al Ain, United Arab Emirates, 2018, pp. 291-295, doi: 10.1109/ICREGA.2018.8337616.

[39] M. E. M. Rizk, S. Abulanwar, A. Ghanem and Z. Chen, "Investigation of Novel DC Wind Farm Layout During Continuous Operation and Lightning Strikes," in *IEEE Transactions on Power Delivery*, vol. 36, no. 4, pp. 2221-2230, Aug. 2021, doi: 10.1109/TPWRD.2020.3022853.

[40] C. Meyer, M. Hoing, A. Peterson and R. W. De Doncker, "Control and Design of DC Grids for Offshore Wind Farms," in *IEEE Transactions on Industry Applications*, vol. 43, no. 6, pp. 1475-1482, Nov.-dec. 2007, doi: 10.1109/TIA.2007.908182.

[41] N. Holtsmark, H. J. Bahirat, M. Molinas, B. A. Mork and H. K. Hoidalen, "An All-DC Offshore Wind Farm With Series-Connected Turbines: An Alternative to the Classical Parallel AC Model?," in *IEEE Transactions on Industrial Electronics*, vol. 60, no. 6, pp. 2420-2428, June 2013, doi: 10.1109/TIE.2012.2232255.

[42] A. Garcés and M. Molinas, "A Study of Efficiency in a Reduced Matrix Converter for Offshore Wind Farms," in *IEEE Transactions on Industrial Electronics*, vol. 59, no. 1, pp. 184-193, Jan. 2012, doi: 10.1109/TIE.2011.2130502.

[43] Y. Xu, Z. Wang, P. Liu, Q. Wei, F. Deng and Z. Zou, "The Modular Current-Fed High-Frequency Isolated Matrix Converters for Wind Energy Conversion," in *IEEE Transactions on Power Electronics*, vol. 37, no. 4, pp. 4779-4791, April 2022, doi: 10.1109/TPEL.2021.3123204.

[44] Z. Wang, B. Yuwen and M. Cheng, "Improvement of operating performance for the wind farm with a novel CSC type wind turbine-SMES hybrid system," *2012 IEEE International Symposium on Industrial Electronics*, Hangzhou, China, 2012, pp. 1017-1022, doi: 10.1109/ISIE.2012.6237228.

[45] R. E. Torres-Olguin, A. Garces, M. Molinas and T. Undeland, "Integration of Offshore Wind Farm Using a Hybrid HVDC Transmission Composed by PWM Current-Source Converter and Line-Commutated Converter," *2012 Asia-Pacific Power and Energy Engineering Conference*, Shanghai, China, 2012, pp. 1-4, doi: 10.1109/APPEEC.2012.6307103.

[46] S. Nishikata and F. Tatsuta, "A New Interconnecting Method for Wind Turbine/Generators in a Wind Farm and Basic Performances of the Integrated System," in *IEEE Transactions on Industrial Electronics*, vol. 57, no. 2, pp. 468-475, Feb. 2010, doi: 10.1109/TIE.2009.2026765.

[47] K. -i. Yamashita, G. Tsukamoto and S. Nishikata, "Steady-State Characteristics of a Line-Commutated Converter-Based High-Voltage Direct Current Transmission System for Series-Connected Wind Power Plants," in *IEEE Transactions on Industry Applications*, vol. 56, no. 4, pp. 3932-3939, July-Aug. 2020, doi: 10.1109/TIA.2020.2986984.

[48] M. Popat, B. Wu, F. Liu and N. Zargari, "Coordinated Control of Cascaded Current-Source Converter Based Offshore Wind Farm," in *IEEE Transactions on Sustainable Energy*, vol. 3, no. 3, pp. 557-565, July 2012, doi: 10.1109/TSTE.2012.2191986.

[49] E. Veilleux and P. W. Lehn, "Interconnection of Direct-Drive Wind Turbines Using a Series-Connected DC Grid," in *IEEE Transactions on Sustainable Energy*, vol. 5, no. 1, pp. 139-147, Jan. 2014, doi: 10.1109/TSTE.2013.2276616.

[50] Y. Xia, K. H. Ahmed and B. W. Williams, "Wind Turbine Power Coefficient Analysis of a New Maximum Power Point Tracking Technique," in IEEE Transactions on Industrial Electronics, vol. 60, no. 3, pp. 1122-1132, March 2013, doi: 10.1109/TIE.2012.2206332.

[51] M. Popat, B. Wu and N. R. Zargari, "A Novel Decoupled Interconnecting Method for Current-Source Converter-Based Offshore Wind Farms," in *IEEE Transactions on Power Electronics*, vol. 27, no. 10, pp. 4224-4233, Oct. 2012, doi: 10.1109/TPEL.2012.2191982.

[52] Q. Wei, B. Wu, D. Xu and N. R. Zargari, "A Medium-Frequency Transformer-Based Wind Energy Conversion System Used for Current-Source Converter-Based Offshore Wind Farm," in *IEEE Transactions on Power Electronics*, vol. 32, no. 1, pp. 248-259, Jan. 2017, doi: 10.1109/TPEL.2016.2524635.

[53] Q. Wei, B. Wu, D. Xu and N. R. Zargari, "A New Configuration Using PWM Current Source Converters in Low-Voltage Turbine-Based Wind Energy Conversion Systems," in *IEEE Journal of Emerging and Selected Topics in Power Electronics*, vol. 6, no. 2, pp. 919-929, June 2018, doi: 10.1109/JESTPE.2017.2748281.

[54] Q. Wei, B. Wu, D. Xu and N. R. Zargari, "Bipolar Operation Investigation of Current Source Converter Based Wind Energy Conversion Systems," in *IEEE Transactions on Power Electronics*, vol. 33, no. 2, pp. 1294-1302, Feb. 2018, doi: 10.1109/TPEL.2017.2683262.

[55] Q. Wei, B. Wu, D. Xu and N. R. Zargari, "Power Balancing Investigation of Grid-Side Series-Connected Current Source Inverters in Wind Conversion Systems," in *IEEE Transactions on Industrial Electronics*, vol. 64, no. 12, pp. 9451-9460, Dec. 2017, doi: 10.1109/TIE.2017.2711566.

[56] Y. Liu, L. -l. Huang, J. Yan, Q. Wang and Y. Miao, "Analysis of power abandon characteristics in Offshore Wind Farms with DC Series-Parallel Architectures," *2021 International Conference on Power System Technology (POWERCON)*, Haikou, China, 2021, pp. 965-970, doi: 10.1109/POWERCON53785.2021.9697592.

[57] H. J. Bahirat and B. A. Mork, "Operation of DC Series–Parallel Connected Offshore Wind Farm," in *IEEE Transactions on Sustainable Energy*, vol. 10, no. 2, pp. 596-603, April 2019, doi: 10.1109/TSTE.2018.2839712.

[58] L. Ming, W. Ding, C. Yin, Z. Xin and P. C. Loh, "A Direct Carried-Based PWM Scheme With Reduced Switching Harmonics and Common-Mode Voltage for Current Source Converter," in *IEEE Transactions on Power Electronics*, vol. 36, no. 7, pp. 7783-7796, July 2021, doi: 10.1109/TPEL.2020.3042387.

[59] L. Ming, W. Ding, P. C. Loh and Z. Xin, "A Direct Carrier-Based Modulation Scheme with Full Index Range for DC-Link Current Ripple Mitigation of a Current Source Converter," in *IEEE Transactions on Industrial Electronics*, vol. 69, no. 1, pp. 452-462, Jan. 2022, doi: 10.1109/TIE.2021.3053895.

[60] J. He *et al*., "A Fault-Tolerant Operation Approach for Grid-Tied Five-Phase Current-Source Converters with One-Phase Supplying Wire Broken," in *IEEE Transactions on Power Electronics*, vol. 34, no. 7, pp. 6200-6218, July 2019, doi: 10.1109/TPEL.2018.2867219.

[61] D. Xu, N. R. Zargari, B. Wu, J. Wiseman, B. Yuwen and S. Rizzo, "A Medium Voltage AC Drive with Parallel Current Source Inverters for High Power Applications," *2005 IEEE 36th Power Electronics Specialists Conference*, Dresden, Germany, 2005, pp. 2277-2283, doi: 10.1109/PESC.2005.1581949.

[62] Z. Bai, Z. Zhang and X. Ruan, "A Natural Soft-Commutation PWM Scheme for Current Source Converter and Its Logic Implementation," in *IEEE Transactions on Industrial Electronics*, vol. 58, no. 7, pp. 2772-2779, July 2011, doi: 10.1109/TIE.2010.2070773.

[63] L. Ding, Y. Li and Y. W. Li, "A New Current Source Converter Using AC-Type Flying-Capacitor Technique," in *IEEE Transactions on Power Electronics*, vol. 36, no. 9, pp. 10307-10316, Sept. 2021, doi: 10.1109/TPEL.2021.3067799.

[64] G. Migliazza et al., "DC Current Control for a Single-Stage Current Source Inverter in Motor Drive Application," in *IEEE Transactions on Power Electronics*, vol. 36, no. 3, pp. 3367-3376, March 2021, doi: 10.1109/TPEL.2020.3013301.

[65] E. P. Wiechmann, P. Aqueveque, R. Burgos and J. Rodriguez, "On the Efficiency of Voltage Source and Current Source Inverters for High-Power Drives," in *IEEE Transactions on Industrial Electronics*, vol. 55, no. 4, pp. 1771-1782, April 2008, doi: 10.1109/TIE.2008.918625.

[66] X. Guo, Y. Yang and X. Wang, "Optimal Space Vector Modulation of Current-Source Converter for DC-Link Current Ripple Reduction," in *IEEE Transactions on Industrial Electronics*, vol. 66, no. 3, pp. 1671-1680, March 2019, doi: 10.1109/TIE.2018.2835396.

[67] P. Liu, Z. Wang, Q. Song, Y. Xu and M. Cheng, "Optimized SVM and Remedial Control Strategy for Cascaded Current-Source-Converters-Based Dual Three-Phase PMSM Drives System," in *IEEE Transactions on Power Electronics*, vol. 35, no. 6, pp. 6153-6164, June 2020, doi: 10.1109/TPEL.2019.2952672.

[68] J. He, Q. Li, H. Wang, Y. Lyu, H. Jia and C. Wang, "SVM Strategies for Simultaneous Common-Mode Voltage Reduction and DC Current Balancing in Parallel Current Source Converters," in *IEEE Transactions on Power Electronics*, vol. 33, no. 10, pp. 8859-8871, Oct. 2018, doi: 10.1109/TPEL.2017.2778505.

[69] J. Dai, D. Xu, B. Wu and N. R. Zargari, "Unified DC-Link Current Control for Low-Voltage Ride-Through in Current-Source-Converter-Based Wind Energy Conversion Systems," in *IEEE Transactions on Power Electronics*, vol. 26, no. 1, pp. 288-297, Jan. 2011, doi: 10.1109/TPEL.2010.2059377.

[70] L. Li, B. Li, Z. Wang, M. Yang and D. Xu, "Monopolar Symmetrical DC–DC Converter for All DC Offshore Wind Farms," in *IEEE Transactions on Power Electronics*, vol. 37, no. 4, pp. 4275-4287, April 2022, doi: 10.1109/TPEL.2021.3125095.

[71] P. D. Judge and T. C. Green, "Dynamic thermal rating of a Modular Multilevel Converter HVDC link with overload capacity," *2015 IEEE Eindhoven PowerTech*, Eindhoven, Netherlands, 2015, pp. 1-6, doi: 10.1109/PTC.2015.7232329.

[72] O. E. Oni, I. E. Davidson and K. N. I. Mbangula, "A review of LCC-HVDC and VSC-HVDC technologies and applications," *2016 IEEE 16th International Conference on Environment and Electrical Engineering (EEEIC)*, Florence, Italy, 2016, pp. 1-7, doi: 10.1109/EEEIC.2016.7555677.

[73] F. Tatsuta and S. Nishikata, "Experimental Studies on Dynamic Performances of Wind Power Plants Composed of Series-connected Wind Generators and Synchronous-compensator-commutated Thyristor Inverter," *2019 22nd International Conference on Electrical Machines and Systems (ICEMS)*, Harbin, China, 2019, pp. 1-6, doi: 10.1109/ICEMS.2019.8921934.

[74] L. Liu, Y. Pu and Y. Lu, "The Protection and Coordinated Control Study of VSC-HVDC Access System for Large-Scale Offshore Wind Power," *2022 4th International Conference on*

Smart Power & Internet Energy Systems (SPIES), Beijing, China, 2022, pp. 746-750, doi: 10.1109/SPIES55999.2022.10082100.

[75] X. Wang, Y. Qi, X. Xu, R. Huang, Y. Ruan and X. Bian, "A Mixed Model- and Data-Driven Approach for Subsynchronous Oscillation Analysis of VSC-HVDC Grid-Connected Offshore Wind Farm," *2021 IEEE 5th Conference on Energy Internet and Energy System Integration (EI2)*, Taiyuan, China, 2021, pp. 848-853, doi: 10.1109/EI252483.2021.9713615.

[76] A. Beddard and M. Barnes, "Availability analysis of VSC-HVDC schemes for offshore windfarms," *6th IET International Conference on Power Electronics, Machines and Drives (PEMD 2012)*, Bristol, 2012, pp. 1-6, doi: 10.1049/cp.2012.0345.

[77] J. Lange, R. Neubert, B. Alt, V. Hussennether and M. G. C. de Abreu, "Innovative Converter Testing Technology and Overall Reliability and Availability Performance of HVDC Solutions," *2021 AEIT HVDC International Conference (AEIT HVDC)*, Genoa, Italy, 2021, pp. 1-6, doi: 10.1109/AEITHVDC52364.2021.9474590.

[78] D. Guedon, P. Ladoux, S. Sanchez and S. Cornet, "High Voltage IGCTs for HVDC Converter-Stations," *2021 AEIT HVDC International Conference (AEIT HVDC)*, Genoa, Italy, 2021, pp. 1-6, doi: 10.1109/AEITHVDC52364.2021.9474610.

[79] T. H. Nguyen, Q. A. Le and D. -C. Lee, "A novel HVDC-link based on hybrid voltage-source converters," 2015 IEEE Energy Conversion Congress and Exposition (ECCE), Montreal, QC, Canada, 2015, pp. 3338-3343, doi: 10.1109/ECCE.2015.7310131.

[80] W. Wang, F. Gao, Y. Yang and F. Blaabjerg, "An Eight-Switch Five-Level Current Source Inverter," in *IEEE Transactions on Power Electronics*, vol. 34, no. 9, pp. 8389-8404, Sept. 2019, doi: 10.1109/TPEL.2018.2884846.

[81] L. Xing, Q. Wei and R. Y. Li, "A New 5-Level Current Source Inverter with Inherent Balancing," *2023 IEEE 14th International Symposium on Power Electronics for Distributed Generation Systems (PEDG)*, Shanghai, China, 2023, pp. 30-34, doi: 10.1109/PEDG56097.2023.10215120.

[82] Z. Wang and Q. Wei, "X-Type Five-Level Current Source Inverter," in *IEEE Transactions on Power Electronics*, vol. 38, no. 5, pp. 6283-6292, May 2023, doi: 10.1109/TPEL.2023.3244075.

[83] L. A. L. d. A. C. Costa, M. A. Vitorino, M. B. d. R. Corrêa, L. V. Hartmann and A. W. S. Ramalho, "X-Type Current Source Converters," in *IEEE Transactions on Power Electronics*, vol. 36, no. 11, pp. 12843-12856, Nov. 2021, doi: 10.1109/TPEL.2021.3082032.

[84] E. Agheb and H. K. Høidalen, "Medium frequency high power transformers, state of art and challenges," *2012 International Conference on Renewable Energy Research and Applications (ICRERA)*, Nagasaki, Japan, 2012, pp. 1-6, doi: 10.1109/ICRERA.2012.6477318.

[85] X. Fu, K. Al-Haddad, L. -A. Dessaint and H. Abdelhamid, "Series Connection of VSC Modules for Offshore Wind Farm Application," *2019 IEEE 28th International Symposium on Industrial Electronics (ISIE)*, Vancouver, BC, Canada, 2019, pp. 974-979, doi: 10.1109/ISIE.2019.8781460.

[86] J. Tait, S. Wang and K. H. Ahmed, "An Enhanced Series-Connected Offshore Wind Farm (SC-OWF) System Considering Fault Resiliency," in *IEEE Transactions on Power Delivery*, vol. 39, no. 1, pp. 352-362, Feb. 2024, doi: 10.1109/TPWRD.2022.3219373.

[87] H. A. Hussain and K. A. N. Al-Deen, "Design and Control of Series-DC Wind Farms based on Three-Phase Dual Active Bridge Converters," *2022 IEEE Energy Conversion Congress and Exposition (ECCE)*, Detroit, MI, USA, 2022, pp. 1-8, doi: 10.1109/ECCE50734.2022.9947753.

[88] K. Zhao, G. Li, B. Wang and M. Zhou, "Grid-connected topology of PMSG wind power system based on VSC-HVDC," *2011 4th International Conference on Electric Utility Deregulation and Restructuring and Power Technologies (DRPT)*, Weihai, China, 2011, pp. 297-302, doi: 10.1109/DRPT.2011.5993906.

[89] S. Chuangpishit and A. Tabesh, "Reduced model and control of diode-interfaced offshore wind farms with DC power systems," *2013 IEEE Electrical Power & Energy Conference*, Halifax, NS, Canada, 2013, pp. 1-5, doi: 10.1109/EPEC.2013.6802913.

[90] Y. Pang, X. Qu and W. Chen, "An LCC/VSC Hybrid Structure And Its Coordinated Control In Medium-Voltage DC Distribution System," *2022 10th International Conference on Smart Grid (icSmartGrid)*, Istanbul, Turkey, 2022, pp. 174-178, doi: 10.1109/icSmartGrid55722.2022.9848557.

[91] Z. Wang, B. Wu, D. Xu and N. R. Zargari, "Hybrid PWM for High-Power Current-Source-Inverter-Fed Drives With Low Switching Frequency," in *IEEE Transactions on Power Electronics*, vol. 26, no. 6, pp. 1754-1764, June 2011, doi: 10.1109/TPEL.2010.2087362.

[92] K. Gnanasambandam, A. K. Rathore, A. Edpuganti, D. Srinivasan and J. Rodriguez, "Current-Fed Multilevel Converters: An Overview of Circuit Topologies, Modulation Techniques, and Applications," in *IEEE Transactions on Power Electronics*, vol. 32, no. 5, pp. 3382-3401, May 2017, doi: 10.1109/TPEL.2016.2585576.

[93] X. Guo, D. Xu, J. M. Guerrero and B. Wu, "Space Vector Modulation for DC-Link Current Ripple Reduction in Back-to-Back Current-Source Converters for Microgrid Applications," in *IEEE Transactions on Industrial Electronics*, vol. 62, no. 10, pp. 6008-6013, Oct. 2015, doi: 10.1109/TIE.2015.2424397.

[94] M. A. Elgenedy, A. Abdel-Khalik, A. Elserougi, S. Ahmed and A. M. Massoud, "A new five-phase to three-phase back-to-back current source converter based wind energy conversion system," 2013 7th IEEE GCC Conference and Exhibition (GCC), Doha, Qatar, 2013, pp. 193-198, doi: 10.1109/IEEEGCC.2013.6705774.

[95] J. D. Ma, Bin Wu, N. R. Zargari and S. C. Rizzo, "A space vector modulated CSI-based AC drive for multimotor applications," in *IEEE Transactions on Power Electronics*, vol. 16, no. 4, pp. 535-544, July 2001, doi: 10.1109/63.931075.

[96] J. A. Roseline and M. Senthil Kumaran, "Generalized Modulation Technique for Current Source Converters," TENCON 2018 - 2018 IEEE Region 10 Conference, Jeju, Korea (South), 2018, pp. 0383-0388, doi: 10.1109/TENCON.2018.8650255.

[97] Suroso and T. Noguchi, "Multilevel Current Waveform Generation Using Inductor Cells and H-Bridge Current-Source Inverter," in *IEEE Transactions on Power Electronics*, vol. 27, no. 3, pp. 1090-1098, March 2012, doi: 10.1109/TPEL.2010.2056933.

[98] P. G. Barbosa, H. A. Carvalho Braga, M. D. Carmo Barbosa Rodrigues and E. C. Teixeira, "Boost current multilevel inverter and its application on single-phase grid-connected photovoltaic systems," in *IEEE Transactions on Power Electronics*, vol. 21, no. 4, pp. 1116-1124, July 2006, doi: 10.1109/TPEL.2006.876784.

[99] F. Gao, P. C. Loh, F. Blaabjerg and D. M. Vilathgamuwa, "Five-Level Current-Source Inverters With Buck–Boost and Inductive-Current Balancing Capabilities," in *IEEE Transactions on Industrial Electronics*, vol. 57, no. 8, pp. 2613-2622, Aug. 2010, doi: 10.1109/TIE.2009.2030208.

[100] L. Ding, Z. Quan and Y. W. Li, "Common-Mode Voltage Reduction for Parallel CSC-Fed Motor Drives With Multilevel Modulation," in *IEEE Transactions on Power Electronics*, vol. 33, no. 8, pp. 6555-6566, Aug. 2018, doi: 10.1109/TPEL.2017.2754462.

[101] L. Ding and Y. W. Li, "Multilevel CSC System Based on Series–Parallel Connected Three-Phase Modules With Optimized Carrier-Shift SPWM," in *IEEE Transactions on Power Electronics*, vol. 36, no. 4, pp. 3957-3966, April 2021, doi: 10.1109/TPEL.2020.3021392.

[102] P. E. Melin *et al*., "Analysis and Design of a Multicell Topology Based on Three-Phase/Single-Phase Current-Source Cells," in *IEEE Transactions on Power Electronics*, vol. 31, no. 9, pp. 6122-6133, Sept. 2016, doi: 10.1109/TPEL.2015.2502185.

[103] Q. Wei, B. Wu, D. Xu and N. R. Zargari, "Power Balancing Investigation of Grid-Side Series-Connected Current Source Inverters in Wind Conversion Systems," in *IEEE Transactions on Industrial Electronics*, vol. 64, no. 12, pp. 9451-9460, Dec. 2017, doi: 10.1109/TIE.2017.2711566.

[104] L. Xing and Q. Wei, "Series-Connected Current-Source Inverters: f_{SW} = 60 Hz," in *IEEE Transactions on Power Electronics*, vol. 35, no. 9, pp. 8882-8885, Sept. 2020, doi: 10.1109/TPEL.2020.2974734.

[105] L. Xing and Q. Wei, "Series-Connected Current Source Inverters With Less Switches," in *IEEE Transactions on Power Electronics*, vol. 35, no. 6, pp. 5553-5556, June 2020, doi: 10.1109/TPEL.2019.2951794.

[106] Bin Wu, Yongqiang Lang, Navid Zargari, Samir Kouro, Power Conversion and Control of Wind Energy Systems, John Wiley & Sons, Inc., Hoboken, New Jersey, July 2011.

Appendix

Figure A.1 illustrates the lab-scale setup that is used for experimental verification of this thesis research. Modifications and rearrangements are made to accommodate the proposed different power converters in this research.

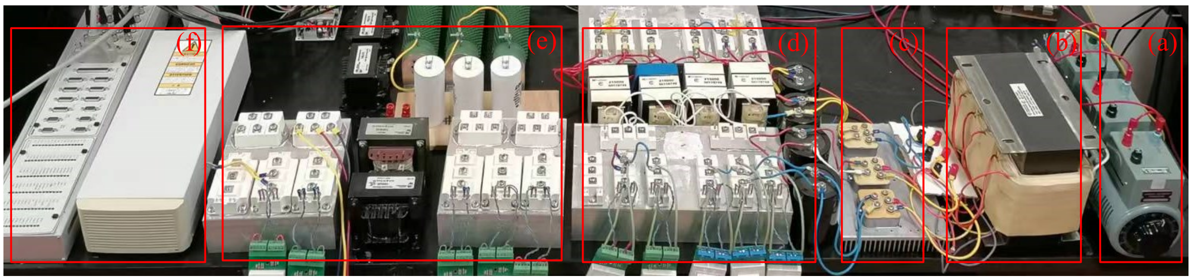

Figure A.1: Lab-scale setup for experimental verification: (a) Variac, (b) phase-shifting transformer, (c) multi-pulse rectifiers, (d) modular H-bridge converters, (e) CSC modules, and (f) dSPACE1103.